UNIVERSITY OF CALIFORNIA,

IRVINE

A TRUE MULTI-MODALITY SYSTEM FOR OPTICAL IMAGING WITH MR RESOLUTION: PHOTO-MAGNETIC IMAGING

DISSERTATION

For the degree of

DOCTOR OF PHILOSOPHY

In Electrical and Computer Engineering

By

Alex T Luk

Dissertation committee:
Associate Professor Gultekin Gulsen, Chair
Associate Professor Ozdal Boyraz
Professor Lydia Su

2016

Contents

List of Figures

List of Tables

ACKNOWLEDGMENTS

I am very thankful for all these years that I have worked in the Center for Functional Onco-Imaging. I would like to give my deepest appreciation to all that lab members that worked with me, helped me, taught me and guided me. I would not be able to go this far without the help from so many patient people.

My advisor, Professor Gultekin Gulsen, is an amazing mentor who is always kind, patient and helpful. I am very lucky to be his student. Every time I encountered problems during research, he was always optimistic and gave countless ideas. No matter how busy he was, he always found time to discuss potential solutions with me. He taught me how to approach the problems creatively and how to think. I am thankful for his great personality; he is always hopeful and persistent. He is not just a good teacher and a good advisor but also a good friend to us. He really cares about his students and gives insightful advice for our research, career and life.

My other advisor in the lab, Professor Lydia Su, who is also our center's director, also gave tremendous help to me during these years. She always worked diligently to help us, train us and give us her professional opinions from a clinical point of view. I would also want to thank Professor Ozdal Boyraz for serving as my committee member and for taking the time to come to my candidacy exam and my dissertation defense. I am grateful for his guidance me during my Master's degree when I first came to UC Irvine.

I would like to thank all my lab members. Yuting, who taught me every detail in the lab when I first came to the CFOI and helped me all the time if I had any problems in research and my career. Farouk is always inspiring, funny and supportive. I am grateful to him for teaching me the programming and mathematics of my project. Hakan was always patient with me and helped me tremendously in writing papers and presenting. I am thankful to Tiffany for being such a good friend and helping me with countless work. She was always helpful and brought so much fun to our group. Many thanks to Jessica, Jie and Jaedu for all the help they provided on the experiments.

I would also want to give special thanks to Dr. Mark Hamamura, Dr. Jeon-Hor Chen, Dr, Seunghoon Ha, Dr. Scott Li and Dr. Hon Yu for all the professional help they provided. It is my honor to work with and learn so much from them. It is a wonderful experience which I will never forget. I also want to thank Lena for animal preparation and for even coming in to perform animal studies with me during numerous weekends.

Also, I want to thank the NIH for providing F31 funding for my research. The work cannot progress without the generous support from NIH F31#1F31CA171745

Up to this point, I realize how lucky I am to come this far with so much support; there are so many people that helped me that I cannot list them all. Thank you all with all my heart.

Here, I also thank Institute of Physics and Engineering in Medicine, OSA and SPIE grant me the permission to use the papers I have published. Some of the text of this thesis is a reprint of the material as it appears in "An accelerated photo-magnetic imaging reconstruction algorithm based on an analytical forward solution and a fast Jacobian assembly method", "Comprehensive analytical model for CW laser induced heat in turbid media", and "Experimental validation of a high resolution diffuse optical imaging modality: photo magnetic imaging".

CURRICULUM VITAE

Alex T Luk

Education

2005 **B.S.** Electrical Engineering and Computer Science, National Tsing-Hua University, Taiwan
2007 **M.S** Electrical Engineering and Computer Science, University of California, Irvine
2016 **Ph.D** Electrical Engineering and Computer Science, University of California, Irvine

Award and Honors

- F31 National Research Service Award Individual Predoctoral Fellowship from the National Institute of Health

Field of Study

Multi-Modality Medical Imaging

Publications

- Luk, Alex; Nouizi, Farouk; Erkol, Hakan; Unlu, Mehmet B.;Gulsen, Gultekin, "*Ex vivo* Validation of Photo-Magnetic Imaging", Optics Express, 2016 submitted
- Luk, Alex; Lin Yuting; Unlu, B, et al. "Cross-validation of Dynamic Contrast Enhanced Diffuse Optical Tomography using a Multi-Modality Molecular Probe" JBO, 2016 submitted
- Nouizi, Farouk; Erkol, Hakan; Luk, Alex; Gulsen, Gultekin,"An accelerated photo-magnetic imaging reconstruction algorithm based on an analytical forward solution and a fast Jacobian assembly method", Phys Med Biol., 61(20):7448-7465, 2016
- Nouizi, Farouk; Hakan Erkol, Alex Luk, Unlu, Mehmet B. and Gulsen, Gultekin, "Real time Photo-Magnetic Imaging", Biomedical Optical Express, Vol. 7,Issue 10, pp.3899-3904, 2016
- Nouizi, Farouk; Luk, Alex; Thayer, David; Lin, Yuting; Gulsen, Gultekin, "Experimental validation of a high resolution diffuse optical imaging modality: photo magnetic imaging", Journal of Biomedical Optics, 21(1):016009, 2016
- Erkol, Hakan; Nouizi, Farouk; Luk, Alex; Gulsen, Gultekin, "Comprehensive analytical model for CW laser induced heat in turbid media", Optics Express Vol. 23, Issue 24, pp.31069-31084, 2015
- Lin, Yuting; Gao, Hao; Thayer, David; Luk, Alex; Gulsen, Gultekin, "Photo-Magnetic Imaging: resolving optical contrast at MRI resolution", Phys Med Biol, Vol. 58, Num 11., 2013

- Thayer, David; Lin, Yuting; Luk, Alex; et al. “Laser-induced photo-thermal magnetic imaging”, Applied Physics Letter, 101(8):83703., 2012

Conference

- Luk, A; Nouizi, Farouk; Marks, Michael; Kart, Turkay; Gulsen, Gultekin, “Monitoring gold nanoparticle distribution with high resolution using photo-magnetic imaging” SPIE Photonic West in San Francisco , 2016
- Erkol, Hakan; Nouizi, Farouk; Luk, Alex; Unlu, Mehment, B.; Gulsen, Gultekin, “A new analytical approach for heat generation in tissue due to laser excitation”, SPIE Photonic West in San Francisco, 2016
- Nouizi, Farouk; Erkol, Hakan; Luk, Alex; Lin, Yuting; Gulsen, Gultekin, “Analytical Photo Magnetic Imaging”, OSA Optical Tomography and Spectroscopy, 2016
- Erkol, Hakan; Nouizi, Farouk; Luk, Alex; Unlu, Mehment, B.; Gulsen, Gultekin, “An analytical Approach for temperature distribution in tissue”, OSA Biomedical Optics, 2016
- Luk, A; Yuting, Lin; Thayer, David; Ha, Seunghoon; Gulsen, Gultekin “Near Infrared Optical Tomography at MR resolution: Photo-magnetic Imaging” ISMRM in Toronto, 2015
- Nouizi, Farouk; Cho, Jaedu; Luk, Alex; Anashkin Edward; Stepanov, Pavel; Zavarzin, Val; Weinberg, Irvine N.; Su, Lydia; Gulsen, Gultekin; Nalcioglu, Orhan, “Hybrid PEM/MRI, a new approach for high resolution breast imaging”, ISMRM at Toronto, 2015
- Cho, Jaedu; Ha, Seunghoon; Luk, Alex; Nouizi, Farouk; Gulsen, Gultekin; Nalcioglu, Orhan; Su, Lydia, “A new unilateral breast specific coil design and dual-modality interface configuration for MR/scintimammography”, ISMRM at Toronto, 2015
- Luk, A; Ha, Seunghoon; Nouizi, Farouk; Thayer, David; Lin, Yuting; Gulsen, Gultekin , “A true multi-modality approach for high resolution optical imaging: photo-magnetic imaging”, SPIE Photonic West in San Francisco, 2014
- Luk, A; Yuting, Lin; Grimmond, Brian; Sood, Anup; Uziris, Egidijus E.; Nalcioglu, Orhan; Gulsen, Gultekin, ”Validation of diffuse optical tomography using a bi-funcitonal optical-MRI contrast agent and hybrid MRI-DOT system” , SPIE Photonic West in San Francisco, 2013
- Luk, A; Thayer, David; Lin, Yuting; Nouizi, Farouk; Gao, Hao; Gulsen, Gultekin, ”A novel high-resolution optical imaging modality: photo-magnetic imaging”, SPIE Photonic West in San Francisco, 2013
- Lin, Yuting; Thayer, David; Luk, Alex; Gulsen, Gultekin, "Photo-Magnetic Imaging: Optical Imaging at MRI resolution", OSA BIOMED, 2012
- Luk, Alex; Lin, Yuting; Grimmond, Brian; Sood, Anup; Uziris, Egidijus E.; Nalcioglu, Orhan; Gulsen, Gultekin , “Simultaneous monitoring of a bi-functional optical-MRI contrast agent using a hybrid DOT-MRI system”, Bio-Optics: Design and Application (BODA) OSA Conference, 4-6 April, Monterey, 2011

ABSTRACT OF THE DISSERTATION

A TRUE MULTI-MODALITY IMAGING SYSTEM FOR OPTICAL IMAGING WITH MR RESOLUTION: PHOTO-MAGNETIC IMAGING

By

Alex T Luk

Doctor of Philosophy in Electrical and Computer Engineering

University of California, Irvine, 2016

Associate Professor Gultekin Gulsen, Chair

A major goal of *in vivo* imaging is to obtain individualized structural, functional, and molecular information to provide personalized medicine. In particular, optical imaging uses non-ionizing radiation to provide functional information such as hemoglobin concentration and also visualize exogenous contrast agents as well as molecular and functional markers. Indeed, *in vivo* optical imaging extends across a wide range of applications, from cellular to organ levels. At high end of the spectrum, diffuse optical tomography (DOT) can penetrate up to 10 centimeters but only offer low-resolution images (> 5mm) due to highly scattering nature of the tissue.

Significant effort has been spent on multi-modality imaging techniques to improve the resolution of DOT. While combining DOT with spatial information defined by a separate anatomical imaging modality is promising, there are many challenges and inaccuracies that arise with co-registration. However this can be overcome with a novel multi-modality imaging technique, Photo-Magnetic Imaging (PMI) which uses MRI as a detector to provide both high resolution anatomical and optical information. PMI takes advantage of the 3D measurement capabilities of MR thermometry (MRT) to non-invasively measure the temperature increase of

the medium induced by a laser to acquire a temperature map of the entire volume. As DOT measures the photon flux only from the boundary, the major advantage of PMI is that high absorbing regions can be resolved directly from the high spatial resolution temperature map. These measurements can then be converted to obtain the optical absorption properties of the tissue using a reconstruction algorithm to model the light propagation and heat transfer in tissue.

This thesis will present the development of the first preclinical *in vivo* small animal PMI system prototype using the safety standards set by the American National Standard Institution. To optimize the system for *in vivo* studies, a fast PMI reconstruction method was also developed to accelerate the original PMI reconstruction method ~1000 times faster. These promising results validated the practicality of PMI for preclinical studies and showed the potential of PMI for clinical studies. This led to the development of the first human PMI prototype for clinical breast studies.

Chapter One: Introduction

1.1 Introduction and motivation

Medical imaging is a developing field of scientific research and technological development. It provides information inside tissue with the help of interior images of tissue. In recent years, medical imaging has evolved parallel to the drastic advances in imaging modalities such as X-ray Computed Tomography (CT), Magnetic Resonance Imaging (MRI) and Ultrasound Imaging providing anatomical information non-invasively [1]. These techniques have led to diagnosis and hence treatment of various illnesses. X-ray techniques are useful to obtain images of bones since other tissues absorb the X-ray less than bones in the body. MRI images yields anatomical and physiological information of the body. It uses the fact that nuclei or molecules absorb and release photon when an external magnetic field is applied invasively [1].

Diffuse Optical Imaging (DOI) has also become popular due to its low cost and non-invasive application. DOI is an optical imaging method for imaging of thick tissue [2-5]. It uses near-infrared (NIR) light to quantitatively characterize the optical properties of tissue, namely, absorption and scattering coefficients since absorption in tissue is very high at these NIR wavelength spectrum. Recent advances in DOI have made it possible to apply the modality for broad variety of diagnostic applications, especially for imaging of the female breast, the adult and infant brain. DOI involves obtaining 3D volumetric images of area of interest based on NIR spectroscopy. Diffuse optical tomography (DOT) is also one of DOI techniques providing two

2D images from boundary measurements of NIR light of tissue [2]. It provides functional information such as hemoglobin concentration and oxygen saturation in blood since their absorptions are high at NIR spectrum. In DOT, sources and detectors are located on the surface of the tissue. Combinations of source-detector pairs are recorded in reflection or transmission mode. While NIR light is traveling through tissue, it interacts with tissue mainly by absorption and elastic scattering. Therefore, reconstruction of absorption and scattering images are obtained due to the recorded measurements by using numerical iterative methods for the diffusion equation. In tissue, hemoglobin in red blood cell is the main absorber of NIR light [1]. Horecker first presented the diagnostic application of NIR light due to by making use of the differences in absorption coefficients of oxygenated and deoxygenated blood cells at this wavelength [6]. Although DOT provides functional information about tissue, measurements are acquired over distances of a few millimeters since scattering in tissue is substantially larger so that it suffers from its low resolution and accuracy. In other words, highly scattering leads photons to propagate longer and deeper in the bio subject, which makes it very difficult to collect photons and hence information to reconstruct. This is the main limitation of DOT. Optical coherence tomography (OCT) is also another technique which utilizes NIR and provides superior resolution for the bio tissue but is highly limited by the depth (less than 1 mm).

A lot of efforts have been made for the development of tomographic systems. On the other hand, difficulties in solving inverse source problem have brought attention for multi-modality systems. The inverse problem for DOT is ill-posed which means that the solution is non-unique. At the same time, it is mainly dependent on noise because of the measurement. The challenges which the inverse source problem leads to can be overcome by utilizing multi-modality systems since they provide a *priori* (complementary) information providing anatomical information for the

inverse problem of DOT keeping the functional information DOT yields. Although conventional medical imaging modalities such as X-ray computed tomography and MRI are providing high resolution anatomic image, their signal contrast is not directly related to the tissue metabolism so that it is hard to provide functional information of the tissue. PAT combines the advantage of optical and ultrasound imaging modalities, high optical contrast as well as scalable ultrasound resolution and imaging depth. Still, it has some limitations. Limited quantitative accuracy in inhomogeneous scattering tissue for optical or ultrasound waves is one of the challenges. Another limitation is the effect of acoustic impedance mismatch between different tissue types such as the bones or skull and surrounding soft tissues. Especially, the requirement of conducting medium between ultrasound transducers and the tissue under examination is one of the main disadvantages of PAT. Based on the similar concept, the high-resolution MRI has been tried to combine with DOT. A simultaneous MRI-DOT image uses anatomical structure information provided by MRI as an a priori data for DOT reconstruction for higher accuracy optical imaging. However, it is not a suitable multi-modality imaging and does not overcome the ill-posed problem of DOT reconstruction, which is the number of unknowns are greater than the number of measurements.

Unlike the aforementioned multimodality techniques (which takes just images from one technique and uses in the other), we propose a true imaging modality, which is called Photo-Magnetic Imaging (PMI) to overcome the challenges mentioned above. Our aim is to develop high resolution, non-invasive and non-contact optical tomography. PMI utilizes laser and MRI to illuminate tissue and to measure changes in temperature, respectively. So it deals with the limitations resulted from optical imaging.

1.1.1 Optical characteristics of tissue

In this section, the basic of interaction of light with tissue is provided. Main optical characteristics of tissue are expressed in terms of absorption, scattering, anisotropy, and refractive index.

1.1.1.1 Absorption coefficient

When a collimated beams of light travels through a non-scattering medium by a distance x, its intensity decreases exponentially with a product of absorption coefficient and x (Figure 1.1) [1]:

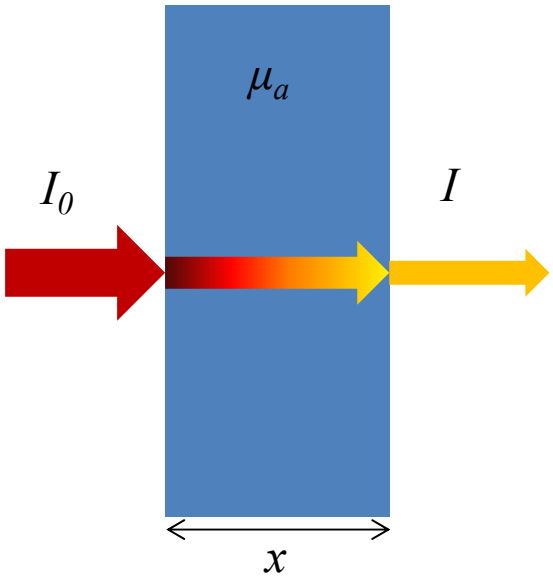

Figure 1.1 Attenuation of light for a non-scattering medium.

$$I = I_0 e^{-\mu_a(\lambda)x}$$

Here, the absorption coefficient, μ_a, is defined as the probability of a photon to be absorbed per unit length [1], I and I_0 are the final and initial light intensity. Actually, absorption is resulted from the transition of two energy levels of a molecule at a specific wavelength. When tissue (or

medium) is illuminated by light, physical effects are generated due to the absorption. Absorption occurs when the energy of the photon energy meets the energy difference between a molecule's two energy levels. Absorption coefficient is dependent on wavelength. For example, at the therapeutic window (650 nm -1350 nm), water has negligible optical absorption. Therefore, it does not prevent the near infrared light so that the light can penetrate deeper into the tissue at these wavelength spectra. Also, imaging system can separate different chromophores by its own specific spectrum as shown in Figure 1.2.

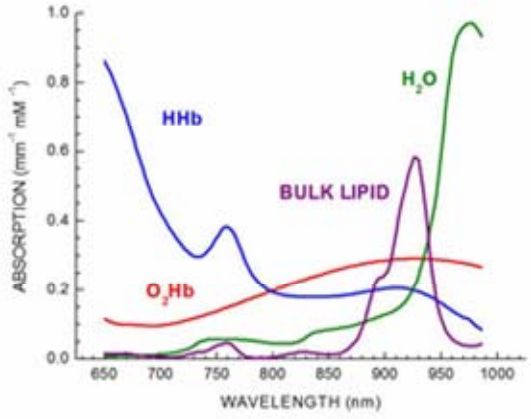

Figure 1.2 Spectrum of different major chromophores in human body. [7]

1.1.1.2 Scattering coefficient

Optical scattering is resulted either from particles or from the surrounding medium having a different refractive index (or varying refractive index in tissue). Mie theory assumes that photons are scattered from ideal spheres through a medium (Cells or water droplets can lead to Mie scattering) [6]. Rayleigh scattering is also used to describe elastic scattering of photons in which the wavelength of light is much greater than spheres' radius.

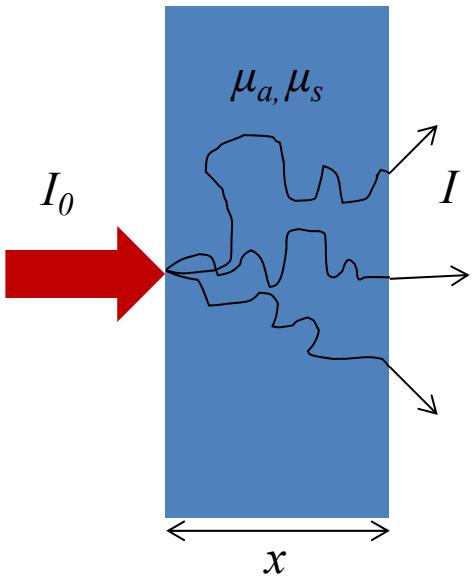

Figure 1.3 Attenuation of light through a scattering medium.

The scattering coefficient is defined as the probability of a photon to be scattered per unit length. Photons travel in very complicated, random paths when the medium is highly scattering. Thus, it is impossible to detect all the photons traveling through the medium since the detector cannot record at all the boundary points [1]. The attenuation of light can be approximated by the Beer-Lambert law, which is the number of transmitted photons is an exponentially decreasing function of the product of distance travelled by photons and differential path length factor. On the other hand, if the medium is non-scattering and the collimated light is used, the intensity of the transmitted (emerging) photons is exponentially decaying function of the width of the medium. Attenuation through scattered medium can be expressed by the modified Beer-Lambert law:

$$I = I_0 e^{-\mu_a DPFx+G}$$

Here, *DPF* is defined the differential path-length factor, which is dependent on the scattering and absorption coefficients, the isotropy, and the geometry of the medium. *G* accounts for loss of photons because of the geometry of the medium [1].

1.1.1.3 Anisotropy

The anisotropy of a medium is defined by the mean value of cosine function of the scattered light to simplify directional effects, which is also called Landé g-factor. The scatter is isotropic if the factor g is zero.

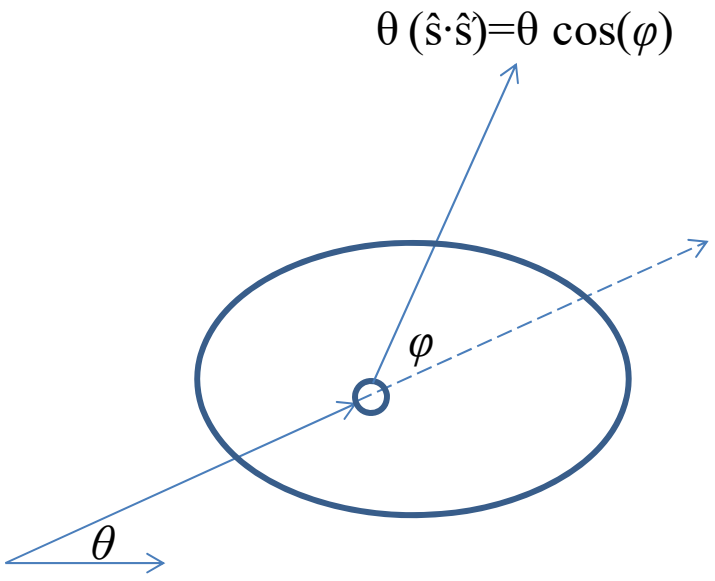

Figure 1.4 The phase function θ is usually anisotropic.

The phase function θ(ŝ·ŝ′) holds for

$$\iint_{4\pi} \theta(\hat{s}\cdot\hat{s}')d\Omega$$

The phase function is dependent on the scalar product of ŝ·ŝ', the angle between the incident and scattered light. The reduced scattering coefficient μ_s' is defined as $\mu_s'=(1-g)\mu_s$ for tissue. Here, the anisotropy factor g can be used to describe the degree of anisotropy of the phase function (typically 0.9 for biological tissue) [8-9].

1.1.1.4 Refractive index

When light travels through a medium to another one whose refractive index is different, its velocity changes. In other words, refractive index characterizes the effect of a medium on the speed of light. The speed of light c, is given by

$$c = \frac{c_0}{n}$$

Here, c_0 is the speed of light in vacuum and n is the refractive index (typical value for tissue is 1.4 c_0) [1,10]. The refractive index can be imaginary. While its real part represents the stored energy affecting the speed of light in media, the imaginary part stands for energy dissipation and indicates the absorption coefficient [11].

1.2 Diffuse Optical Imaging (DOI)

The radiative transfer equation is very successful to describe photon transport in turbid media [12,13]. However, the diffusion equation is usually preferred since it is very hard to solve RTE. In tissue, the diffusion approach also yields results which match with the experimental ones very well since the scattering is considerably larger than absorption [14]. The scattering and absorption properties are characterized by the scattering and absorption coefficients, μ_s and μ_a respectively.

Diffuse Optical Imaging also uses diffusion approximation to model light transport in tissue [3,15-19]. It is useful for imaging of thick tissue. This technique deals with the determination of the absorption and scattering of the tissue. It has a wide range of applications from breast imaging to brain imaging [18]. Light sources and the detectors are placed on boundary of the region of interest and recordings are acquired. Reconstructions of absorption and scattering images are obtained based on numerical iterative methods for the diffusion equation.

DOT systems can provide real and imaginary parts of photon waves as well as phase and amplitude of the waves. For example, a frequency domain system provides amplitude and phase of the diffusion waves (experimental counterpart of solutions of the diffusion equation). In DOT, source and detectors are usually positioned uniformly on the boundary of region of interest. The light source is approximated by a collimated source leading to a point source approximation. In this approach, the light is described by a Dirac delta function. Another DOT approach is trans-illumination method. In this technique, source and detectors are located on the opposite sides of the boundary.

The spatial distribution of some of physiologically significant chromophores, mostly water, fat, oxy- and deoxy-hemoglobin can be determined using DOT [20] by using multi-wavelength measurements. Hence, DOT can yield functional information such as total hemoglobin and oxygen saturation maps with high sensitivity, which leads to a variety of applications from brain imaging to molecular imaging [20].

Although DOI has high sensitivity in yielding valuable functional information, its spatial resolution is low. The solution of the inverse problem of DOT is non-unique and measurement sensitive because of the ill-posed property [3]. In other words, the number of unknowns is

greater than the number of measurements, which makes the problem very difficult to solve. Obtaining the measurements only from the boundary makes the inverse problem of DOT ill-posed property. On the other hand, acquiring internal measurements would improve the reconstruction process. It has been shown that these measurements considerably ameliorate the reconstruction performance of magnetic resonance imaging (MRI)-electrical Impedance Tomography (MREIT) [21]. Hence, combining DOT with MRI (which is a true multimodality), can overcome ill-posed property of the inverse problem of DOT.

1.3 Photo-Magnetic Imaging

Photo-Magnetic Imaging (PMI) is a novel MRI-DOT multi-modality imaging, which is presented by our team headed by Dr. Gulsen. It utilizes laser light to heat tissue. The induced temperature changes are measured using Magnetic Resonance Imaging (MRI). The theoretical basis of the PMI can be explained in two steps; light transport is modeled by the diffusion equation while the heat distribution is modeled by the Bio-Heat equation. The solution to the diffusion equation (photon density) is used in the source term of the heat equation to obtain change in temperature. Actually, the source term of the heat equation is a product of the absorption coefficient and the photon density. Photon density can be found by either analytical or numerically depending on the geometry, regularity and homogeneity of the medium. The image reconstruction of PMI is obtained by utilizing the finite element method with an iterative method.

PMI involves temperature measurements acquired by MRI from the whole volume as opposite to DOT in which the measurements are obtained only from the boundary. For this reason, PMI has the advantage to solve the inverse of DOT. Also, PMI is a non-contact imaging modality

Another virtue of the PMI is its direct measurement of temperature map. Indeed, PMI signals are originated from the temperature increase as a result of the product of photon density and the absorption coefficient at any point ($T=\mu_a\Phi$). However, PMI measures T directly, the objects will be directly resolved in the MR temperature map and reconstruction process will only require to obtain their quantitative absorption coefficients. Hence, PMI will provide not only optical images with similar resolution but also potentially higher quantitative accuracy.

When the current PMI system can be combined with MR systems, it becomes a low-cost multimodality. It should be noted that although the MR scan would increase the cost, it would also bring unique structural and functional MR information along with optical images of PMI. PMI can speed up process of orthotropic tumor models and development of optical molecular probes by providing whole body imaging of spontaneous metastases and distribution of molecular probes *in vivo*. PMI can be an important next generation multi-modality medical imaging technique.

1.4 Innovation and contributions

The major innovation and contributions have been made during this thesis:

- This is the first photo-magnetic imaging fully working with laser power under American National Standard Institute (ANSI) safety limit. In this work, the MR thermometry

sequence has been optimized for Photo-Magnetic Imaging by using our finite element based PMI simulation model and quality results are obtained with the limited laser power which is under the skin maximum permissible exposure (MPE) instructed by American Nation Standard Institute.

- A fast reconstruction method has been developed to speed up Photo-Magnetic Imaging reconstruction program. Comparing to diffuse optical tomography reconstruction, the computation complexity of PMI is nearly 100~10000 times depending on the resolution of the PMI setting. The fast reconstruction method helps to reduce the computation time to the same order as DOT reconstruction and make the real-time PMI possible for clinical work.

- The limitation and resolution limit of PMI has been well characterized in this work. As a new imaging modality, it is important quantify the limit of the PMI. During this work, a series of the phantom tests has been made and processed through the PMI reconstruction program.

- The first *ex vivo* and *in vivo* PMI studies under ANSI limit have been shown in this work. Due to the low signal to noise ratio (SNR) in real biological tissue study, keeping the laser power under ANSI limit will become a more challenge task for photon based imaging system. A quality high SNR MRI animal coil has been built to work with Philips 3 Tesla Achieva system and cooperated with a large collimator lens laser focusing system. This prototype of PMI has high stability and supplies enough SNR for high quality PMI measurement for *ex vivo* and *in vivo* study.

- A breast PMI coil has also been set up and tested. By integrating fast reconstruction algorithm, optimized low laser power PMI sequence and high stability PMI system, most of the preclinical studies are finished which made PMI ready to use for a clinical trial. The breast PMI can be a very promising area of research to start with. A series of breast PMI simulation based on the FEM has been run and verified the feasibility of clinical use of PMI.

Chapter Two: Modeling and image reconstruction techniques

Imaging a turbid medium using diffused light implies establishing a relationship between the intensity of light I, measured at a given distance from a source of illumination I_0, considering the optical properties of this medium, namely its absorption, μ_a, and scattering, μ_s, coefficients. Considering the particle nature of light, this relationship can be modeled using the radiative transport theory. In fact, the radiative transport equation (RTE) is a strong mathematical tool used in various applications to describe the energy balance within a given medium [22]. However, the RTE is very complex and is usually simplified under certain assumptions. Its most used simplification is the diffusion approximation [15]. This approximation is valid in the therapeutic window, spectral window where the propagation of photons is mostly driven by the scattering which largely dominates the absorption [23].

2.1 Radiative Transport Equation:

The radiative transport equation or Boltzmann equation models the propagation of photons through a medium based on the evolution of the radiance $L(r,\hat{s},t)$ [W m^{-2} sr^{-1}]. The radiance of a source of light consists in the power emitted per a unit surface and a solid angle as follow:

$$\frac{1}{c_n}\frac{\partial L(r,\hat{s},t)}{\partial t}+\nabla L(r,\hat{s},t)\hat{s}+[\mu_a(r)+\mu_S(r)]L(r,\hat{s},t)=\mu_S\iint_{4\pi}L(r,\hat{s}',t)f(\hat{s}.\hat{s}')d\Omega'+S(r,\hat{s},t) \qquad (1)$$

Where, c_n is the speed of light in the medium having the refractive index n. $f(\hat{s}, \hat{s}')$ is the phase function describing the probability that a photon coming from $\hat{s}$ will be scattered towards $\hat{s}'$. The term $S(r,\hat{s},t)$ represents the energy emitted per unit of volume and unit of time in the direction $\hat{s}$.

2.2 Diffusion Equation:

The resolution of RTE is a very complex task. Therefore, it is usually approximated to the diffusion equation [24]. This approximation is made based on the assumption that light propagates in an isotropic fashion within a scattering dominant ($\mu_a << \mu_s'$) medium. Thus, the distance between the used source and detector has to be longer than the diffusion transport length ($1/\mu_s'$) in order to omit the directionality information.

Briefly, the diffusion approximation is made by first developing the terms of the RTE equation to spherical harmonics using the P_N approximation [3]. Considering only the P_N approximation terms of order 1, these terms can be separated into isotropic and anisotropic based on their components:

$$L(\vec{r},\vec{s}) = \frac{1}{4\pi}\left(\Phi(\vec{r}) + 3\vec{J}(\vec{r}).\vec{s}\right) \tag{2}$$

$$S(\vec{r},\vec{s}) = \frac{1}{4\pi}\left(S_0(\vec{r})\right) \tag{3}$$

Where Φ [W m^{-2}] and $\vec{J}$ [W] are the photon density and the photon current, respectively. S_0 is the isotropic source of light [W m^{-3}] situated $1/\mu_s'$ under the illuminated surface of the medium.

Afterwards, we integrate all the terms of the RTE with and without multiplying them by $\hat{s}$. Making the assumptions that the source term is isotropic and that the rate of change of photon current is negligible, the diffusion equation in the continuous wave (CW) form can be written as follow [3]:

$$\nabla \cdot [D(\vec{r})\nabla\Phi(\vec{r})] - \mu_a(\vec{r})\Phi(\vec{r}) = -S(\vec{r}) \tag{4}$$

where μ_a and μ_s' are the optical absorption and reduced scattering coefficients, respectively. The parameter $D(\vec{r}) = 1/[3(\mu_a(\vec{r}) + \mu_s'(\vec{r}))]$ is the diffusion coefficient.

As can be seen, the diffusion equation disregarded the dependence on the orientation vector $\hat{s}$. Here, the propagation is solved in term of intensity or density of photons and not in term of radiance anymore. Also, one can observe that the diffusion approximation is not dependent on both the scattering coefficient and the factor of anisotropy but on their combination μ_s'. In summary, three approximations have been made [3,25]:

1) We limited the P_N approximation to the terms of order 1.
2) The temporal variations of the photon current are negligible.
3) The source of light is isotropic.

The first two approximations can be reduced to $\mu_a << \mu_s'$, which states that photons have to undergo multiple scattering events before being absorbed. The values of absorption and reduced scattering of biological tissue have been presented in the first chapter. In the therapeutic window, the absorption coefficient value varies in the range [0.001 - 1] mm^{-1} while the reduced scattering coefficient is in the range [0.3 - 10] mm^{-1} [26]. Consequently, this late hypothesis is always verified for most of the biological tissues. Henceforth, all the assumptions will be considered satisfied in this study.

2.3 Boundary conditions:

The boundary conditions state that light is only injected at the position of the isotropic sources, which means that the radiance propagating towards the inside of the medium is null [27]. Not being able to manage the directionality information, the diffusion equation supposes that the photon current entering a given surface is equal to the fraction of the exiting current, reflected by the surface having the reflection index R [28]:

$$R = -1,44n^{-2} + 0,71n^{-1} + 0,668 + 0,0636n \quad (5)$$

Where n is the refractive index of the medium. Using the Fick's law, we can obtain the modified Robin boundary conditions given by [29-31]:

$$\Phi(\vec{r}) + 2\zeta D(\vec{r})\nabla\Phi(\vec{r})\cdot\vec{n} = 0 \quad (6)$$

Where $\vec{n}$ is the normal vector to the surface. ζ=(1+R)/(1-R) is the reflection index characterizing the surface. In DOT, the measured signals at the surface are given by [3]:

$$M(\vec{r}) = \frac{\Phi(\vec{r})}{2\zeta} \quad (7)$$

2.4 Diffused light image reconstruction techniques:

Image reconstruction can be considered as an optimization problem which consists in estimating the internal optical properties of an object after performing light fluence measurements on its surface in the case of DOT or internal temperatures variations in the case of PMI. In other words, a set of μ_a and μ_s' correspond to those of the object, if the modeled predictions match the measurements. Therefore, the performance of this method will depend on:

a. accuracy of the model representing the object,
b. quality of the experimental measured data,

Also, the type of measurements will define the number of parameters that the image reconstruction algorithm will be able to reconstruct. Unlike μ_a which only requires information about the intensity of measured light, μ_s' requires additional information about the propagation of photons within the object. This information can be obtained either using time-resolved [25,30-37] or frequency-domain [3,24,38-47] detection techniques. As aforementioned, our PMI system

utilizes a continuous-wave (CW) laser to warm-up the medium. The only measure of (CW) intensity variation can in no case be used to separate absorption and scattering in a heterogeneous object. Therefore, our studies will focus on the recovery of absorption maps (μ_a) which are directly related to the concentration of the chromophores present in the biological tissue.

The main step in the image reconstruction process is the creation of the matrix which relates the variations of the internal absorption coefficient at any position within the medium to their induced perturbations in measurements. This matrix is commonly called the *sensitivity matrix* or *the Jacobian matrix*. This step is based on the so called, *perturbation theory* [3]. This theory is based on the approximation stating that variations of μ_a will induce changes in measurements $Y_{s,d}(\mu_a)$ which can be expressed by a series of Taylor. A measure $Y_{s,d}(\mu_a)$ obtained considering the source s and the detector d on a medium having the absorption coefficient μ_a can be expressed as:

$$Y_{s,d}\left(\mu_{a1}\right) = Y_{s,d}\left(\mu_{a0}\right) + \frac{\partial Y_{s,d}\left(\mu_{a0}\right)}{\partial \mu_a}\left[\mu_{a1} - \mu_{a0}\right] + \frac{1}{2!}\frac{\partial^2 Y_{s,d}\left(\mu_{a0}\right)}{\partial {\mu_a}^2}\left[\mu_{a1} - \mu_{a0}\right]^2 + \ldots \tag{8}$$

The coefficients μ_{a0} and μ_{a1} respectively represent the initial and the perturbed state of μ_a.

Considering only the terms of order 1 in equation (8), we obtain the following definition:

$$J_{s,d}\left(\mu_{a0}\right) = \frac{\partial Y_{s,d}\left(\mu_{a0}\right)}{\partial \mu_a} = \frac{Y_{s,d}\left(\mu_{a1}\right) - Y_{s,d}\left(\mu_{a0}\right)}{\mu_{a1} - \mu_{a0}} \tag{9}$$

This matrix contains the amplitudes of variations in the measurements $Y_{s,d}(\mu_a)$ caused by a variation in the internal absorption μ_a when source s and detector d are used. The full Jacobian describing all the variations for the whole set of source-detector pairs can be obtained by assembling all the individual Jacobians $J_{s,d}(\mu_a)$.

From equation (9) we can write:

$$M_{s,d}(\mu_{a1}) - M_{s,d}(\mu_{a0}) = J^{M}_{s,d}(\mu_{a0})\left[\mu_{a1} - \mu_{a0}\right] \tag{10}$$

This problem is undetermined and strongly ill-posed. Therefore, it is not possible to directly invert the Jacobian matrix which is singular and not square. Hence, the pseudo inversion iterative algorithm of Levenberg-Marquardt is used to solve this problem [48,49]:

$$\Delta\mu_a = \left[J^T J + \tilde{\lambda} I\right]^{-1} J^T \Delta M \tag{11}$$

The vector $\Delta\mu_a$ [Nx1] contains the updates to the absorption coefficient at any node of the FEM node. ΔM [Mx1] is the vector containing the measurement variations. M is the number of measurements or source-detector pairs. I is defined as the identity matrix. The Hessian matrix, $J^T J$ [NxN] is known to be ill-conditioned [50]. Several techniques exist to reverse this type of matrix [50]. The common one consists in adding a term to its diagonal for stabilization. $\tilde{\lambda} = \lambda \max(diag(J^T J))$ is the regularization factor used to improve the stability of the inversion of the Hessian matrix [$J^T J$] by making it diagonally dominant [51-56].

Using non linear image reconstruction algorithms, equation (11) necessitates to be solved iteratively. At the first iteration, the values of $M_{s,d}$ are calculated using the initial distribution of $\mu_{a(init)}$. The difference between the measured $M^{(1)}_{s,d}$ and simulated data $M^{init}_{s,d}$ is used to estimate the update at the following iteration $\mu_{a(init+1)}$:

$$\begin{aligned} M^{(1)}_{s,d} - M^{(init)}_{s,d} &= J^{M}_{s,d}(\mu_{init})\left[\mu_{init+1} - \mu_{init}\right] \\ M^{(1)}_{s,d} - M^{(init+1)}_{s,d} &= J^{M}_{s,d}(\mu_{init+1})\left[\mu_{init+2} - \mu_{init+1}\right] \\ &\ldots \end{aligned} \tag{12}$$

The process is iterated in order to minimize the objective function given by:

$$\Omega = \sum_{s,d}\left(M^{(1)}_{s,d} - M^{(init+N)}_{s,d}\right)^2 \tag{13}$$

2.5 Mathematical framework of PMI

Figure 2.1 shows the diagram describing the image reconstruction algorithm. Unlike DOT where the data are the light fluence at the surface of the medium, the measurements consist in the internal temperature in PMI [57-59]. This image reconstruction algorithm is composed of two main steps: the forward and the inverse problem.

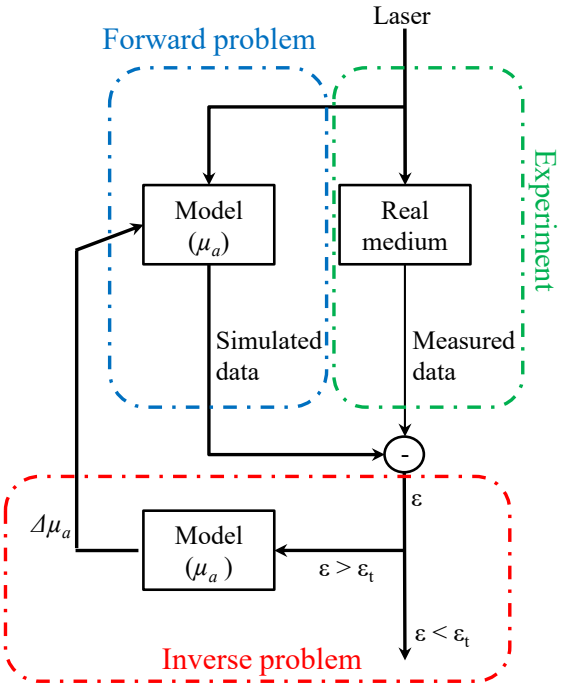

Figure 2.1 Diagram of the image reconstruction algorithm.

2.5.1 PMI forward problem

The used model is a numerical geometry having the same shape as the real object to be imaged. The PMI forward problem consists in the generation of temperature variations within a medium at any time after its heating using a NIR laser. This forward solver is defined by a system of two equations modeling each of light and temperature propagation and variation. The first equation is

the diffusion equation, which is used to model the transport of light in the medium [3, 15, 24, 31, 46, 47, 50, 60-63]. The second equation is the Pennes bio-heat thermal equation used to model the propagation and variations of the NIR laser induced temperature T [5, 20, 57, 59, 64-66]:

$$\begin{cases} -\nabla \cdot [D(r)\nabla\Phi(r)] + \mu_a(r)\Phi(r) = S(r) \\ \rho c \dfrac{\partial T(r,t)}{\partial t} - \nabla \cdot [k\nabla T(r,t)] = \Phi(r)\mu_a(r) \end{cases} \quad (14)$$

As a reminder, $\Phi(r)$ [W mm^{-2}] is the photon density at position r [mm], μ_a [mm^{-1}] is the absorption coefficient and D the diffusion coefficient, $D(r) = 1/3(\mu_a + \mu_s')$ with μ_s' [mm^{-1}] being the reduced scattering coefficient. *S(r)* is the isotropic source positioned under the illuminated surface of the imaged medium. The source is positioned inside the medium at a distance from the surface imposed by the approximation to diffusion equation and equal to $1/\mu_s'$. For the second equation terms, ρ is the density [g mm^{-3}], c, specific heat [J (g ˚C)$^{-1}$] and k the thermal conductivity [W (mm ˚C)$^{-1}$] of the medium. The source of thermal energy induced by the laser is expressed in the right hand side of the second equation. It is obtained by the product of the optical absorption and the photon density at any point within the medium [20, 66]. For phantom experiments presented in this paper, the metabolic heating and blood perfusion terms are neglected in the second equation but should be accounted for when performing *in vivo* experiments [57]. The Robin boundary conditions are used for the first equation as expressed by equation (6) [31]. For the second equation, the boundary conditions are defined considering the heat convection at the boundary only [20]:

$$-k\frac{\partial T(r)}{\partial n} = h\left[T_f - T(r)\right] \quad (15)$$

with T_f [˚C] being the ambient temperature and h being the heat transfer coefficient [W (mm^2 ˚C)$^{-1}$] at the surface of the medium.

The system of equations (14) can be solved either using numerical or FEM when the imaging complex irregular geometries or analytical methods when imaging media with regular geometries.

2.5.1.1 Numerical solutions: Finite element method

The diffusion equation is usually solved using numerical methods. One of the most powerful numerical methods is the Monte Carlo method which is a technique that transforms the deterministic problem of photon propagation into a probabilistic problem [67]. Prahl *et al*. introduced its use in modeling light propagation in biological tissue in the late 80's [68]. The other numerical method is the finite element method which is used to generate the results presented in this thesis [47].

Solving the diffusion equation using the finite element method (FEM) on a domain Ω, is to seek an approximate solution in the form of a piecewise field defined on subdomains of Ω. In other words, seeking a solution by FEM implies determining what local field is assigned to each subdomain such as the overall field obtained by juxtaposition of these local fields is close to the exact solution of the problem [47]. However, some constraints are imposed on the approximated solution, namely the fact that it has a simple continuity at the boundary between the sub domains. The accuracy of the solution depends on the division type of the main sub domain into smaller subdomains (number and size), choice of the local fields in each subdomain (test functions). This step is referred to as generation of the mesh [25]. In this thesis, all the results are generated using a mesh composed of N_T triangular elements connected at N vertices called nodes, Fig 2.2.

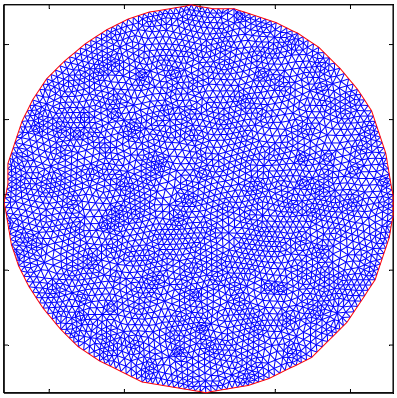

Figure 2.2 A typical mesh as used for FEM to solve the PMI forward problem through a circular domain. The mesh consists of 7200 triangular elements connected at 3705 nodes.

The estimation of the density of photons $\Phi(\vec{r})$ and the temperature $T(\vec{r})$ by FEM is obtained through their approximations $\Phi^h(\vec{r})$ and $T^h(\vec{r})$, which are polynomial functions defined over the basis function of FEM $u_i(\vec{r})$ with $u_i(\vec{r}_j) = \delta_{ij} \quad (i, j = 1,...,N)$, where $\vec{r}_j$ is the position of the node n_i.

$$\Phi^h(\vec{r}) = \sum_{i=0}^{N} \Phi_i(\vec{r}) u_i(\vec{r}) \tag{16}$$

$$T^h(\vec{r}) = \sum_{i=0}^{N} T_i(\vec{r}) u_i(\vec{r}) \tag{17}$$

To solve the PMI forward problem by FEM, the system of equation (14) and the boundary conditions given by equation (6) and (15) are reduced to a matrix inversion problem as follow [24,47]:

$$
\begin{aligned}
&\left[A(D)+C(\mu_a)+\beta(\zeta)\right]\Phi = S,\\
&\left[K(\kappa)+\gamma(h)\right]T = C(\mu_a)\Phi,\\
&A_{ij} = \int_{\Omega} D_i \nabla u_i(\vec{r}).\nabla u_j(\vec{r})\, d\Omega,\\
&C_{ij} = \int_{\Omega} c\mu_a u_i(\vec{r}) u_j(\vec{r})\, d\Omega,\\
&\beta_{ij} = \frac{c}{2\zeta}\int_{\partial\Omega} u_i(\vec{r}) u_j(\vec{r})\, ds,\\
&S_j = \int_{\partial\Omega} S_0 u_j(\vec{r})\, ds,\\
&K_{ij} = \int_{\Omega} \kappa_i \nabla u_i(\vec{r}).\nabla u_j(\vec{r})\, d\Omega,\\
&\gamma_{ij} = h\int_{\partial\Omega} u_i(\vec{r}) u_j(\vec{r})\, ds, I'm\_not\_sure\_of\_this\_one\\
&\Phi = \left[\Phi_1 \quad \Phi_2 \quad \ldots \quad \Phi_N\right],\\
&T = \left[T_1 \quad T_2 \quad \ldots \quad T_N\right].
\end{aligned}
\tag{18}
$$

The matrices A_{ij}, C_{ij}, K_{ij}, γ_{ij}, and β_{ij} (i,j=1, 2, ...,N) are of size NxN (N is the number of mesh nodes). Also, they are sparse and non-null only if i and j belong to the same triangular element. ζ is the reflection index characterizing the surface of the imaged medium having the refractive index n. From equation (18) we can observe that solving the PMI forward problem by FEM can be obtained by inversion of this matrix system:

$$
\begin{aligned}
&\left[A(D)+C(\mu_a)+\beta(\zeta)\right]^{-1} S = \Phi,\\
&\left[K(\kappa)+\gamma(h)\right]^{-1} C(\mu_a)\Phi = T,
\end{aligned}
\tag{19}
$$

2.5.1.2 Analytical solutions:

Several analytical solutions to the diffusion equation have been proposed for media with some regular geometries such as cylindrical, spherical and infinite or semi-infinite slabs [15, 63, 69-77]. In addition to the geometry restrictions, these analytical solutions perform only on optically homogeneous media. These analytical methods are usually based on the Greens' function and series expansion methods [15, 78-80]. Similarly to the diffusion equation, the heat equation has been solved analytically [81, 82]. In these solutions a simple photon density expressions to

describe the source term of the bio-heat equation is used. Recently, we proposed a new approach that not only provides a very comprehensive photon density expression but presents a very detailed analytical temperature expression for laser induced temperature in a circular medium as well [5]. For the first part, a detailed analytical solution is obtained for the diffusion equation based on an integral approach using the Robin boundary condition, which is more adequate for tissue modeling [61]. For the second part, the heterogeneous heat equation is solved using the separation of variables technique considering that the temporal and spatial parts of the heat equation can be separable. Here, the heat convection boundary condition is used to derive the solution.

The final expression of temperature induced with a laser heating of circular medium of diameter R at any position (r,θ) and at any time t is given by [5]:

$$T(r,\theta,t) = T_s + \sum_{m=-\infty}^{\infty}\sum_{l=-\infty}^{\infty}\frac{\rho c}{\kappa\lambda_l^2}\omega_{m,l}J_m(\lambda_l r)\cos(m\theta)\left[1-\exp\left(\frac{-\kappa}{\rho c}\lambda_l^2 t\right)\right] \tag{20}$$

where T_s is the ambient temperature and J_m is the first kind Bessel function, not to be confused with J, the Jacobian matrix used in the inverse problem. The factors λ_l are obtained from the heat convection boundary condition. The factors $\omega_{m,l}$ are derived from the solution of the diffusion equation of the PMI forward problem:

$$\begin{aligned}
\omega_{m,l} = \frac{\mu_a}{\rho c}\{&-a_m(\beta)r_i[\beta J_{m-1}(\beta r_i)J_m(r_i\lambda_l)-\lambda_l J_m(\beta r_i)J_{m-1}(r_i\lambda_l)]\\
&+b_m(\beta)r_i[\beta J_{m-1}(\beta r_i)J_m(r_i\lambda_l)-\lambda_l J_m(\beta r_i)J_{m-1}(r_i\lambda_l)]\\
&-\beta R J_{m-1}(R\beta)J_m(R\lambda_l)+R\lambda_l J_m(R\beta)J_{m-1}(R\lambda_l)\\
&+c_m(\beta)r_i[\beta Y_{m-1}(\beta r_i)J_m(r_i\lambda_l)-\lambda_l Y_m(\beta r_i)J_{m-1}(r_i\lambda_l)]\\
&-\beta R Y_{m-1}(R\beta)J_m(R\lambda_l)+R\lambda_l Y_m(R\beta)J_{m-1}(R\lambda_l)\}\\
\times&\frac{1}{\frac{1}{2}R(\beta^2-\lambda_l^2)\{R[J_{m-1}(R\lambda_l)^2+J_m(R\lambda_l)^2]-\frac{2mJ_{m-1}(R\lambda_l)J_m(R\lambda_l)}{\lambda_l}\}}
\end{aligned} \tag{21}$$

where a_m, b_m and c_m are the differentiation constants given by:

$$
\begin{aligned}
a_m(\beta) &= \frac{\gamma \cos(m\theta_i)}{2D[2D\beta\xi R J_{m-1}(\beta R) + (R - 2Dm\xi) J_m(\beta R)]} \\
&\times \{ J_m(\beta r_i)[2D\beta\xi R Y_{m-1}(\beta R) + (R - 2Dm\xi) Y_m(\beta R)] \\
&+ Y_m(\beta r_i)[-2D\beta\xi R J_{m-1}(\beta R) - (R - 2Dm\xi) J_m(\beta R)] \} \\
b_m(\beta) &= \gamma R \frac{D\beta\xi[Y_{m-1}(\beta R) - Y_{m+1}(\beta R)] + Y_m(\beta R)}{2D[2D\beta\xi R J_{m-1}(\beta R) + (R - 2Dm\xi) J_m(\beta R)]} \\
&\times J_m(\beta r_i) \cos(m\theta_i) \\
c_m(\beta) &= -\frac{\gamma}{2D} J_m(\beta r_i) \cos(m\theta_i)
\end{aligned}
\tag{22}
$$

2.5.2 PMI inverse problem

The PMI high resolution absorption maps are obtained by solving the so called inverse problem. Technically, this inverse problem consists in minimizing the quadratic difference between the measured MRT temperature and the simulated temperature maps according to the following objective function:

$$
\Omega(\mu_a) = \sum_{d=1}^{N_D} \left\| T_d^m - T_d(\mu_a) \right\|^2 \tag{23}
$$

where N_D is the number of used detectors. T_d^m represent the measured temperatures at node d and $T_d(\mu_a)$ are the temperatures simulated using the FEM forward solver considering the absorption distribution μ_a.

Note that using MRT, measurements are performed within the medium at all the mesh nodes and thus N_D is equal to the number of the FEM mesh nodes N. Therefore, the size of the *Jacobian* which was initially MxN, with M being the number of measurements, becomes NxN. However, it is possible to discard some of the measurements where the MRT measurements are below an acceptable *SNR* [57], making M slightly smaller than N. Therefore, considering the nature of the

Jacobian matrix, the minimization of equation (23) is performed using the Levenberg-Marquardt algorithm, Eq. (11):

$$\Delta\mu_a = \left(J^T J + \lambda I\right)^{-1} J^T \left(T_{s,d}^M - F_{s,d}\left(\mu_{ainit}\right)\right)^2 \tag{24}$$

2.5.2.1 Standard PMI sensitivity matrix:

In DOT, implementing the Jacobian matrix defined in equation (9) requires the resolution of the forward problem $N(N_S+1)$ times, with N_S being the number of sources. The first N_S times are solved to obtain the measurements $Y_{s,d}(\mu_{a0})$ using the homogeneous set of absorption coefficient μ_{a0}. Afterwards, the forward problem is solved after the sequential perturbation of μ_a at every node of the mesh. Clearly, this method is very time consuming. Therefore, it is generally established that the sensitivity matrix is computed using the *adjoint-method*, as in the case of DOT reconstructions using FEM [3]. This method states that the influence of a source "s" on a detector "d" is the same as the influence of "d" on "s" when "d" is used as source and "s" as detector. Using this formulation the Jacobian is simply obtained by solving the forward problem N_S+N_D times, where N_D is the number of used detectors. This adjoint-method significantly reduces the Jacobian assembly time and the overall computation time [31].

Using MRT to measure the internal spatiotemporal temperature of the medium is equivalent to placing a detector at each node of the FEM mesh. This configuration makes the use of the adjoint-method inadequate for the computation of the PMI Jacobian, since it loses its advantage due to the high number of detectors [65]. Therefore, the Jacobian is computed using the standard approach by perturbing the absorption at each node individually then solving the forward problem to establish a relationship between the absorption change at this node and the induced temperature variation at any point [20]. Nevertheless, unlike DOT, the sources are illuminated

simultaneously which reduces the number of resolution of the forward problem to N+1 times. Evidently, this straightforward method is very time consuming and requires very heavy computational resources.

2.5.2.2 Fast implemented PMI sensitivity matrix:

In order to overcome the long computation time imposed by the FEM implementation of the Jacobian matrix, we introduced a new method to analytically assemble the Jacobian matrix [65, 83]. This new method is later implemented it into our new so called analytic-based PMI image reconstruction algorithm [65, 83].

Technically, obtaining the Jacobian analytically requires the implementation of a new solution which is able to perform considering a spatially point variant absorption within a homogeneously absorbing medium then deriving it. To our knowledge, such an analytical computation would be very complex and has not been done yet. Therefore, we first utilize the FEM based algorithm to understand the dependence of the shape and amplitude of the Jacobian at any point as a function of optical and thermal properties of the medium. Please note that medium properties are varied over a wide range during these calculations. This empirical approach allows us to understand the relationship between these parameters and the shape as well as the amplitude of the Jacobian [65].

During this empirical approach, first step is to compute the Jacobians for all the N FEM nodes (J_n, n=1,2,..N), using our FEM-based solver while varying the optical and thermal properties of a synthetic phantom. Although we repeat these calculations over a wide range of optical and thermal properties, here we will present an example case with a certain set of parameters to explain this step in detail. Figure 2.3 shows a 40 mm diameter circular synthetic phantom whose absorption and reduced scattering coefficients are set to 0.01 mm-

1 and 0.8 mm-1, respectively. Meanwhile, the density, specific heat and thermal conductivity of the phantom are set to 1000 kg.m-3, 4200 J.(kg.°C)-1, and 0.5.10-3 W(mm.°C)-1, respectively. The light is illuminated at the bottom of the phantom and the laser power is optimized in order to allow a maximum heating under 2 °C at the illumination site, Figure 2.3.a.

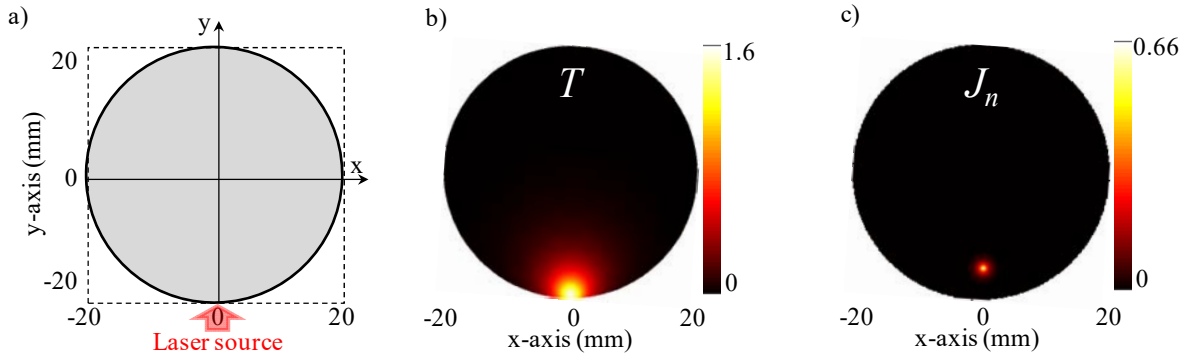

Figure 2.3 (a) Schematic showing the synthetic phantom and the position of the laser source. (b) The simulated temperature obtained by solving the PMI forward problem, 8 seconds after turning on the laser. (c) The computed Jacobian at a particular node *(x=0 mm, y=-15 mm)* [65].

Figure 2.3.b shows the temperature simulated after 8 seconds of heating with light using our FEM-based algorithm. This simulation uses a very fine mesh (*Mesh_1*) which consists of 65536 triangular elements connected at 33025 nodes. The Jacobian J_n at each node is computed using the standard method. After that each individual Jacobian is mapped into a 200 pixel x 200 pixel grid to obtain Jacobians in Cartesian coordinates. As an example, Figure 2.3.c shows the Jacobian J_n obtained at one of the nodes whose coordinates are x_0*=0 mm and* y_0*=-15 mm*. Unlike the banana shape sensitivity matrix observed in diffuse optical tomography[3], the obtained Jacobian J_n consists in a kernel centered at this point, Figure 2.3.c.

The Jacobian for each set of optical and thermal properties is first calculated for all nodes and then mapped into the Cartesian grid. Afterwards, an extensive series of fitting are performed to investigate all the aforementioned parameters. Based on these fittings, we established that the distribution of the Jacobian J_n at any node $n(x_0,y_0)$ can be expressed as:

$$J_n(x,y) = A_n\left(x_0,y_0\right)J_s(x-x_0,y-y_0) \tag{25}$$

where $A_n(x_0,y_0)$ is the amplitude of the kernel at the center and J_s is the shape of the kernel, which is obtained by normalizing the kernel fitted on the Jacobian computed on that node $n(x_0,y_0)$. This shows that the amplitude and the normalized shape of each Jacobian can be independently studied. Accordingly, we investigated them separately as a function of the parameters of the medium and the spatial position within the phantom.

2.5.2.2.1 Shape of the kernel (J_s)

To investigate the shape of the kernels, a series of fittings is performed on all the Jacobians J_n computed with FEM at each node $n(x_0,y_0)$. Figure 2.4.a shows an example of the fitted kernel on the Jacobian J_n obtained at a particular node (x=0 mm, y=-15 mm), Figure 2.3.c. After normalizing the fitted kernels, $\tilde{J}_n$, we observed that the shape of the kernel is found to be governed only by the optical and thermal properties of the phantom and is totally independent from the strength of the laser source and the spatial position within the medium. In other words, the normalized shape of the kernel, is found to be the same for a given set of optical and thermal properties. The normalized shape of the kernel, $J_s = \tilde{J}_n / max(\tilde{J}_n)$, is given by [65]:

$$J_s(x,y) = e^{\left(-3.12{\mu_a}^{0.58}-2.41\right)\left(\frac{\kappa}{\rho c}\right)^{0.27}\sqrt{(x-x_0)^2+(y-y_0)^2}} \tag{26}$$

The profiles performed on both Jacobians J_n and $\tilde{J}_n$ are in very good agreement, Figure 2.4.b. Please note that these fittings are verified not only for each node in a particular synthetic phantom but also for a large range of optical and thermal properties. Although the fitting is performed on Jacobians computed at the nodes, it is important to mention that Eq. (26) is valid for any point within the medium and allows us to calculate J_s at any point (x, y) in the Cartesian grid.

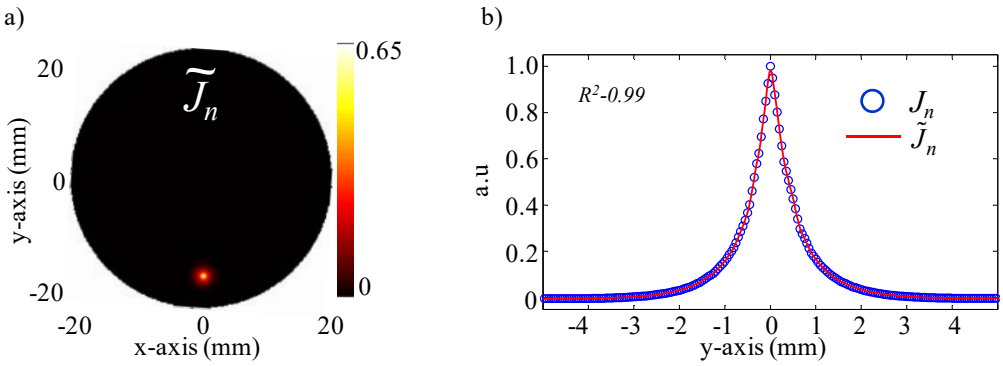

Figure 2.4 (a) The analytic Jacobian $\tilde{J}_n$ fitted on J_n obtained using our FEM-based solver at a particular node (x=0 mm, y=-15 mm). (b) The normalized profiles performed on $\tilde{J}_n$ and J_n [65].

2.5.2.2.2. Amplitude of the kernel (A_n)

Unlike the shape of the kernel, J_s, its amplitude, A_n, shows that in addition to the dependence on the optical and thermal properties, A_n exhibits a strong dependence on the spatial position within the medium. Implementing an analytical formula to obtain the amplitude of the kernel $A_n(x_0,y_0)$ with respect to its spatial position and background optical properties is complicated. In this paper, we propose an alternative method that allows us to obtain $A_n(x_0,y_0)$. This method is performed in two steps:

Since analytical solutions can be obtained only on homogeneous media, first the so called *Total Jacobian,* J_T, is computed using the standard method by varying the absorption coefficient

simultaneously at all the pixels instead of varying it locally at a given pixel. Since this step is performed using analytic methods, Cartesian coordinates are used and all the positions are defined as pixels that belongs to the 200 x 200 grid. Accordingly, the total Jacobian, J_T, corresponds to the sum of all the individual Jacobians J_n centered at each pixel $n(x_0,y_0)$ and can be written as [65]:

$$J_T(x,y) = \sum_{x=0}^{N_x} \sum_{y=0}^{N_y} J_n(x,y) \tag{27}$$

where N_x and N_y the size of the grid describing the domain, containing the phantom, in the x- and y- directions, respectively. By substituting equation (25) into (27), we obtain [65]:

$$J_T(x,y) = \sum_{x=0}^{N_x} \sum_{y=0}^{N_y} A_n(x_0,y_0) J_s(x-x_0, y-y_0) \tag{28}$$

Equation (28) shows that by definition, J_T at any pixel is then given by the convolution of the normalized kernel $J_s(x,y)$ and the amplitude of the kernel $A_n(x_0,y_0)$ at pixel $n(x_0,y_0)$ and we can write [65]:

$$J_T = A_n \otimes J_s \tag{29}$$

From equation (29), $A_n(x,y)$, the amplitude of the kernels at any position within the phantom is simply obtained by deconvolving the normalized kernel J_s from the Total Jacobian, J_T, Figure 2.5.a-c [65]:

$$A_n = J_T \otimes^{-1} J_s \tag{30}$$

Since both J_s and J_T are noise free, the deconvolution can be performed using any deconvolution method without any difficulty. Once the maximum amplitudes A_n are obtained analytically, the analytic Jacobians are assembled using equation (25).

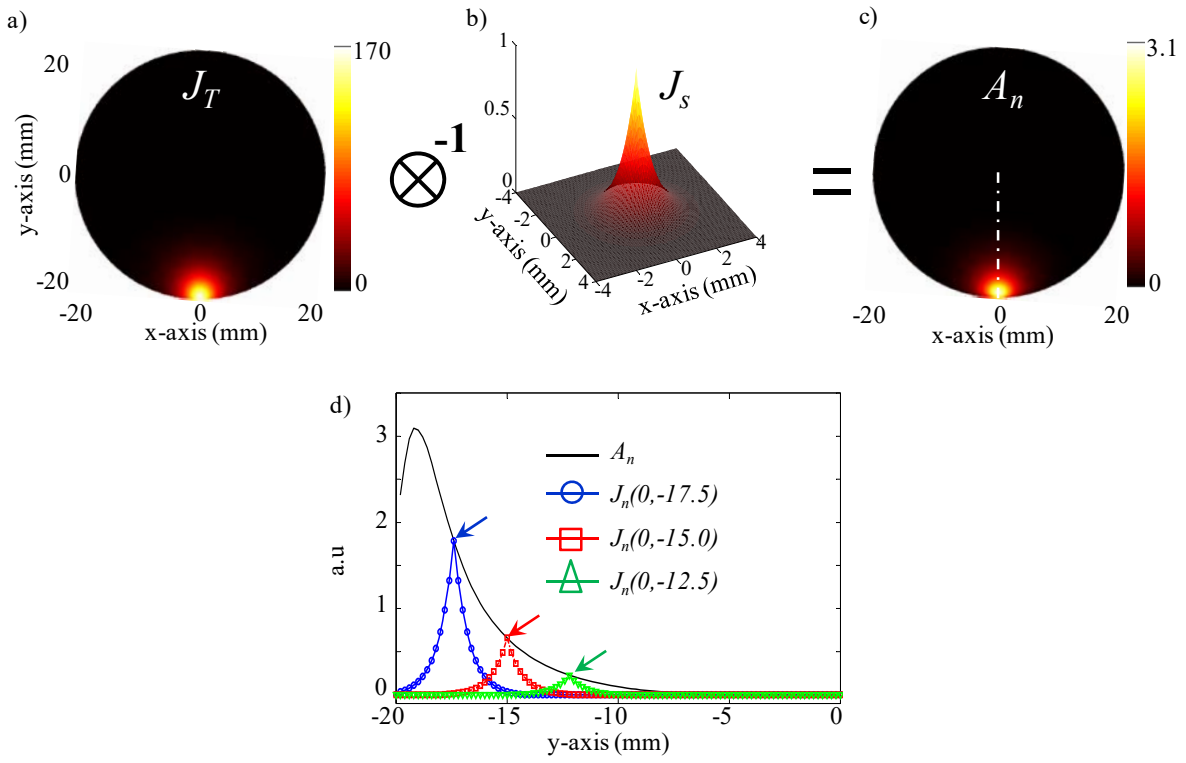

Figure 2.5 (a) The Total Jacobian J_T obtained by changing the absorption simultaneously at all nodes. The total Jacobian is also equal to the sum of the Jacobians computed individually at each node of the mesh. . (b) The normalized shape of the kernel obtained using equation (26). (c) A_n the maximum amplitude of the individual Jacobians. (d) The profile carried-out on A_n, along the white dashed-line, matches the maximum amplitude of the individual Jacobians computed using FEM at nodes (x=0 mm, y=-17.5, -15, -12.5 mm) [65].

To validate our approach, we compare the computed maximum amplitude using equation (30) with the amplitude of individual Jacobians chosen at random points. Figure 2.5.d shows that the profile of A_n, along the white dashed-line, matches perfectly the amplitudes obtained with the FEM-based algorithm at nodes (x=0 mm, y=-17.5, -15, -12.5 mm).

In summary, our new analytic Jacobian assembly method is performed following these steps. First, the distribution of the Jacobian J_s is obtained using equation (26). Secondly, the total Jacobian J_T is obtained using the standard method by varying the absorption coefficient of the

whole medium instead of a local variation at one given position. Afterwards, the amplitude of the Jacobian at each pixel A_n is obtained by simply deconvolving J_s from J_T. Following that, the Jacobian J at any point $n(x_0,y_0)$ is obtained using equation (25), multiplying the shape function by its corresponding amplitude at that particular point $n(x_0,y_0)$. Finally, the obtained Jacobian J is used in the PMI inverse problem as expressed by equation (24).

Chapter 3: Simulation studies

Simulations are preformed to optimize and verify our new PMI sequence and reconstruction. Heat diffusion simulation, multiple illuminations PMI, first and multiple iterations reconstruction, as well as adipose tissue excluded reconstruction simulation all proved valuable to this end. The following section details some of our techniques.

3.1 Heat diffusion simulation

Thermal diffusion could be a potential limiting factor of the PMI, however it has been included in the bio heat equation. A longer MRT acquisition time will result in a longer thermal diffusion distance. This phenomenon will make the PMI inverse problem both more complicated, and require more iterations to obtain accurate result. It will also demand higher signal noise ratio for the MRT. Acquiring data during heating phase can solve this issue. Heating phase refers to the period when the laser is on and the temperature change of the object is dominated by the laser photon absorption. The high absorption area will absorb more photons and heat up more than the background tissue. The temperature difference between them will drive thermal diffusion. However, during the heating phase period there is a continuous flow of photons into the sample. In the following simulation study, a 40mm cylindrical phantom is embedded with a 5mm, 8x absorption inclusion at the center. The sample is illuminated from top and bottom of the phantom as shown in Figure 3.1.

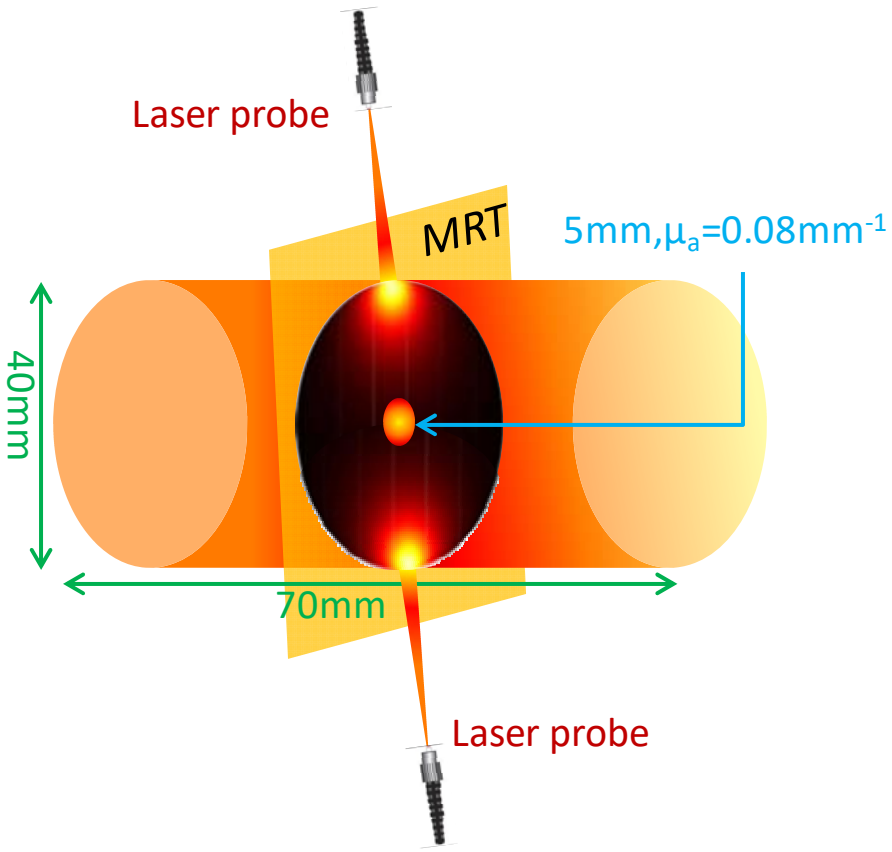

Figure 3.1 A 5mm diameter cylindrical inclusion is embedded at the center of a 40mm diameter phantom. The phantom background absorption coefficient for 808nm wavelength laser is 0.01mm^{-1}. Two laser source is illuminated the subject from top and bottom respectively.

The thermal diffusion length during the pulse period can be estimated as: $\delta_T = 2\sqrt{D_T.\tau_P}$. Using this equation, the calculated thermal diffusion length for 1, 6, 10 and 30 seconds are 0.75, 1.83, 2.37, 4.06 mm, respectively. One might think that resolution will degrade as imaging time increases. However, this is not true when the heat is continuously pumped into the tissue. As our simulation shows, during the heating process the FWHM of the profile measured around the object (dashed line) increases only up to 5.6 mm in 45 seconds, Figure 3.1 Diffusion shows its

blurring effect as soon as the laser is turned off, i.e. after 45 seconds of cooling off, FWHM increases to 9 mm.

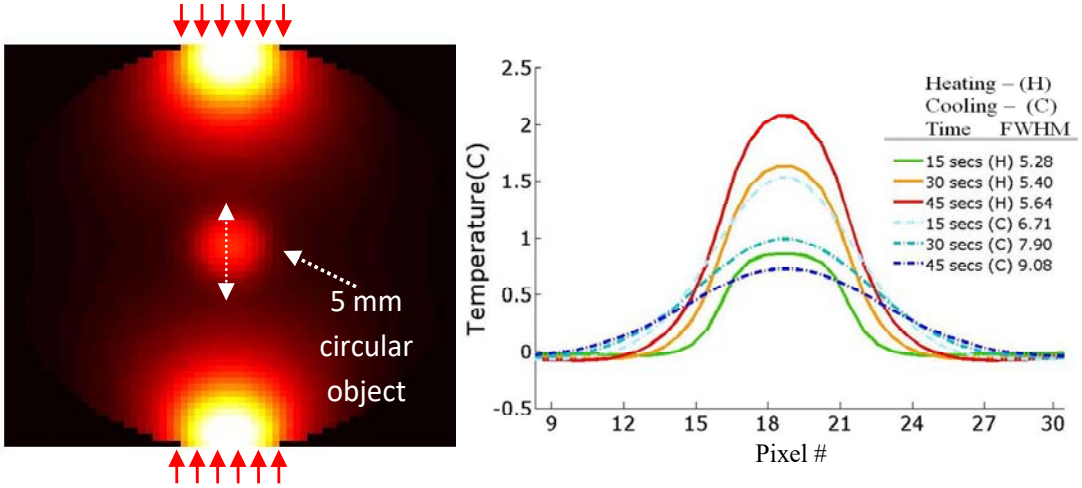

Figure 3.2 This simulation demonstrates that heat diffusion does not blur the object during the heating process (labeled with "H"). (a) The simulated temperature map at 30 seconds of heating. (b) FWHM changes from 5.28 mm to 5.64 mm in 45 seconds. However, after the laser is tuned off (labeled with "C"), FWHM increases from 5.64 mm to 9.08 mm in 45 seconds as expected.

3.2 PMI forward problem [57]

3.2.1 Single-port illumination

The first step in the experimental validation of our technique is the validation of the forward problem. For this purpose, a PMI temperature map is first acquired using a mice-sized 25 mm diameter cylindrical agarose homogeneous phantom with an optical absorption coefficient of 0.01 mm^{-1}, to mimic biological tissue. A 5 mm inclusion is embedded inside the phantom, 6 mm deep under the illumination site in order to mimic heterogeneous medium having a higher absorption area, Fig. 3.3.a. The inclusion is placed a bit off-center and its optical absorption is set to be 8 times higher than the background.

Meanwhile, using the forward solver, the temperature map is simulated on an identical synthetic phantom having the same size, optical and thermal properties. This simulated temperature map is then compared to the temperature map obtained by MRT.

Figure 3.3.b and 3.3.c show the measured and simulated temperature maps, respectively. Please note that, in order to compare the measured and the simulated data, a calibration step is needed. During this step, two parameters are defined from the experimental setup: the power of the laser and the shape of the illumination beam. Firstly, the laser power is measured at the output of each of the four collimation lenses using a power meter. Secondly, PMI measurements are performed on a homogeneous phantom with known optical and thermal properties. The PMI interface holds the phantom at the center and therefore, the position of the illumination beams on the sample are approximately known. Nevertheless, a minimization program calculates the exact position of the illumination beams on the sample by minimizing a quadratic difference between the measured and simulated temperature maps. Using these calculated parameters, a very good agreement is achieved between simulated and measured maps on this heterogeneous phantom as shown by the profiles presented in Fig. 3.3.d.

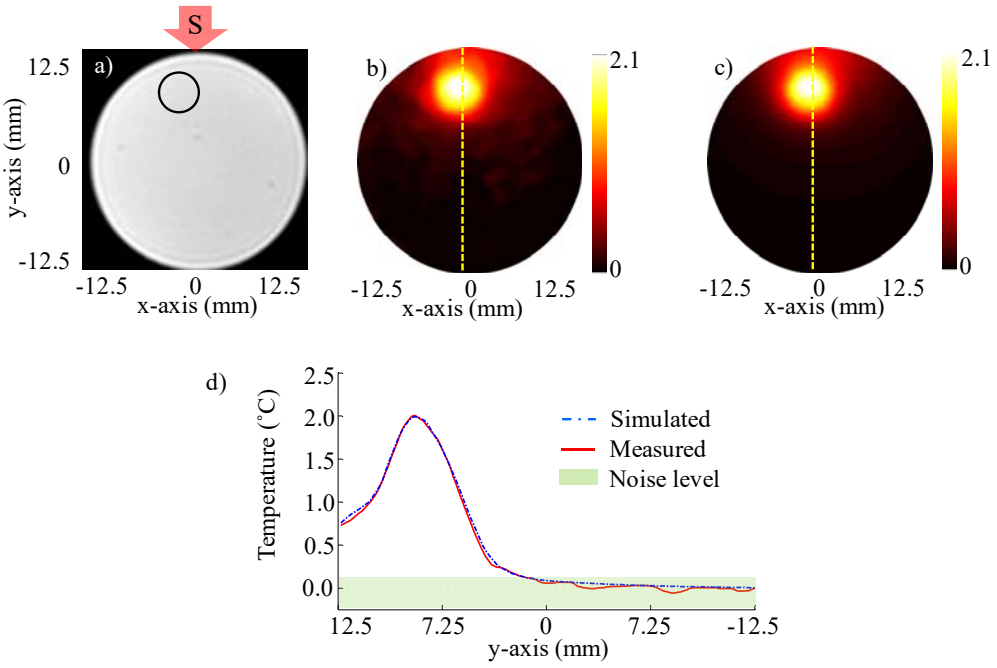

Figure 3.3 (a) The phantom cross-section showing the inclusion size and position. The laser used to heat the phantom from its top side, is represented by the red arrow *S*. The temperature maps (b) measured using MRT and (c) simulated using the forward solver. (d) The profiles taken along the y-axis, on the measured and simulated temperature maps. [57]

3.2.2 Multiple-port simulation

These first simulations show that the variation in the temperature decreases quickly with depth and goes below the sensitivity of our instrumentation. Additional simulations are performed to analyze the effect of simultaneous multiple point illumination on the depth penetration and stability of the inverse problem. As seen on Figure. 3.4, as the number of illumination beams increases, higher SNR is obtained at the center of the phantom. The temperature maps reveal that, 4-port illumination gives the highest overall temperature increase in the whole phantom. The profiles in both x- and y- directions clearly show that the temperature increase at the center of the phantom is above the noise level only when 4-port illumination is used Fig. 3.4.b. Based

on these results, we upgraded our PMI interface by adding 4-port illumination and performed all the experiments with this configuration.

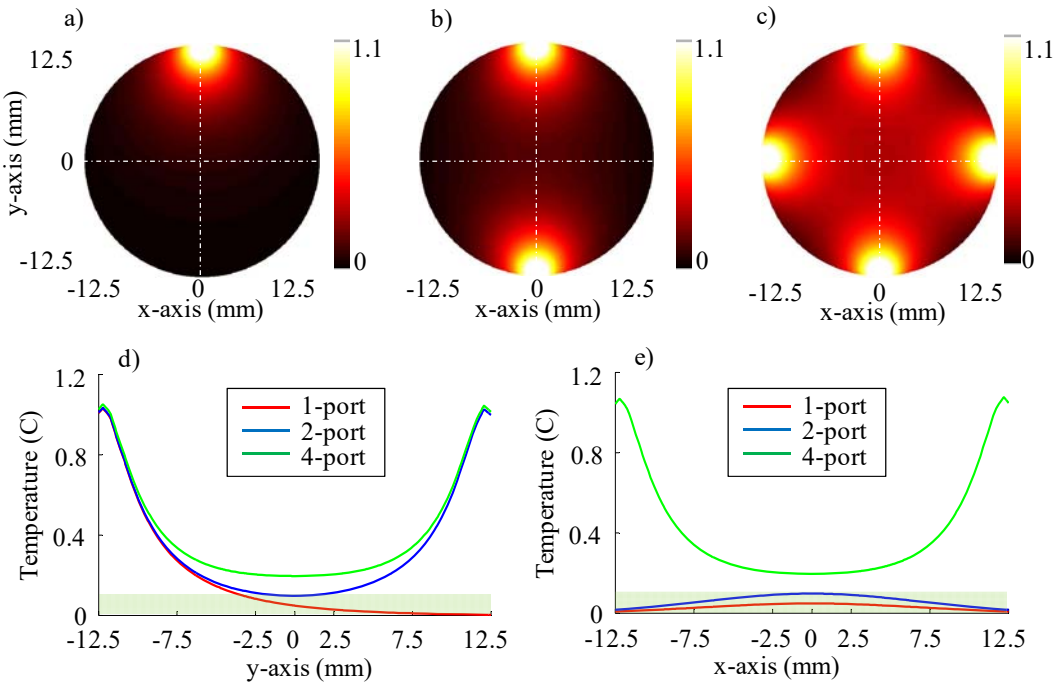

Figure 3.4 Temperature maps simulated when (a) one, (b) two and (c) four lasers are used. The temperature profiles along the (d) y-axis and (e) x-axis. The noise level of the MRT sequence corresponds to 0.1 ^{o}C (green highlighted). With only one laser illumination from the top of the phantom, the signals measured at the bottom half of the phantom is less than the noise level (red).When 2-port illumination are utilized, the measurements at the center of the phantom suffer from low SNR in the direction of illumination and mostly under the noise level in the orthogonal direction (blue). By increasing the illumination ports to four, this problem is solved and the SNR is increased in the overall phantom (green). [57]

3.3 PMI inverse problem [65]

Due to limited number of sources and detectors in conventional diffuse optical tomography system (usually 16-64), the non-linearity of the photon distribution, and challenges arising from the complex scattering properties of tissue; L-M method has been used. The reconstruction time of the conventional DOT system is also limited by the number of iterations needed. The most

time consuming bottle neck is to assemble the Jacobian for each iteration. As we have discussed in chapter 2 the PMI system Jacobian is extremely large and the reconstruction time for multiple iterations of L-M method of PMI will take more than 24 hours. To reduce the time for clinical study, we can decrease the number of iteration of PMI reconstruction. In this case we incur slightly lower reconstruction accuracy. But due to large number of "detectors" inside the PMI subject, the non-linearity of the photon diffusion behavior will not be severe at our resolution scale. This is because the detectors are very close to each other. In this case, we can solve the inverse problem of PMI with only couple iterations in which we approximate PMI as a linear problem. Even with one iteration we obtain a very accurate result compared to DOT. Figure 3.5 has shown the simulation result for different iteration of PMI reconstruction. As we can see the first iteration has already give a precise location for the high absorption inclusion bear inside the phantom. And the optical absorption coefficient has been recovered for 70% in the first iteration. In the second iteration, the edge of the inclusion has been sharpened and the optical absorption coefficient has been recovered for 95%. The L-M method will stop when two iterations change the reconstruction value less than 3%. In Figure 3.5, the fast reconstruction method integrated with analytical solution for forward problem has been compared with the first and second iteration of the conventional FEM PMI reconstruction results. Multiple iteration FEM reconstruction has shown sharper edge recovery and higher accuracy in mean absorption value in the inclusion comparing the first iteration. However, by integrating with the analytical solution introduced in chapter 2, the fast reconstruction shows similar accuracy comparing to multiple iteration FEM results.

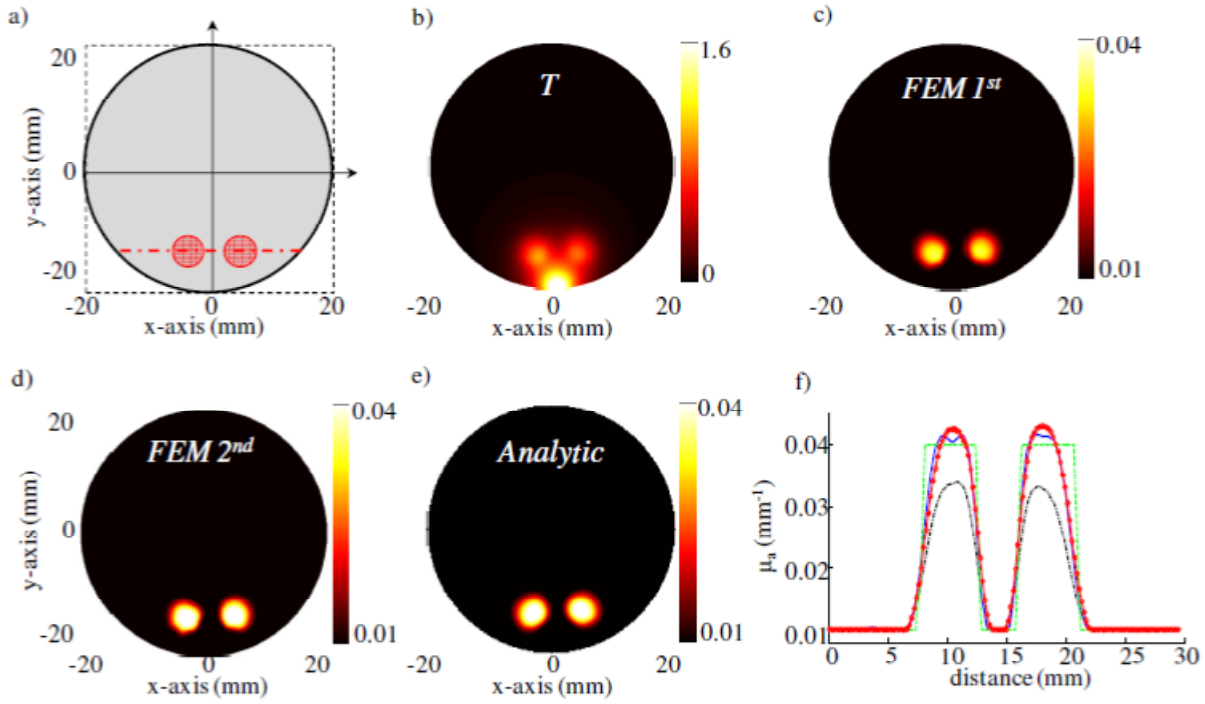

Figure 3.5 (a) Schematic of the double inclusion phantom. The two times more absorbent inclusions are shown with red circles while the limits of the pixel grid are shown in a black dashed line. (b) The synthetic temperature map simulated at the end of the heating cycle (8 seconds after turning on the laser). (c) The reconstructed absorption map using one iteration of the FEM-based algorithm. (d) The final reconstructed absorption map using the FEM-based algorithm. (e) The reconstructed absorption map using our analytic-based algorithm. (f) The reconstructed absorption profiles along the centers of the two inclusions: real (dashed green line), reconstructed using the new analytical method (red line with circle marker), reconstructed using one iteration of the FEM-based algorithm (dash-dot black line) and reconstructed at the final iteration of the FEM-based algorithm (blue line). [65]

3.4 Effect of adipose tissue on simulation results

The most relevant clinical application of PMI is breast cancer monitoring. However, due to the chemical frequency shift of the adipose tissue, proton resonance frequency shift MR thermometry is not accurate in these areas. This makes PMI more complicated in breast tissue monitoring. Owing to the density of adipose tissue in the breast, we either must use a different

MR thermometry method (independent to the lipid concentration), or we must take advantage of the MR structure information. This could be accomplished by using MR structure information as a priori information for the PMI reconstruction or using fat suppressed sequence to perform the MR thermometry. We can predefine the adipose tissue optical property before the PMI reconstruction. Figure 3.6(a) presents the MR image which can be used to define the fibrosis tissue and adipose tissue area. A 0.02mm-1 high absorption circle is set at the center of the breast as shown in Figure 3.6(a) to model the high absorption tumor tissue. Figure 3.6(b) is the temperature forward simulation with four side laser illuminations. The red arrows indicate the position of the laser source. Figure 3.6(c) presents the photon distribution in the breast and Figure 3.6 (d) is the first iteration PMI reconstruction excluded the temperature measurements at the adipose tissue area. As we can see in Figure 3.6(d) that with the MRI a priori information, even without the MRT measurement at the adipose tissue, PMI can still reconstruct the optical property accurately in the rest fibrosis area.

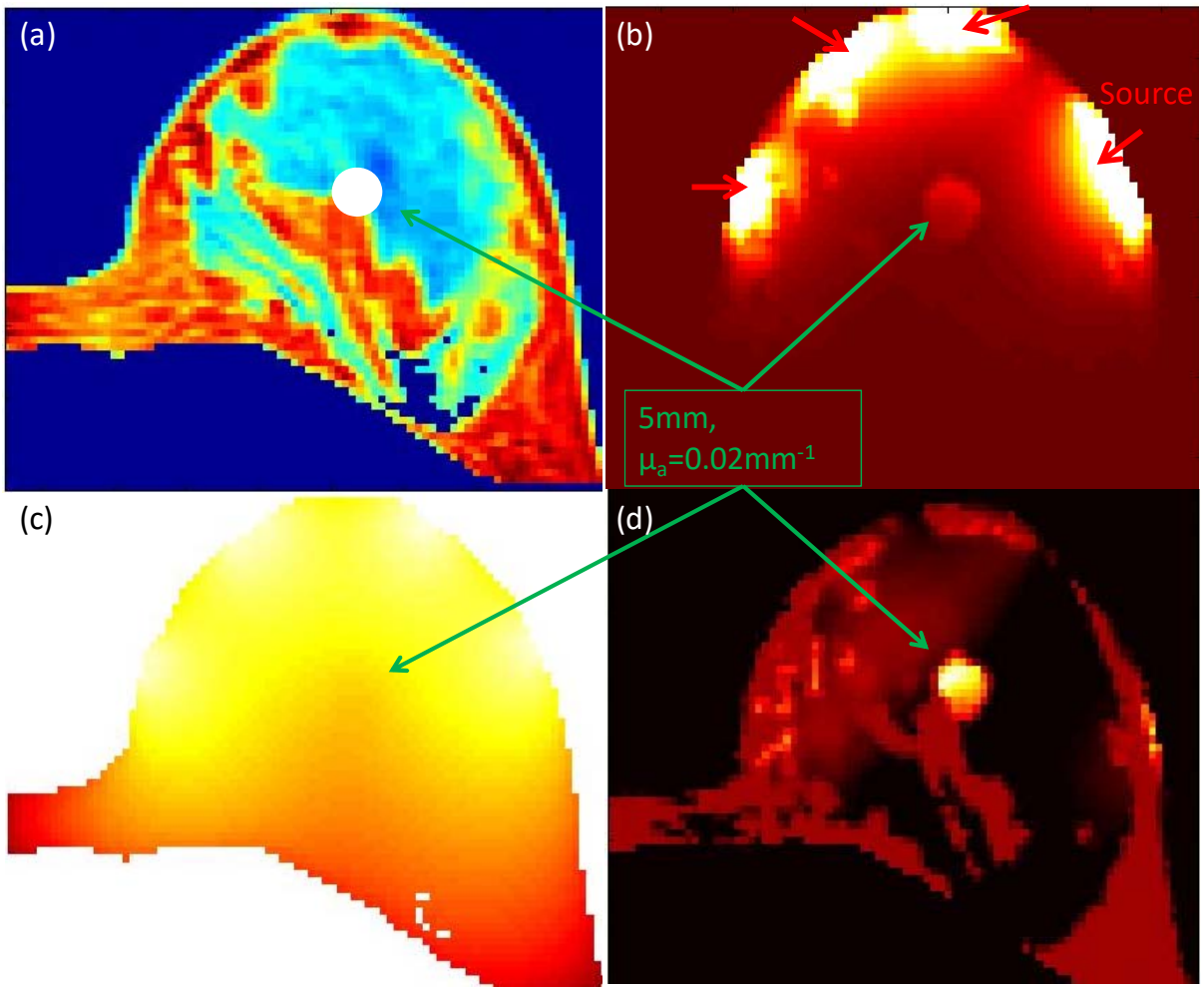

Figure 3.6 (a) shows a MRI anatomical image used to define the adipose tissue region and fibrosis tissue region and tumor region. (b) shows the temperature map simulated by FEM PMI forward solver with four laser sources which are indicated by four red arrows. (c) shows the photon distribution according to these lasers illumination as shown in (b). (d) shows the first iteration reconstruction using FEM based PMI reconstruction algorithm.

Chapter 4: Phantom design

4.1 Phantom preparation

4.1.1 Agarose gel phantom

An agarose gel in which the background's optical properties are tuned by varying intralipid and india ink concentration. A carefully mixed the agarose gel powder and DI water solution is placed on heated stir plate to further uniformly mix and slowly heat up to 92℃. Intralipid is mixed with the India ink in set concentration to achieve the specifications of the phantom. Gadolinium DTPA is added to shorten the magnetic relaxation time of the phantom thereby increasing the T1 signal of MR image. When the agarose solution temperature cools to around 50 degrees, the intralipid, ink and gd-DTPA mix is added to the agarose solution. The fully dissolved agarose powder mixture is cooled in a refrigerator to form the polymerized solid phantom. The solution should be free of bubbles before polymerization to prevent air gaps inside the phantom which will change the magnetic sustainability at the air/agarose interface and create a severe MRI artifact during data collection.

100ml, 0.01mm-1 absorption coefficient, 0.8mm-1 scattering coefficient phantom recipe:

1. Dissolve 2 grams of agarose gel powder into 93 grams of DI water.
2. Pour the solution into a beaker and place the beaker on magnetic auto mixer and heater.
3. Slowly heat up the solution up to 92 degrees and stirring the solution with the auto mixer to fully dissolve the agarose gel powder.

4. Cool the solution down to 60 degrees and continually stirring the solution to clear out the air bubble in the solution.
5. Mix 3.63 grams of intralipid with 0.35 grams of ink and 0.2grams of Gd-DTPA.
6. Put in the intralipid, ink and Gd-DTPA mix into the solution while it is around 50 degree and continually stir for one minute.
7. Pour the final solution into the mold and put the mold into the refrigerator at 4 degrees temperature for 90 minutes.
8. If there are embedded inclusions, prepare them separately with previous steps after finishing background phantom.
9. When doing the experiment, bring the phantom temperature up to 15 degree which is the MRI center temperature.

4.1.2 Chicken breast sample

Chicken breast is a fairly homogeneous bio sample which is very suitable to be used for PMI pilot image study. However, due to the magnetic susceptibility difference between chicken breast and the air, we must immerse the chicken breast in DI water to avoid MR image artifact and distortion at the edge of the chicken breast. The DI water will also fill the small air space we create when place the NMR tube inclusion. In the following experiment, we have prepared two type of chicken breast phantom. One is 25 -50 mm * 25mm diameter cylindrical phantom to mimic the mice size. The other one is a 40 mm * 80 mm * 50 mm breast phantom to mimic compressed woman breast.

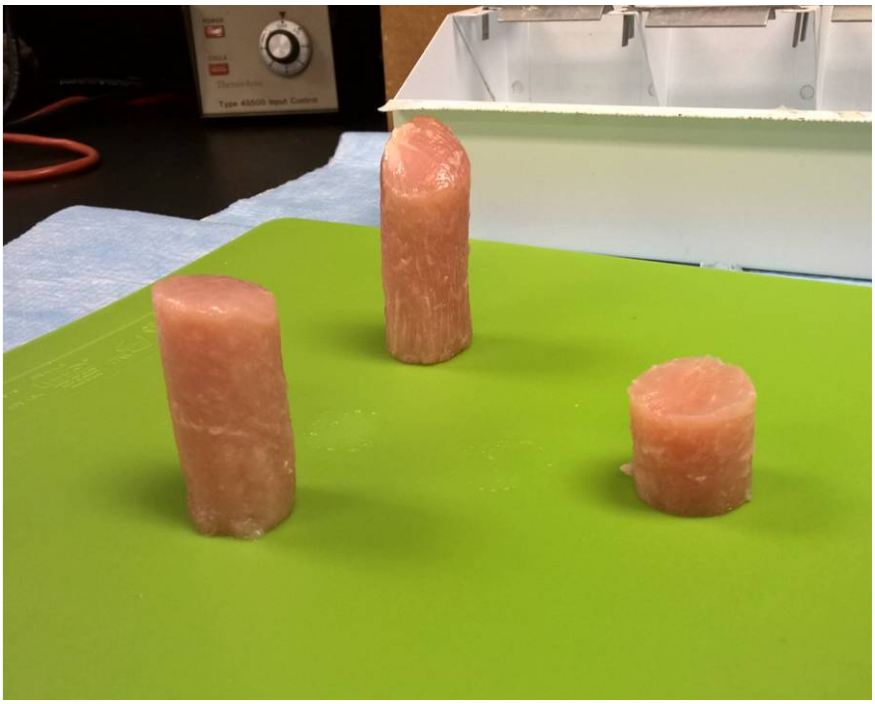

Figure 4.1 shows three different length 25mm diameter cylindrical chicken breast phantom

Figure 4.2 Chicken breast is immersed in the water in a transparent container.

Two kinds of inclusions have been used in the chicken breast phantoms. One is an NMR tube filled with high absorption agarose gel. The other is pure agarose gel. The NMR tube will give as

a perfect cylindrical inclusion and will not change shape of the chicken breast. The primary disadvantage of this will be a thin class boundary between the inclusion and the chicken breast. This small boundary may create some photon reflection and cause some inaccuracy in the PMI reconstruction. Also, the lack of MR signal in this thin region may be visible upon reconstruction. There will be some variability in the pure agarose gel inclusion. Such an inclusion may have elliptical shape due to deformation of the breast by gravity and could cause an air gap between the chicken breast and the inclusion. However, there will likely not be any photon reflection on the boundary. Also, since we are immersing the chicken breast into DI water, DI water will likely fill the small space between the inclusion and the chicken breast and mitigate the artifact.

4.1.3 Utilized Contrast Agents

One of the attractions of PMI is its ability to monitor molecular biomarkers. Many optical contrast agents have been used in the research. In this thesis work, we primarily use Indocyanine Green (ICG) and gold nanoparticle as our contrast agent for the PMI. ICG is the only FDA approved contrast agent and has high absorption coefficient at 808nm wavelength. ICG is a non-specific fluorescence contrast agent that can be used as a probe for tumor detection because it will accumulate via blood vessel leakage. Recent studies have already shown that ICG can enhance the tumor detection [84].

Gold nanoparticles have been extensively used in diagnostic imaging and therapy. Their bio-compatibility makes them suitable for *in vivo* studies. Also, they are used as a thermal therapy enhancer for laser ablation therapy [85]. Their optical absorption spectrum can be tuned by changing their size and shape, thus their surface plasmon resonance frequency shift. Gold

nanoparticles are frequently used as an imaging probe in cancer imaging [86]. They also can accumulate in tumors via the enhanced permeability and retention (EPR). Gold nanoparticles' accumulation in the tumors can be enhanced by conjugating them with specific ligands that can bond to receptors on the tumor cells. Moreover, gold nanoparticles can also be used as a drug delivery vehicle for cancer treatment. However, the uptake of gold nanoparticles in the regions of interest needs to be quantified.

Photo-Magnetic imaging is a potential solution for non-invasive molecular biomarker monitoring *in vivo*. Although the current PMI system only targets on 808nm wavelength absorbers, with multi-wavelength laser system, it can be easily used to monitor other near infrared wavelength contrast agents *in vivo*.

4.1.3.1 Gold nanoparticle

In this thesis work, we use gold nano rods from Nanopartz^{TM} as our gold nanoparticle contrast agent. Nanopartz^{TM} provides products covering 780, 808, 850, 980, and 1064 nm. Also, as they are coated in a proprietary layer of hydrophilic polymers that shield the gold surface, the contrast agent can have longer circulation times. It can also be designed to covalently conjugate to specific antibody for targeting.

4.1.3.2 Gd-DTPA

In the following works, we use Gd-DTPA (OmniscanTM, GE health, Princeton, NJ) to alter the T1 relaxation in the phantom which gives us higher signal in T1 weighted images.

Chapter 5: Experimental Setup

This chapter describes the detail of PMI systems, particularly for animal and human breast imaging. The details of the instrumentation, animal and breast PMI interface as well as details of the MRT procedures are outlined.

5.1 PMI Animal Imaging Interface

As explained earlier, PMI utilized MRI to measure the small temperature elevation due to abruption of NIR light. Therefore, it requires a suitable interface consisting of an rf-coil for MR imaging, several ports for NIR illumination, and a suitable sample holder. The experimental studies are performed in Philips Achieva 3T MR system available in Center for Functional Onco-Imaging. Figure 5.1.a shows a schematic of the custom designed animal PMI interface inside the 3T MR bore.

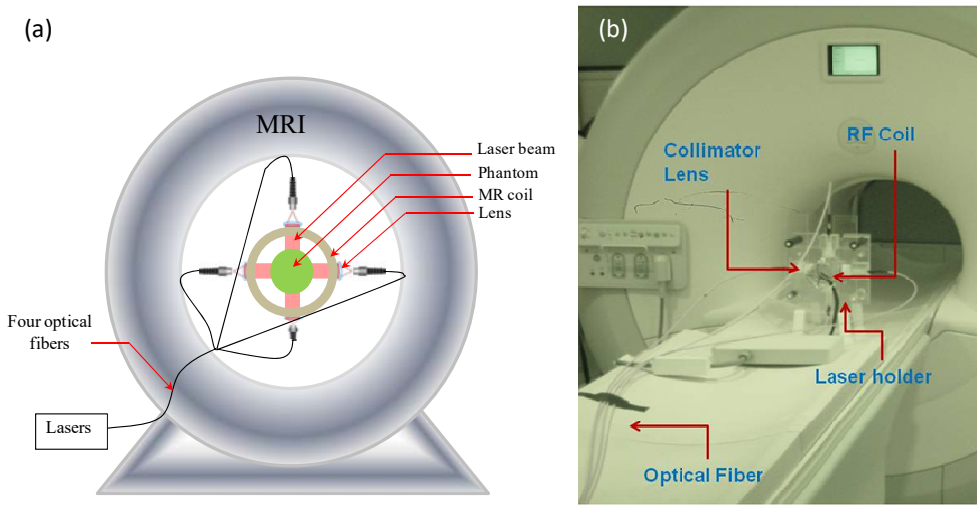

Figure. 5.1. a) The schematic of PMI setup that shows the phantom and the optical instrumentation inside the MRI bore. b) The picture of the PMI interface placed on the MRI bed.

The PMI interface has a custom designed RF coil at the center with four windows for illumination and four ports that hold the collimation optics. The rf-coil is designed for small animal imaging with a diameter of 7cm and length of 18 cm. It is unique in a sense that the rf circuitry is built to accommodate the windows for optical illumination without sacrificing the performance. Figure 5.2 shows the close-up pictures of the PMI animal interface from two different angles. The light in one of the illumination port is kept on using a visible laser for illustration purposes. The 25mm diameter agarose phantom is also placed in the center of the rf-coil as in the real experiments.

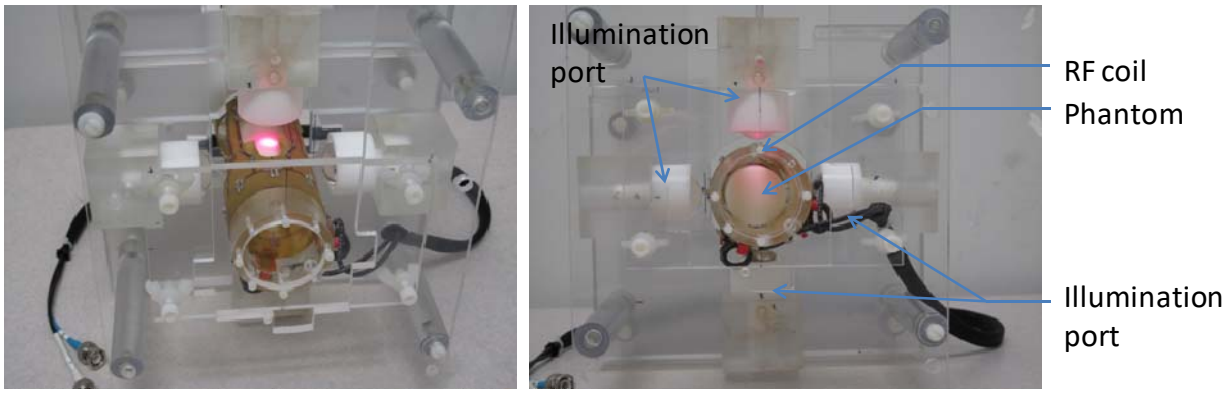

Figure. 5.2. a) The close-up pictures of the PMI animal interface. The rf-coil is placed at the center and has four windows for illumination. The interface also has four ports for illumination that corresponds to the windows. The collimation lenses are confined in the white plastic holders at each port. A visible laser is utilized at the top port to illuminate the phantom positioned at the center of the rf-coil for illustration purposes.

Seven watt laser diodes emitting at 808 nm (Focuslight, China) are used as light sources for illumination, Figure 5.3. The lasers are pigtailed with 200 μm diameter fibers that are coupled with SMA type connector. The laser diodes are driven by VueMatrix Vue-HCT controller with a 9A maximum output current. The maximum current setting is adjusted based on the laser power profile and required power level for a particular experiment.

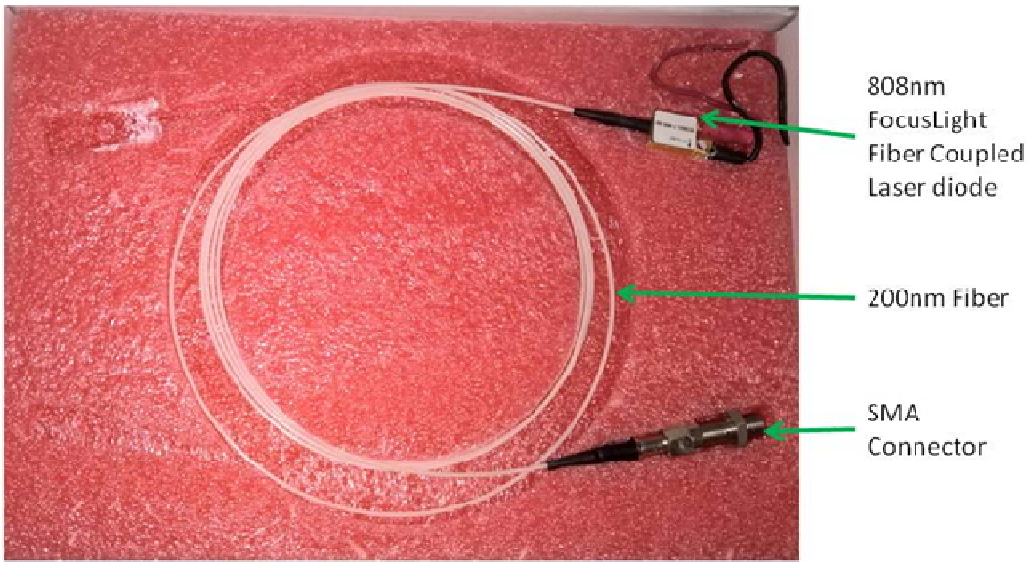

Figure 5.3. 808nm laser diode coupled to a 200nm diameter fiber with an SMA connector.

Since the lasers are high-power units, they need to be cooled to stabilize their light output as well as prevent any damage. For this purpose, all four lasers are placed on a copper heat sink (W:15cm, L:15cm, H:8mm) and four TEC cooling plates has been placed under this copper block. A thermo coupler is also embedded in the copper plate to monitor the temperature. Again VueMatrix Vue-HCT driver is used monitor the temperature of copper plate and provide current to TEC controllers to keep the temperature of the lasers constant during the operation.

The light output of the laser diodes are transported to the PMI interface located inside the MR bore using four 15-meter long, 1 mm diameter optical fibers. One end of the fiber is polished and attached with SMA optical connector which can be directly connected to the pigtailed laser diode, Figure 5.4. The other end of the fiber is polished and installed in a ceramic probe, which is MR compatible. The numerical aperture of the fiber is 0.22. The power loss at the SMA connection is around 15%, estimated by measuring the delivered power with and without 15m long fiber.

Figure 5.4. Light is transported to the PMI interface located inside the MR bore using 15-meter long optical fibers. One end of the fiber is polished and secured with a ceramic MR compatible probe (left), while the other end is coupled with an SMA type connector.

Once the light arrives to the PMI interface, it needs to be collimated prior illuminating the sample. For this purpose a 32.5 mm diameter aspherical lens, Newport Inc., has been used, Figure 5.5.c. The focal length of this collimator lens is 28.5 mm. Since the laser probe has a 0.22 numerical aperture, the laser spot size on the sample is nearly 14 mm. A MR compatible plastic holder is machined to hold the aspheric lens and the SMA connector at the end of the optical fiber, Figure 5.5.a. The connector is aligned with the lens and positioned at the focal length for optimum collimation. The large size of the lens permits for better collimation performance, i.e. a circular and homogeneous illumination. Additionally, a diffuser is placed after the collimating lens to make the pattern even more homogenous or change the laser spot pattern to other shapes if needed, such as a square pattern, Figure 5.5.c&d.

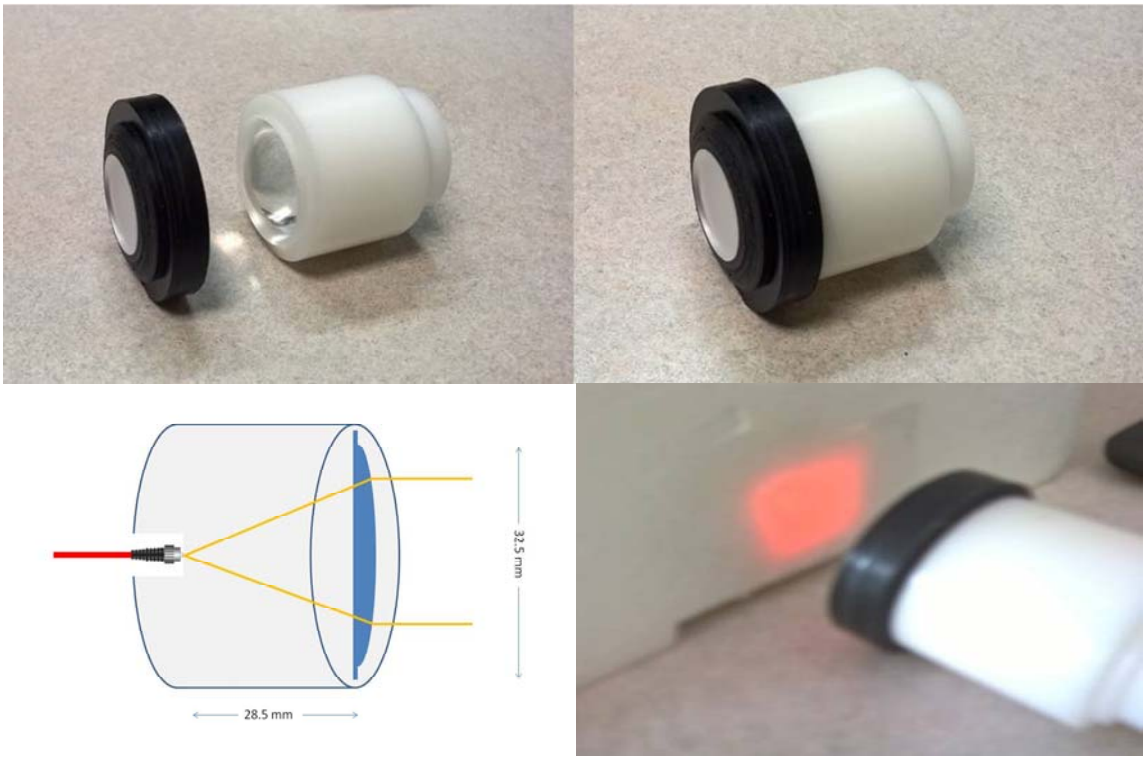

Figure 5.5 (a) The MR compatible plastic holder is machined to hold the aspheric lens and the SMA connector at the end of the optical fiber. A diffuser is placed after the collimating lens to make the pattern even more homogenous. (b) A black plastic holder secures the diffuser.(c) A 32.5 mm diameter aspherical lens is used to collimate the output of the fiber output. (d) The diffuser can be chosen to create any pattern such as a square illumination.

This animal PMI interface can illuminate the sample from four orthogonal angles, while the MRT measurements are acquired. This interface can accommodate small animals such as mice or rats. Indeed, PMI can provide an excellent platform for small animal imaging, particularly for understanding the disease progression and parameters related to diagnosis as well as monitoring the treatment. Furthermore, new optical contrast agents can be monitored using PMI. Hence, it has a great potential to contribute to the pharmacological science and nanotechnology.

5.2 PMI Breast Imaging Interface

For the clinical transition of the PMI, the first suitable application is breast cancer imaging. High resolution anatomic MRI and dynamic contrast enhanced MRI (DCE-MRI) has evolved into a standard approach for detection and diagnosis of breast lesions [87]. DCE-MRI acquires a series of images before and after administration of contrast medium to measure contrast enhancement kinetics. Tumors can be characterized based on their morphology and enhancement kinetics for diagnosis [88, 89]. In enhancement kinetics malignant tumors often show a rapid wash-in and wash-out pattern, while benign diseases often display a continuous enhancing pattern. The currently available MR contrast agents for clinical use are low molecular weight extracellular agents, which can diffuse freely from the vascular space into the interstitial space. Some benign lesions may also have high vascularity and high interstitial volume, thus may show malignant type enhancement kinetics and give false positive results and reduce the specificity of DCE_MRI. For these lesions, biopsy is the most common approach to characterize them but costs a great anxiety and morbidity to patients, and is very expensive.

Other adjunct imaging modalities that can better characterize the enhancing lesions on MRI, especially for young women with dense breasts, are greatly needed. For example, using near-infrared light, optical imaging can provide *in vivo* hemoglobin and oxygen saturation imaging for assessment of angiogenesis and metabolism. High total hemoglobin concentration is an indication of elevated tissue blood volume fraction while decreased oxygen saturation is of increased tissue oxygen metabolism, both are shown to be important parameters in differentiating malignant cancer and benign tumors [2]. There is also emerging data indicating that NIR scattering spectra are correlated to the normal composition of breast tissue, and that changes in breast physiology can be detected by variations in scattering spectra [90, 91].

Therefore, with all published promising data we hypothesize that additional information provided by optical imaging may be used in conjunction with morphological and kinetics parameters measured by DCE_MRI to improve diagnosis of breast cancer. Meanwhile, an accurate pre- and post-NAC disease staging is very important for selecting the optimal patients suitable for breast conserving surgeries without subjecting them to the high risk of recurrence [92]. Current methods for assessing treatment response include clinical examination (palpation), sonography, mammography, MRI, and molecular imaging. Among these, MRI has been proven the most accurate. The tumor size measured by MRI is highly correlated with pathological size after completing therapy, and early change of tumor size has been shown to be the most reliable response indicator [93]. Additional information provided by an add-on optical imaging system may not only help to assess treatment response better but also enable clinicians to evaluate the response of a therapeutic agent early and tailor the treatment regime early enough without losing much time.

Despite the promising results, the low resolution and quantitative accuracy have been the main barriers for translation of diffuse optical imaging into clinical arena, mainly due to highly scattering nature of the tissue. By providing high resolution images PMI can be an add-on to the currently available MRI systems. MRI is already the standard modality for clinical management for breast cancer and PMT will be a simple add-on due to its non-complex instrumentation, i.e. only laser source and optical fibers will be utilized and no optical detection system is required.

Due to these reasons, a breast PMI interface is also developed as seen in Figure 5.6. This interface utilizes the commercially available 3T breast coil. The idea is to lightly compress breast to have no more than 4 cm tissue thickness and illuminate the breast from both sides for PMI

imaging. For this purpose again collimating lenses is used on both sides as in the case of animal imaging.

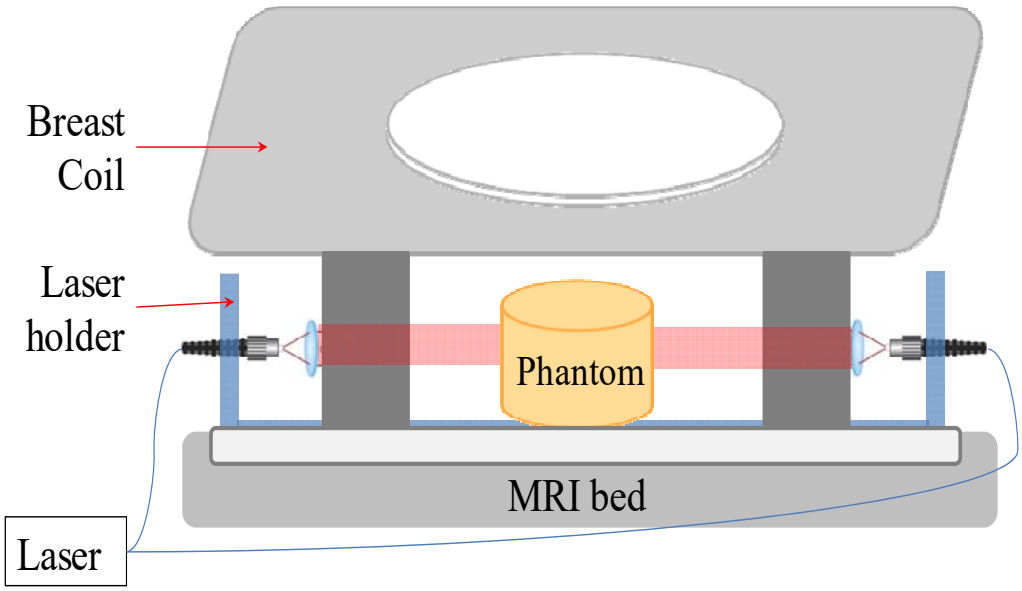

Figure 5.6 A schematic of the PMI breast imaging interface: the sample is placed at the center of the coil and illuminated from both sides. The light is transferred to the interface using optical fibers and collimated using aspherical lenses

5.3 PMI Data Acquisition

The laser-induced temperature variation is measured by MR thermometry using the proton resonance frequency shift method [MR thermometry]. Figure 5.7 shows the dynamic MR temperature acquisition timeline consisting of multiple frames with a temporal resolution of 8 seconds. First, the laser position in the axial direction is precisely located using a T1 weighted image using a fiducial marker. Following this, the dynamic MR temperature acquisition is initiated and the first phase map is acquired and used as baseline prior turning the laser on. Afterwards, the laser is turned on at the beginning of the second frame to warm up the medium

under investigation and dynamic MR temperature measurements are acquired for the following frames.

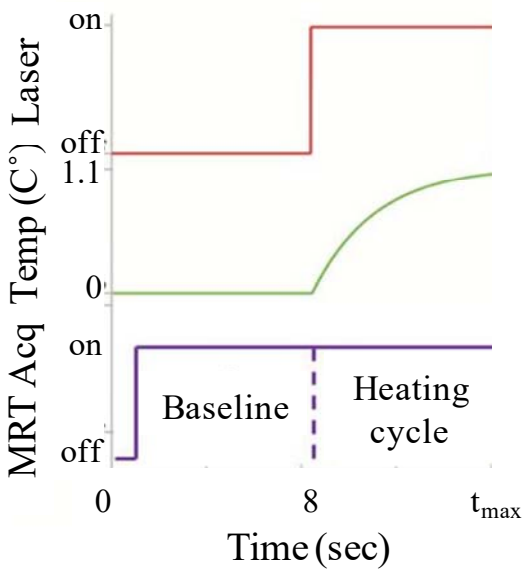

Figure 5.7. The timeline of PMI data acquisition, a MRT phase map is first obtained as a baseline temperature phase map. Then the laser is turned on and at the mean time acquires another temperature phase map during the laser heating period.

The laser induced temperature variation based on the phase shift between any frame and the baseline is calculated during the post processing step. The resulting temperature variation map is utilized during the PMI image reconstruction. In fact, each pixel of this image is utilized as an independent temperature measurement for the reconstruction algorithm [92]. The high resolution of the MRT images leads to high number of measurements that are available for the image reconstruction process. Covering the whole volume, these measurements produce high resolution optical absorption images that are quantitatively accurate.

5.4 Sensitivity of the MRT

To evaluate the sensitivity of the MRT, a 4cm*15cm*10cm agarose gel phantom has been used to characterize the linearity of the phase signal of the MRI gradient echo sequence versus temperature. The phantom is cooled down to 4 degree Celcius and placed at the center of MRI center with a MRI compatible fiber optic temperature probe. The agarose phantom is slowly warmed up by the room temperature and the temperature has been recorded by the MR compatible temperature probe once every two seconds. At the mean time, the MR thermometry has been performed to acquire the corresponding phase signal for duration of 20 minutes. As we can see in Figure 5.8, the phase signal difference linearly depends on the relative temperature change as expected. The phase noise calculated from this data is 0.01 degree that corresponds to ~0.1 degree K. Hence the MRT couldn't detect temperature changes below this level.

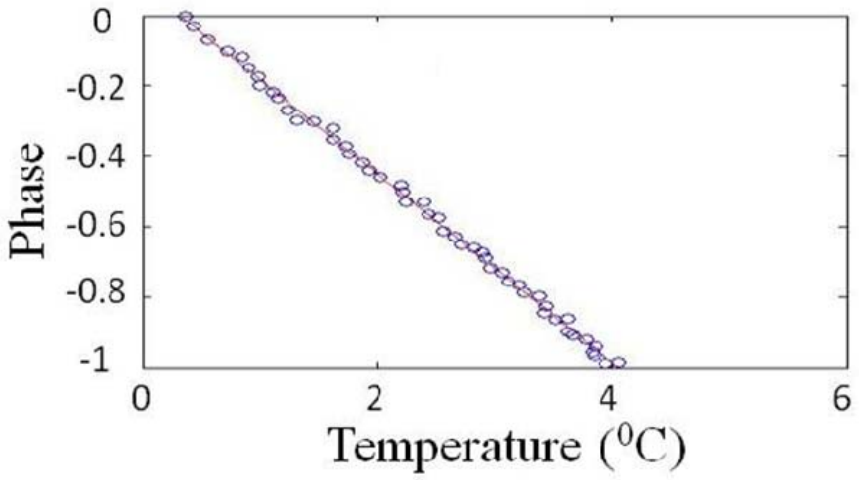

Figure 5.8 The phase changes obtained from the MR measurements versus the temperature measurements by the fiber optic probe. The temperature change was recorded over 30 minutes. The temperature of the agar phantom changed nearly 3 degrees due to the ambient temperature of the MR scanner room. The slope of this curve provided the calibration coefficient required to convert phase images into temperature maps. The linear trend over 30 minutes shows that the drift in the MRI phase measurements is negligible.

5.5 ANSI limit

American National Standard Institution (ANSI) has published laser safety standard in document z136 standards in 2000 and 2007. Our PMI laser power limits are based on the maximum permissible exposure (MPE) of skin suggested by the American National Standards Institute. For pulse duration of 10 seconds, the MPE of skin can be calculated with the following formula: $MPE = 1{,}1.C_a.t^{0.25}$ (J/cm^2), where C_a =1.64 at 808 nm. The safety limit of laser fluence on the tissue during these 10 seconds is 3.2 J/cm^2. The average power per centimeter square is 320 mW. In the experiment, the laser power was kept under 320 mW/cm^2 based on this ANSI safety limit value.

5.6 Image Reconstruction

After collecting the MRT data from the MRI system, the raw image data will be sent to a personal computer for photo-magnetic imaging reconstruction. The matlab based PMI reconstruction program will first convert the MRT phase data into temperature map and then use the high resolution MR anatomical image to create a corresponding FEM mesh for the subject. Manually or automatically laser source position alignment of the subject will be fitted for the FEM simulation. After the program define the laser source pattern at the boundary of the subject, it will start to reconstruct the optical absorption map of the volume under investigation from the temperature map. Figure 5.8.a shows state diagram of PMI as we describe above. To obtain high accuracy reconstructed optical absorption map, the final state need to run a couple more times.(more iterations) To realize “real time” PMI in clinical study, the final status needs to be done as fast as MRT acquisition time which is 6-24 seconds. This will require the fast

reconstruction algorithm as derived in Chapter 2. But even with the fast reconstruction algorithm, PMI can only finish one iteration in this time range. To further speed up PMI reconstruction for high accuracy real time imaging, GPU acceleration is needed with the current system

Chapter 6: Preclinical PMI experiment results

6.1 Introduction

Many studies had to be done before the *in vivo* small animal studies could take place. Indeed, before any live animal studies could be considered, the small animal PMI system had to be thoroughly tested and characterized in phantoms. Then the system had to be translated and optimized for *in vivo* animal imaging. This chapter will report on the development of the preclinical PMI system from feasibility studies to *in vivo* animal results.

6.2 Phantom studies

A number of intensive phantom studies were performed to test the performance of PMI and optimize it for small animal imaging. An agar cylindrical phantom (25 mm diameter and 70 mm in length) was used to mimic the size of a rat in all the phantom studies in this chapter. We first started with a proof of concept study to confirm that PMI was feasible and compared it to FEM to validate our modeling theory. Once this PMI technique was confirmed, we characterized the system in test its ability to accurately recover the correct optical contrast, size dependence, and depth dependence. Next, we studied the performance of PMI to recover the absorption of complex heterogeneous phantoms with high spatial resolution. Finally, we studied how external contrast agents can be used to enhance the SNR of PMI.

6.2.1 Feasibility study: proof of modeling theory

A simple proof of concept study was done to validate that PMI was feasible and that our mathematical modeling was correct. In this study, a simple homogeneous phantom was use to demonstrate the ability of PMI to measure the change in temperature from the absorption of the laser photons with high spatial resolution using MRT. To validate our modeling method, the experimental results were compared with the analytical solution and FEM to verify the practicality of our FEM forward solver as described in Chapter 2.

6.2.1.1 Phantom Preparation

A simple homogeneous phantom was used for this study. This agar phantom is cylindrical in shape and 25 mm in diameter and 70 mm in length. This homogenous phantom consists of 2% agarose, and made to have an absorption coefficient 0.01 mm^{-1} and a scattering coefficient 0.8 mm^{-1}.

6.2.1.2 Experimental parameters

To test the feasibility of this technique, the phantom was illuminated by a single 1 mm diameter laser probe (808 nm). A GRIN lens collimated the beam to illuminate the laser beam homogeneously at the center of the phantom surface as seen in Figure 6.1. The MRT experiments are conducted inside a Philips 3T Achieva system and data acquisition is synchronized with the laser driver.

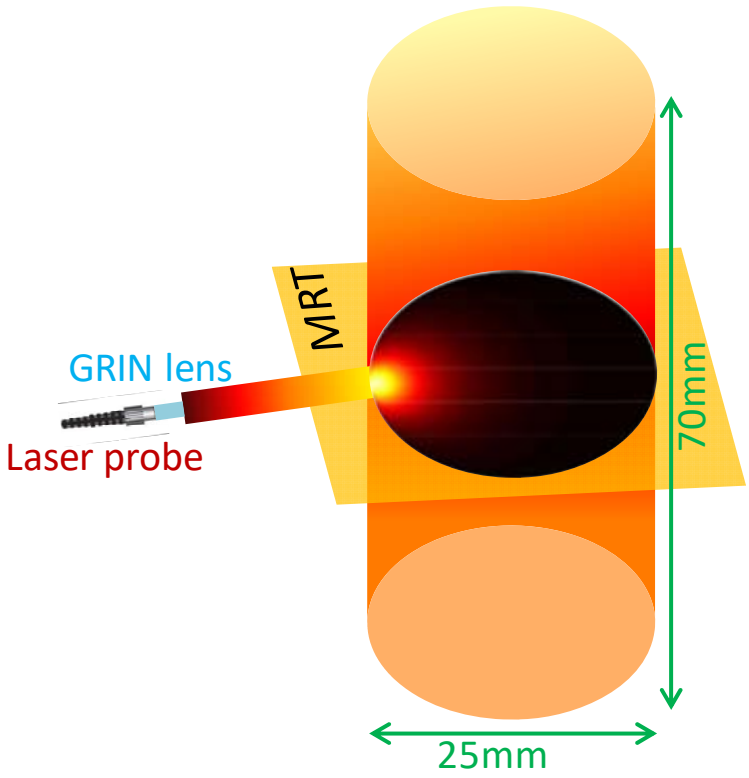

Figure 6.1 shows the phantom setup in this experiment. A GRIN lens is used in this experiment for smaller spot size which can be modeled as a point source at the boundary.

6.2.1.3 Experimental procedure [5]

The MRT measurements are performed using a phase sensitive technique, PRFS. In this experiment, PRFS images are obtained with a gradient echo sequence using a 60 and 12 ms repetition (TR) and echo time (TE), respectively. First, a T1 weighted low resolution MR pilot image is obtained to determine the axial position of the laser probe using markers placed at the laser probe. After the axial plane is located, a baseline high resolution phase image (ϕ) is obtained using a gradient echo scan. Next, the phantom is illuminated by the laser beam for 24 seconds while two consecutive MRT images are acquired, each lasting 12 seconds. The difference between the corresponding phase maps for these two time points and the baseline

phase image provide a high spatial resolution temperature image of the relative temperature increase induced by the laser illumination.

Technically, the local phase measured by the MRT for each time point is an average value for the duration of the data acquisition for that time point, 12 s. Conversely, our simulation studies provide synthetic temperature distribution at a specific time point. To compensate for this, since the experimental data that corresponds to the second time point (12 s - 24 s) is used for analysis, these results are compared with the simulation temperature results obtained at t = 18 s, the midpoint for the MRT acquisition.

6.2.1.4 Experimental results [5]

Figure 6.2 shows the cross-sectional high spatial resolution temperature maps corresponding to the optical fiber plane obtained (a) experimentally (b) analytically and (c) numerically (FEM). As specified in the experimental method, the temperature map provided by MRT does not represent the absolute temperature but the relative increase in temperature induced by the laser. Thus, the room temperature, 14°C, is subtracted from the absolute synthetic temperature maps in order to compare with the experimental one.

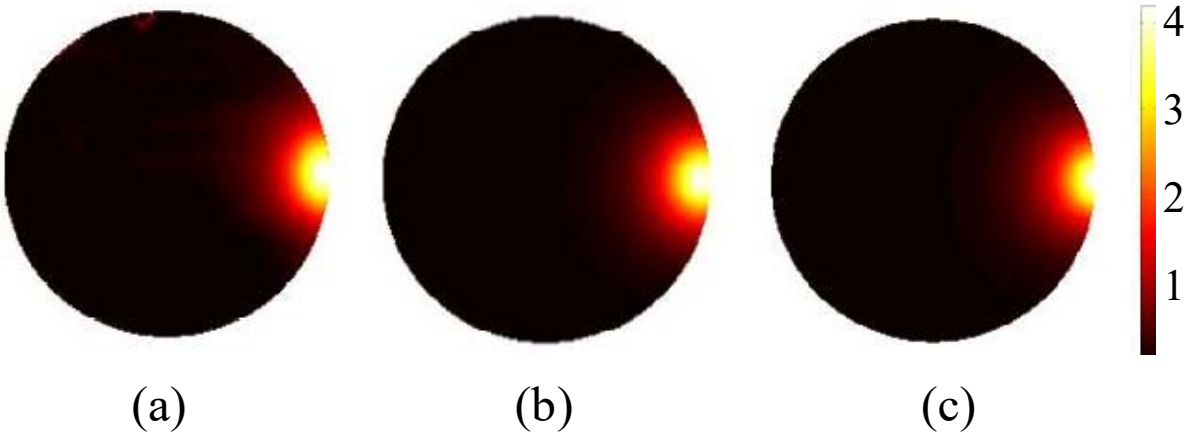

Figure 6.2 Temperature map (°C) of 25 mm diameter circular phantom which is obtained (a) experimentally, (b) analytically and (c) numerically (FEM). The unit of the color bar is in degree Celsius. [5]

Although there are some slight artifacts at the upper boundary of the phantom in the measured temperature map, Figure 6.2.a, nevertheless, this measured temperature map is in very good agreement with the simulated temperatures maps. As expected from the photon diffusion approximation, the highest increase in temperature is observed near the source of light positioned at $\theta=0$ and at $r_i = R-1/\mu_s'$, where R is the radius of the phantom at 25 mm and μ_s' is the reduced scattering coefficient, and decreases in temperature in a radial manner when further from the light source.

For a better comparison of these results, the logarithm of temperature profiles carried out along the x axis can be seen in Figure 6.3. Overall, Figure 6.3 shows the high correspondence between the theoretical, FEM, and experimental results. The experimental results showed excellent agreement with FEM and the analytic result close to edge of the phantom where the temperature increase was the largest but deviated when measuring further from the source

position where the temperature increase was small. However, above the noise level of MRT at 0.1°C, the results were in excellent agreement.

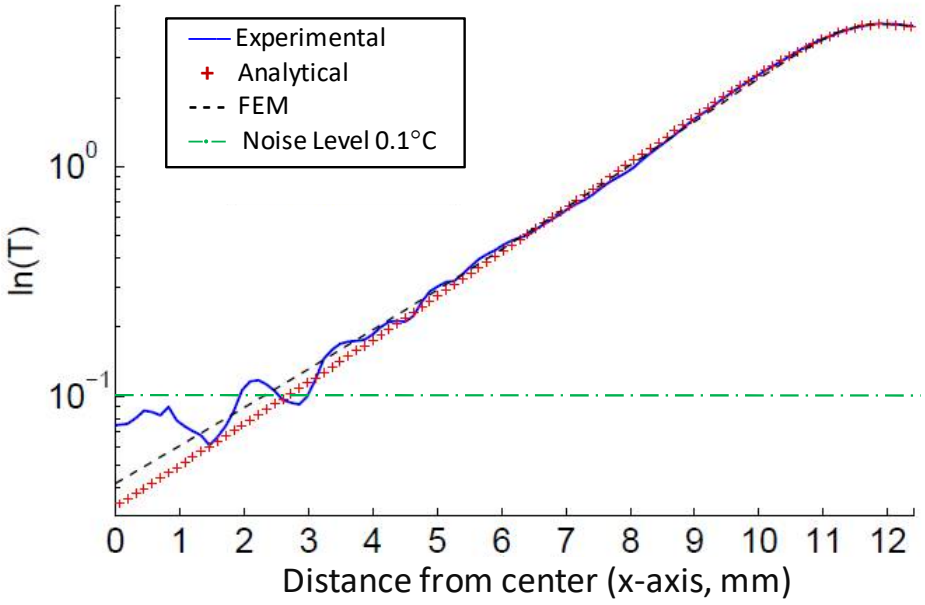

Figure 6.3 Logarithmic temperature profile T (^{0}C) vs. x (mm) for the phantom with the source placed near the boundary at 12 mm. Solid line (blue), red +, and dash line (black) represent the experimental, analytical and FEM results, respectively. Good agreement between the three methods above the MRT noise level at 0.1 °C (green dot dash line). [5]

It is also important to notice that there are some limitations to our FEM and analytical solution approach. Firstly, the diffusion approximation is valid when the distance is larger than the $1/\mu_s'$, ~1.2mm. Secondly, the approximation is also only valid if the scattering coefficient is larger than absorption coefficient. Thirdly, the analytical solution method can be used for regular geometries.

6.2.2 Phantom Study 1: evaluation of system linearity [57]

To characterize and evaluate the limitations of the PMI system, a number of phantom experiments were performed. For traditional optical imaging methods such as DOT, the accuracy of this technique is strongly affected by the SNR. Errors increase when the contrast signal compare to the background is low. This results in poor spatial resolution and quantitative accuracy. In this first study, we evaluated whether PMI can accurately the correct absorption when the contrast is low.

6.2.2.1Phantom preparation

In this experiment, four different optical absorptions were measured. Four 5 mm diameter inclusions were embedded 5 mm beneath the edge of the 25 mm cylindrical agarose phantom (background optical properties: μa= 0.01mm-1, $\mu s'$=0.8mm-1) at the same distance, as seen in Figure 6.4.c. Approximately 5 mm below the surface of the phantom. The optical absorption of the inclusions are set to be 2x (0.02mm-1), 4x (0.04mm-1), 6x (0.06mm-1), and 8x (0.08mm-1) higher than the background optical absorption of the phantom at 0.01mm-1. Taking the same inclusions size and distance under the surface for all inclusions reduces the size and depth dependence errors and allows us to focus on the ability of PMI in resolving inclusions with different contrasts.

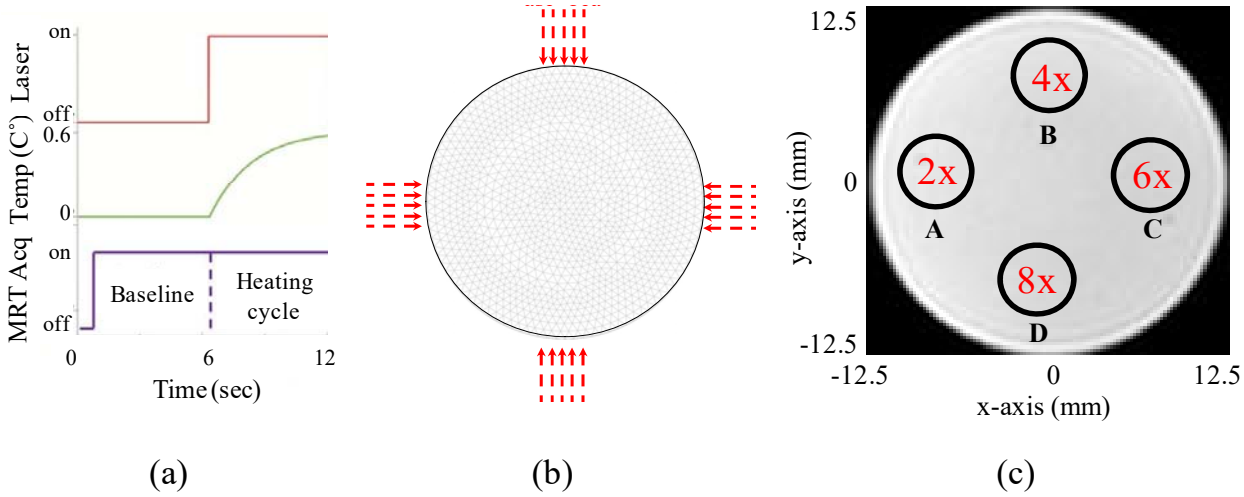

Figure 6.4 (a) PMI data acquisition timeline: the temporal resolution of the dynamic MRT sequence is 12 seconds. The laser is turned on after the first MRT baseline image, and several images are acquired during this heating-phase as the temperature of the medium rises (b) FEM mesh of phantom and laser positions (red arrows). (c) Axial MRI of the cylindrical phantom. The size and position of the four 5 mm diameter inclusions with different absorption contrast is delimited with the black circles since no absorption contrast can be seen on the MRI image. The inclusions are 2, 4, 6 and 8 times more absorbent than the background and are all placed at the same distance from the laser source and edge of the phantom. [57]

6.2.2.2 Experimental procedure

The following phantom studies were all performed inside a Philips 3 Tesla Achieva system. PRF images are acquired using a gradient echo sequence using 60 and 12 milliseconds as repetition (TR) and echo time (TE), respectively. The illumination of the phantom is realized using four 7-watt laser diodes emitting at 808 nm. Figure 6.4.a shows the timeline of data acquisition. First, a T1 weighted low resolution MR pilot image is acquired to localize the axial position of the laser probe. Once the axial plane located, a dynamic imaging set consisting of multiple frames (6 seconds each) is initiated. A gradient echo sequence is used to obtain a high resolution phase image at each time point. The first baseline frame (ϕ_0) is acquired before the laser is turned on. After the lasers are powered, the phantom is illuminated simultaneously from four sides during the heating phase, and another frame is acquired (ϕ_i), Figure 6.4.c. The total

PMI data acquisition time is nearly 12 seconds. After subtracting the baseline image (ϕ_0) from the image acquired during heating phase (ϕ_i), relative phase change for each pixel can be obtained and hence, a high resolution image describing the temperature increase can be attained. In fact, each pixel of this image serves as a measurement point to monitor the temperature increase.

6.2.2.3 Results

The results of the contrast resolution phantom study are seen in Figure 6.5. The temperature map can be seen in Figure 6.5.a. From this alone, without any further processing, the difference in the absorption contrast between the four inclusions can be seen. However, to get a high spatial resolution and quantitatively accurate image, the inverse problem must be solved. Figure 6.5.b shows the reconstructed absorption map which represents a high resolution PMI image of the phantom. This map shows an excellent agreement with the real absorption map presented in Figure.6.5.c.

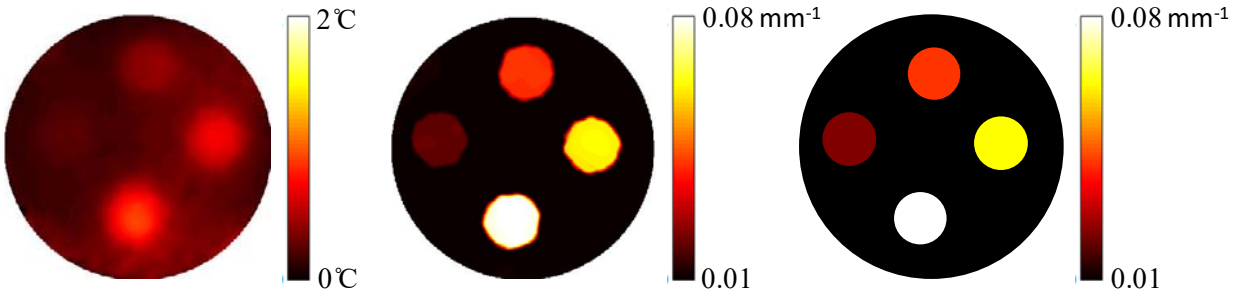

Figure 6.5 (a) Axial MRI of the cylindrical phantom. The size and position of the inclusions are delimited with the black circles since no absorption contrast can be seen on the MRI image. The inclusions are 2, 4, 6 and 8 times more absorbent than the background. (b) The PMI absorption reconstructed map. (c) The true absorption map of the subject. [57]

The results of this experiment are summarized in Table 1. The sizes of all four objects are recovered with less than 4% error. Similarly, the errors in the recovered absorption coefficients are all below 6.25%.

Table 1 Summary of contrast phantom study results. [57]

	Inclusion A		**Inclusion B**		**Inclusion C**		**Inclusion D**	
	True	**PMI**	**True**	**PMI**	**True**	**PMI**	**True**	**PMI**
Diameter (mm)	5	5.1	5	4.9	5	4.8	5	4.8
***% error* Diameter**		2 %		2%		4%		4%
μ_a **(mm^{-1})**	0.02	0.019±0.001	0.04	0.040±0.002	0.06	0.059±0.002	0.08	0.075±0.004
% error μ_a		5.00%		0%		1.67%		6.25 %

Figure 6.6 shows the linear proportional relationship between the reconstructed and true absorption coefficient. The results of this study show that the system response is linear and demonstrates the high performance of PMI in recovering all four contrasts.

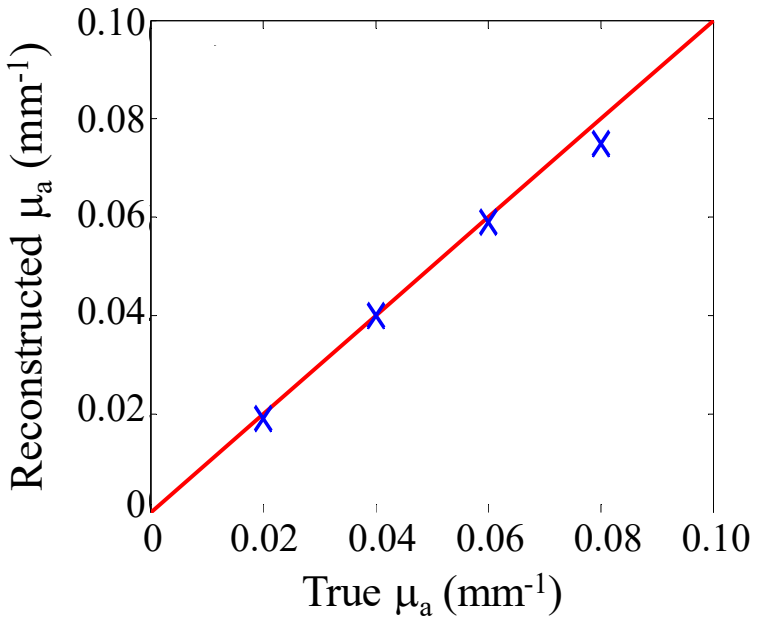

Figure 6.6 Linear proportional relationship between the reconstructed and true absorption coefficient. [57]

6.2.3 Phantom study 2: evaluation of spatial resolution

In this study we evaluated the size dependence of the PMI system. A smaller sized inclusion results in a smaller contrast signal and makes reconstruction extremely challenging. In this study, four inclusions of different sizes were compared.

6.2.3.1 Phantom preparation

In this case, four inclusions with different sizes are embedded approximately 6 mm deep into the 25 mm diameter cylindrical agarose phantom (background optical properties: μa= 0.01mm-1, μs′=0.8mm-1). The four sizes of the inclusions are 1.0, 1.5, 2.0 and 3.0 mm diameter as shown in the cross-section of the phantom presented in Figure 6.7. In order to evaluate the ability of PMI in resolving inclusions with different sizes, we first chose the same optical

absorption coefficient for the four inclusions and set it to be four times higher than the absorption of the background. Second, all four inclusions are placed at the same distance (6 mm) from the surface of the phantom. This ensures that each inclusion is at the same distance from the edge under the illumination it in order to limit the depth-dependence of the heating results.

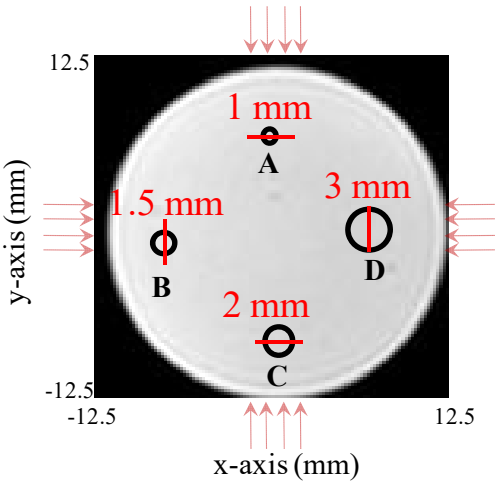

Figure 6.7 Axial MRI of the cylindrical phantom. The size and position of the inclusions are shown in black circles since no absorption contrast can be seen on the MRI image. All four inclusions have the same absorption 4 times the background and are all placed at the same distance from the laser source and edge of the phantom. The four laser positions are shown by the red arrows. [57]

6.2.3.2 Experimental parameters

This phantom study was performed using the same parameters and procedures as described in section 6.2.2.2.

6.2.3.3 Results

Figure 6.8 shows the results of the size dependence phantom study. From Figure 6.8.a, the inclusions can vaguely be distinguished from the temperature map alone. However, the results of the Figure 6.8.b shows the high resolution absorption map obtained after solving the PMI inverse problem. The inclusions are recovered successfully on the reconstructed absorption

map and their location shows a very good agreement with the true absorption of the phantom as seen in Figure 6.8.c.

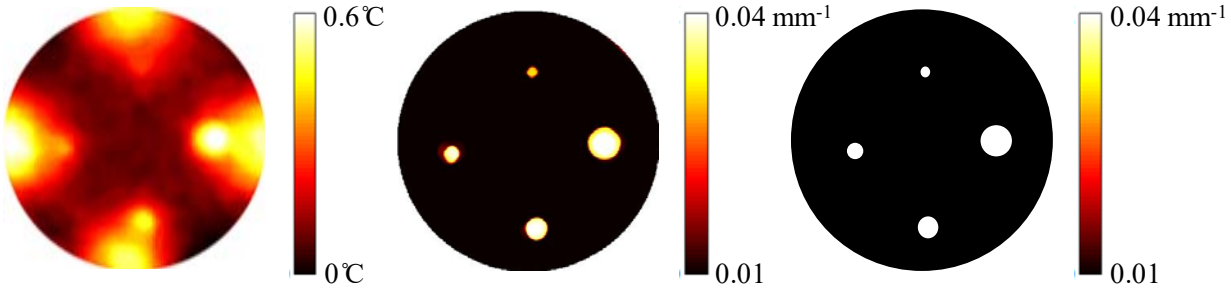

Figure 6.8 a) Temperature map of phantom at the end of the heating cycle. b) The PMI absorption reconstructed map. c) True absorption reconstruction map. [57]

Figure 6.9 shows the four reconstructed absorption profiles taken along the red lines across each inclusion as shown in Figure 6.7. The similarities in profiles between the true and those recovered with PMI show the accuracy in recovering the sizes and contrasts of the inclusions.

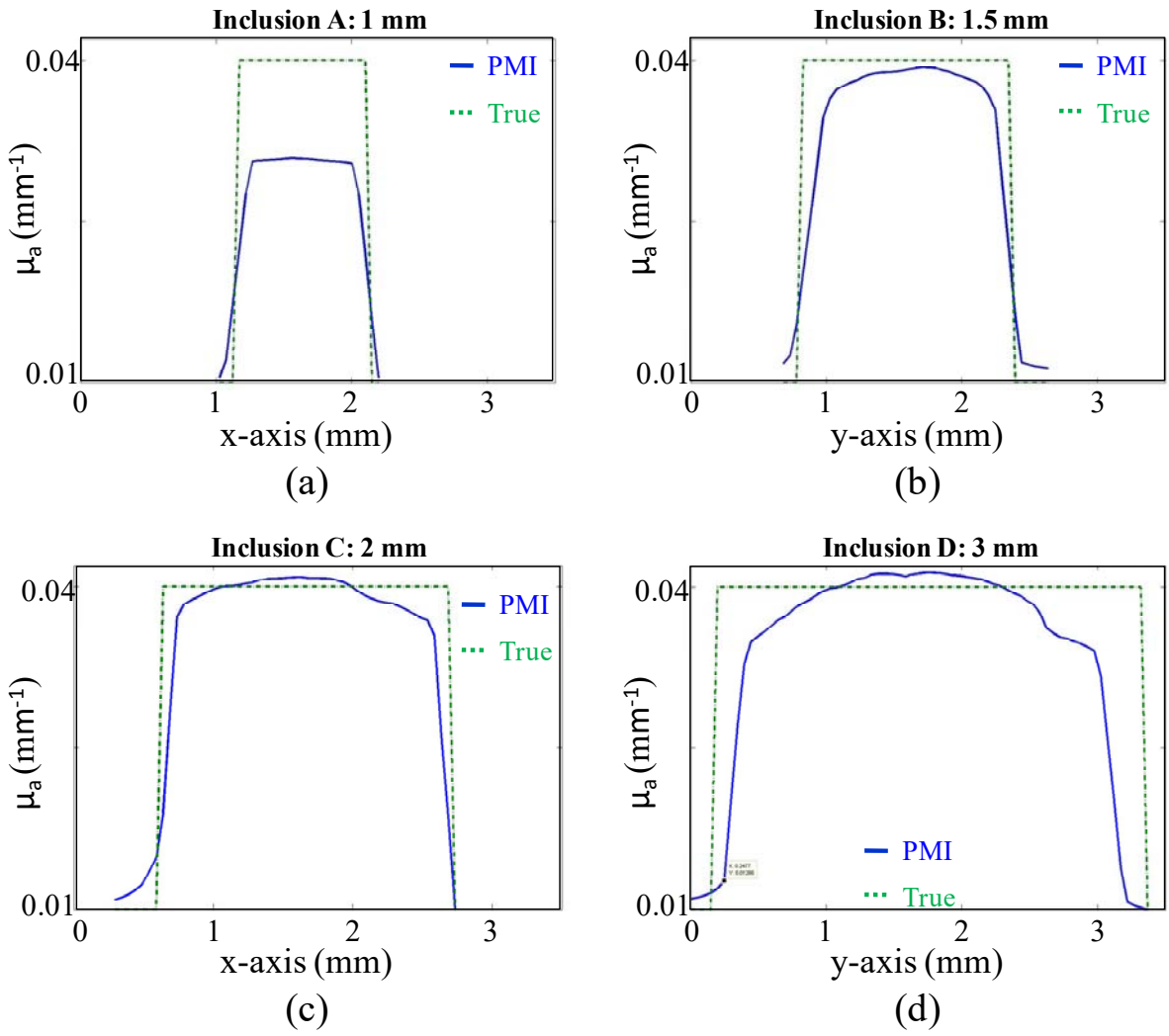

Figure 6.9 Comparison of true and recovered size of inclusions with PMI. Absorption profiles across the four inclusions along the red lines shown on Fig 5(a) for a) 1mm, b) 1.5 mm, c) 2 mm, and d) 3mm.

Table 2 summarizes the results of the experiment. From this table its can be noted that there is a slight trend where the error in the recovered size and absorption increases for smaller sized inclusions. The sizes of the two largest objects (2.0 mm and 3.0 mm) are recovered perfectly, while their absorption coefficients are recovered with only 2.5% error. When the size of the inclusion is decreased to 1.5 mm diameter, the error in the recovered size is slightly larger at 7% while the error in the recovered absorption increases to 5%. This error increases to 10% error in size and 22.5% error in the recovered absorption when the size of the inclusion is

smallest at 1 mm. Although some of the error can be attributed to the low SNR, this can be alleviated by improving the spatial resolution of the PMI system. In fact, since the pixel size of the MRT image is set to 0.8 mm, the higher error in the recovered absorption coefficient of this 1 mm small inclusion is well expected. However, it is important to notice that although the size of this inclusion is very close to the MRT pixel size, it is accurately localized. This problem can be easily overcome by decreasing the size of the MRT pixel size but in expense of PMI temporal resolution and computation time.

Table 2 Summary of the size dependence phantom results. [57]

	Inclusion A		**Inclusion B**		**Inclusion C**		**Inclusion D**	
	True	**PMI**	**True**	**PMI**	**True**	**PMI**	**True**	**PMI**
Diameter (mm)	1	1.1	1.5	1.6	2	2.0	3	3.0
% error Diameter		10.0%		6.7%		0.0%		0.0%
Mean μ_a (mm^{-1})	0.04	0.031±0.001	0.04	0.038±0.001	0.04	0.039±0.001	0.04	0.039±0.003
***% error* μ_a**		22.5%		5.0%		2.5%		2.5%

6.2.4 Phantom study 3: evaluation of depth dependence

In traditional DOT, due to the high absorption and scattering of biological tissue, photon penetration is severely limited and recovery of the absorption because more challenging the farther away from the surface. In this study the depth dependence of the PMI system is studied.

6.2.4.1 Phantom preparation

In this experiment, three 2.5 mm diameter inclusions were placed at three different depths in the 25 mm cylindrical animal phantom (background optical properties: μa= 0.01 mm^{-1}, μs′=0.8 mm^{-1}). All three inclusions were prepared with the same absorption coefficient, 0.04

mm^{-1}, four times higher than the absorption of the background. The inclusions are placed in a line at different depths (3 mm, 7.5 mm, and 12 mm) beneath the surface of the phantom as shown in Figure 6.10.

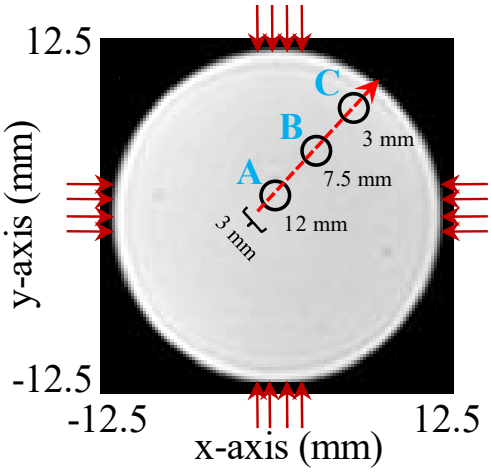

Figure 6.10 Axial MRI of the cylindrical phantom. The size and position of the inclusions are shown using black circles since no absorption contrast can be seen on the MRI image. All inclusions have the same contrast set to four times more absorbent than the background. The four laser positions are shown by the red arrows. [57]

6.2.4.2 Experimental parameters

This phantom study was performed using the same parameters and procedures as described in section 6.2.2.2.

6.2.4.3 Results

Figure 6.11.a shows the measured temperature map obtained using MRT. This map clearly shows the increase in temperature induced by the laser under the illumination sites. The temperature increases at the four illumination sites are not identical due to the different power output levels of each port as well as variation in spot size. In practical applications, the sample will not be perfectly circular and hence the spot size as well as the power density might be different at each illumination site. Due to this reason, for each laser port, a unique power and

spots size were set to model a realistic case. PMI calibration measurement is first performed on a homogenous phantom with known optical and thermal properties. This calibration measurement is utilized to find the differences at each illumination site and hence to figure out any mismatch between the experiment and the simulation parameters by minimizing the objective function, Eq.(13) in chapter 2.

Even without any calibration, Figure 6.11.a shows that the temperature map already reveals the position of the three inclusions prior to any reconstruction process. In fact, due to their higher optical absorption, the temperature increase is higher inside the inclusions. However, strong depth dependence is observed even though the three inclusions have identical size and contrast. This can also be observed in Figure 6.12 which shows the temperature and absorption profile along the red arrow shown in Figure 6.10. The depth dependence is clearly seen in the unprocessed temperature profile (blue line).

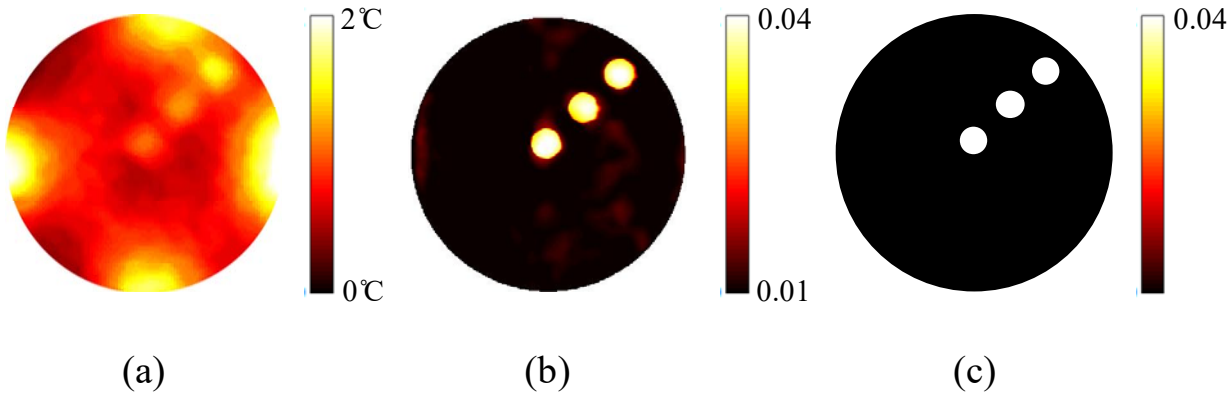

Figure 6.11 a) The temperature map at the end of the heating cycle. b) The PMI absorption reconstructed map. c) True absorption map. [57]

In order to overcome the depth dependence, and obtain quantitative absorption maps, the PMI inverse problem is solved. Figure 6.11.b shows the reconstructed absorption map when the measured MRT temperature map is used as the input for the solver. The three inclusions are resolved accurately and their absorption coefficients are recovered without any depth

dependence. Indeed, the three reconstructed inclusions have an average error of 4% in diameter and less than a 7.5% in the recovered absorption coefficient. The obtained results are summarized in Table 3.

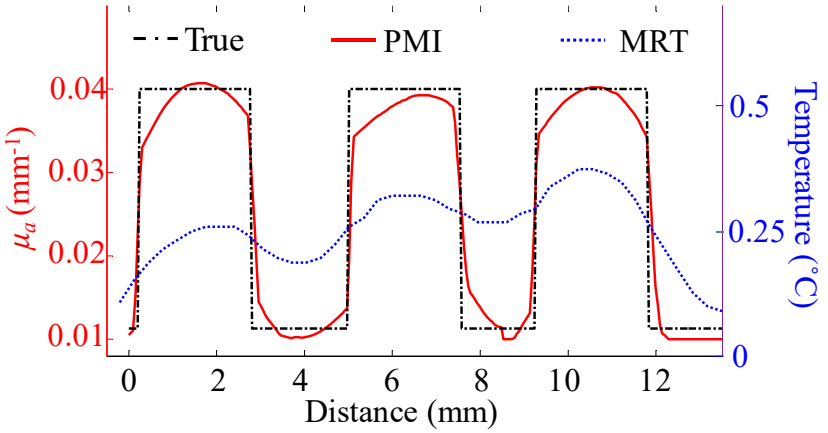

Figure 6.12 Absorption (red) and the temperature (blue) profiles across the three inclusions along the red arrow shown on Figure 6.10. [57]

Table 3 Summary of depth dependence phantom study results. [57]

	Inclusion A		**Inclusion B**		**Inclusion C**	
	True	**PMI**	**True**	**PMI**	**True**	**PMI**
Diameter(mm)	2.5	2.6	2.5	2.4	2.5	2.6
% error Diameter		4%		4%		4%
Mean μ_a (mm^{-1})	0.04	0.039±0.002	0.04	0.037±0.002	0.04	0.038±0.002
***% error* μ_a**		2.5%		7.5%		5.0 %

6.2.5 Phantom study 4: effect of multiple inclusions [94]

The DOT inverse problem results in poor spatial resolution. This makes it extremely difficult to distinguish multiple small objects as separate entities. Often times, the spatial resolution is so

poor that DOT will recover this as a single large object. However, PMI has the potential to overcome this problem due to the fact that the temperature map gives information throughout the phantom and not just on the surface. To study the spatial limitations of PMI, a complex phantom involving nine 2 mm was evaluated.

6.2.5.1 Phantom preparation

A complex phantom with multiples inclusions was prepared. This phantom consisted of a 25 mm cylindrical agarose phantom with nine 2 mm inclusions positioned in a 3 x 3 matrix separated by 1 mm from each other. The absorption and scattering of the background are set to 0.013 mm^{-1} and 0.8 mm^{-1}, respectively by adjusting the Indian ink and intralipid amounts in agar solution. The inclusions are prepared by leaving holes at predetermined positions and filling them with a different agar solution that has two times higher absorption, 0.026 mm^{-1}. Figure 6.13 shows the cross-section of the phantom. The illumination points and the positions of the inclusions within the phantom are indicated by red arrows and dark circles, respectively.

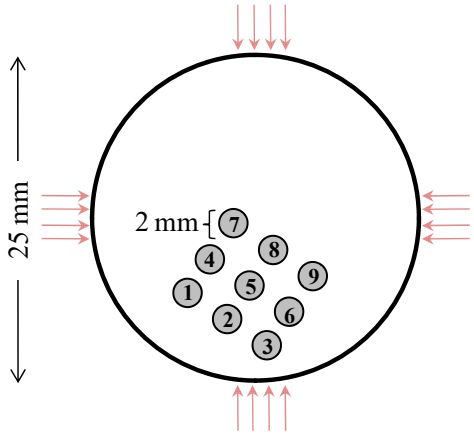

Figure 6.13 shows the 9 2mm inclusions position in the cross-section of the phantom. 4 laser sources are illuminated from top, right, bottom and left respectively as shown.

6.2.5.2 Experimental parameters

The phantom experiment is performed using a gradient echo sequence with a repetition time (TR) and echo time (TE) set to 107 ms and 24 ms, respectively. The field of view (FOV) is set to 60mm x 60mm, the slice –thickness is 5 mm, while the MR image pixel size is 0.234 mm x 0.234 mm. The MRT phase map measured during the heating cycle is acquired at the 2nd time point, between 8th and 16th second, Figure 6.14.b.

6.2.5.3 Results

The more pronounced temperature rise is observed close to the surface under the illumination sites and at the location of inclusions. Although all nine inclusions have the same optical absorption contrast, the temperature increase is different for each inclusion and strongly depends on the distance from the light sources as seen in the MR thermometry temperature map in Figure 6.14.b. The profiles carried out along the lines AB and CD shows the difference in the temperature elevation for some of these inclusions, Figure 6.14.d and 6.14.e. As expected, the temperature goes down as the photons propagate deeper in the tissue but jumps higher at the location of the inclusions due to their high absorption. The elevation in the temperature for each inclusion is different and reduces with the distance from the illumination sites. The dedicated PMI reconstruction algorithm is utilized to generate the high resolution absorption maps using the temperature map as an input, Figure 6.14.c. The FEM mesh used during reconstruction process has 8192 triangular elements connected at 4225 nodes. All nine inclusions are resolved successfully and their absorption value is recovered with high quantitative accuracy as seen on the profiles carried out along the same lines AB and CD, Figure 6.14.d and 6.14.e. First, the size of the inclusions are estimated from the full width at half maximum (FWHM) of these profiles. PMI resolves all nine objects successfully, the estimated diameters from the profiles range

between 1.75 mm to 1.95 mm. The mean error in the recovered size is 9.4% while the max error is 12.5%. In addition to this, PMI recovers the absorption coefficient of the objects with high accuracy. The maximum error in the recovered absorption coefficient is 9.6%, while the error for most of the inclusions is less than 6%, when the peak absorption value in the reconstructed object is considered.

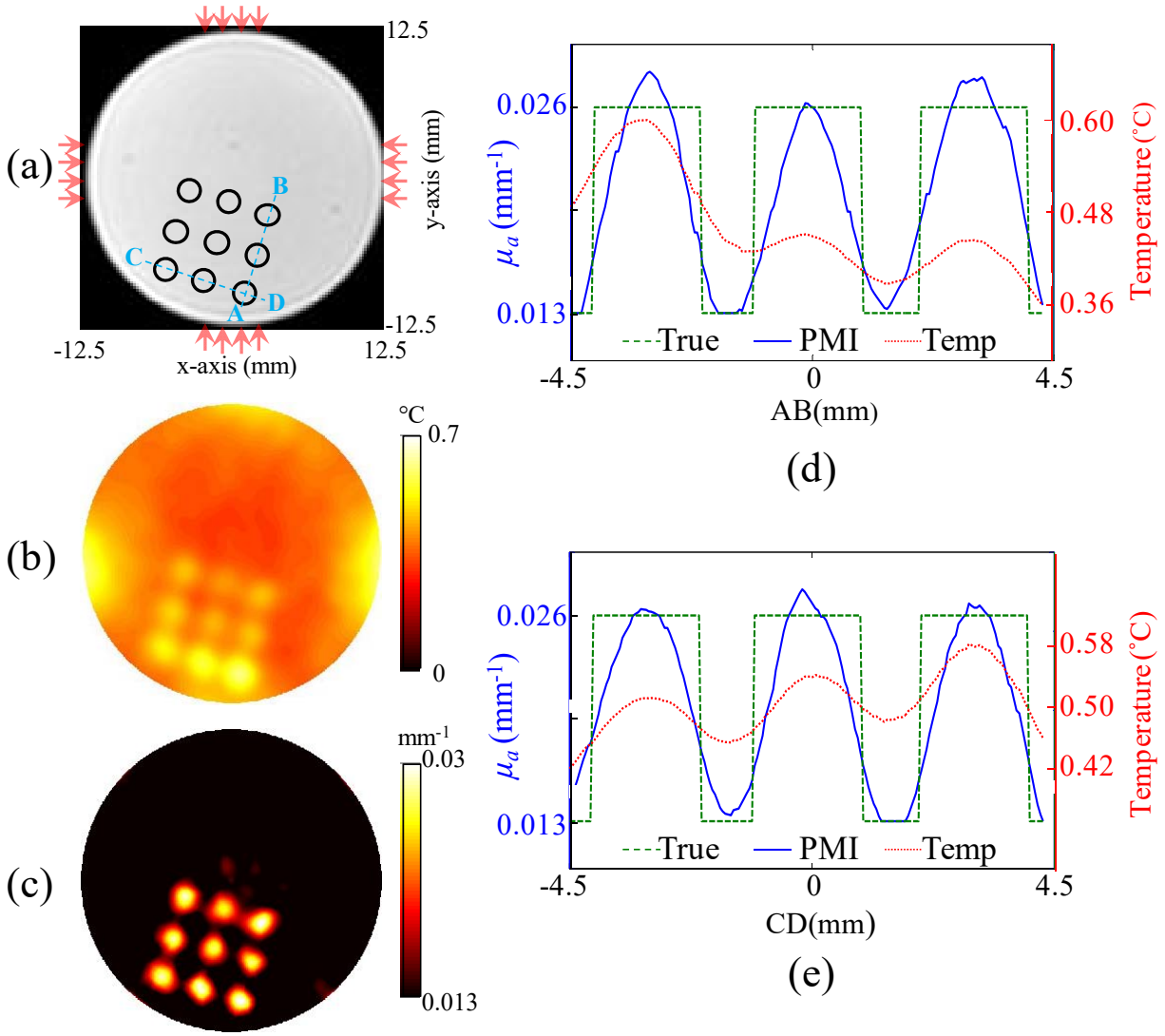

Figure 6.14 (a) shows the inclusions position in the phantom cross-section with laser illumination position with phantom x-y dimension. (b) shows the temperature map acquired with MRT using PMI sequence. All nine inclusions can be seen due to higher temperature change induced by photon absorption. However, the inner inclusions(inclusion 5,6,8) surrounded by outer inclusions have lower temperature change due to photon distribution. (c) shows the PMI

reconstruction. (d) & (e) show the profile of the inclusions reconstructed by the inverse solver comparing to the temperature profile. [94]

Table 4 Summary of multiple inclusion phantom study.

	x-axis FWHM (mm)			y-axis FWHM (mm)			Mean Absorption coefficient (mm^{-1})		
Inclusion	**True**	**PMI**	**% error**	**True**	**PMI**	**% error**	**True**	**PMI**	**% error**
1	2	1.95	2.5%	2	1.88	6%	0.0260	0.0230	11.54%
2	2	1.84	8.0%	2	2.04	2%	0.0260	0.0233	10.38%
3	2	1.84	8.0%	2	1.75	12.5%	0.0260	0.0239	8.08%
4	2	1.78	11.0%	2	1.81	9.5%	0.0260	0.0222	14.61%
5	2	1.75	12.5%	2	1.93	3.5%	0.0260	0.0215	17.30%
6	2	1.77	11.5%	2	1.65	17.5%	0.0260	0.0215	17.30%
7	2	1.81	9.5%	2	2.10	5%	0.0260	0.0232	10.77%
8	2	1.75	12.5%	2	2.06	3%	0.0260	0.0211	18.85%
9	2	1.81	9.5%	2	2.00	0%	0.0260	0.0227	12.69%
Average		**1.81**	**9.4%**		**1.91**	**4.3%**		**0.0225**	**13.50%**

6.2.6 Phantom study 5: monitoring gold nanoparticle [95]

Previously, dye was used to change the absorption of the phantom and inclusion. However, this dye cannot be used for *in vivo* animal or human imaging. However, contrast absorption molecular probes such as gold nanorods can be used to elevate the optical absorption of the tissue and hence enhance the photo-thermal effect. Gold nanorods are an important part of molecular medicine as describe in section 4.2 [85, 86]. Consequently, PMI has the potential to play a major role in molecular medicine by providing information about the location and concentration of a distribution of gold nanorods. In this study, we evaluate whether PMI can

monitor the distribution of gold nanorods quantitatively at MR resolution. PMI takes advantage of the high sensitivity of MRT to measure the internal temperature changes caused by the photo-thermal effect. Afterwards, PMI converts the high resolution MRT maps into tissue optical absorption maps. As the optical absorption coefficient is directly proportional to the concentration of gold nanorods, this technique shows much promise in monitoring the gold nanoparticles.

6.2.6.1 Phantom preparation [95]

Figure 6.15 shows a T1 weighted anatomical MR image of a 25 mm diameter phantom. The phantom absorption coefficient is set to 0.01 mm^{-1} and its reduced scattering coefficient is set to 0.8mm^{-1}. Three 3 mm diameter inclusions are embedded at different depths (3 mm, 7.5 mm, and 12 mm) from the surface of the phantom to the center of each inclusion as seen in Figure 6.15. Gold nanorods are used to induce an absorption contrast almost twice the amount of the background contrast at 0.026 mm^{-1}.

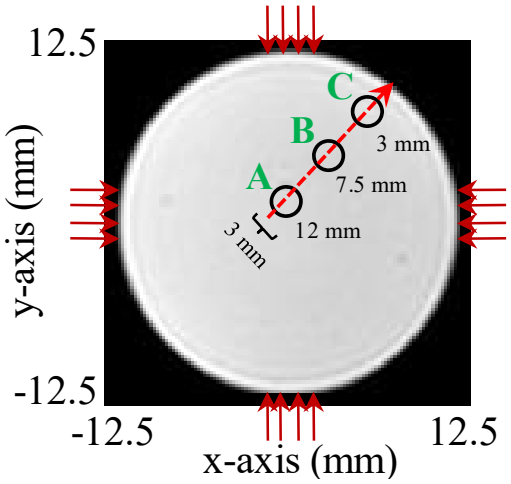

Figure 6.15 (a) T1weighted image of the 25 mm diameter agar phantom with three inclusions (3 mm diameter) containing identical concentrations of gold nanorods are embedded in a linear line at different depths from the phantom surface at: 3, 7.5, 12 mm from the center of the inclusion. Their optical absorption coefficient is set to 0.026 mm^{-1}. The four laser positions are shown by the red arrows. [95]

6.2.6.2 Experimental parameters

This phantom study was performed using the same parameters and procedures as described in section 6.2.2.2.

6.2.6.3 Results

The MRT temperature map after 24 seconds of illumination is shown in Figure 6.16.a. Although all three inclusions have the same optical absorption, their temperature change, induced by photo-thermal effect, are different. This is due to their different distances from the four laser light sources. The temperature change within the medium is proportional to the density of photons. In fact, the highest increase in temperature is observed near the laser illumination sites. However, the FEM reconstruction algorithm accurately compensates for the depth dependence of the temperature map as seen in the high resolution PMI reconstructed absorption map, Figure 6.16.b, and is in good agreement with the true absorption map in Figure 6.16.c.

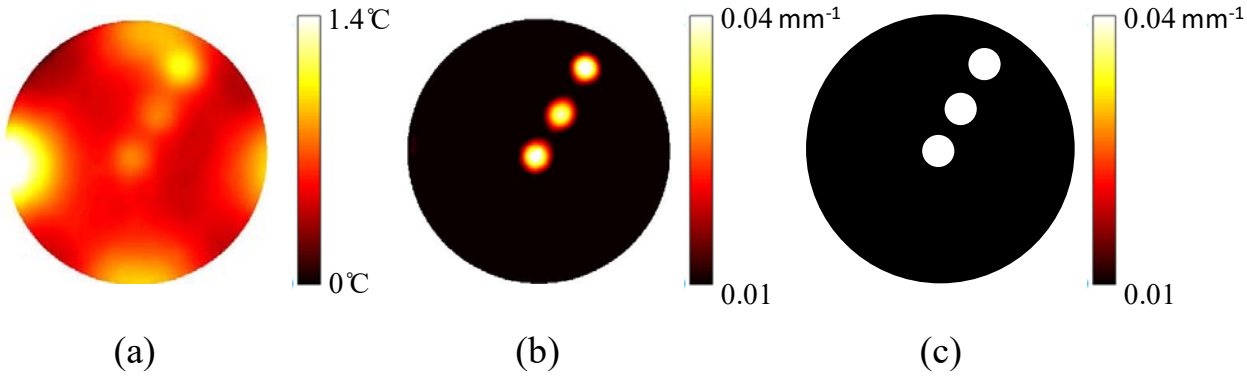

Figure 6.16 (a) MRT temperature map measured of the agar phantom. (b) FEM based PMI reconstructed absorption map. (c) True reconstructed absorption map. [95]

The temperature and the reconstructed absorption profiles along the red dotted line in Figure 6.15 are plotted in Figure 6.17 and summarized in Table 5. Although the depth dependence can be seen in the temperature profiles, the FEM reconstruction algorithm

compensates for this as seen in the blue profiles in Figure 6.17. The size of the recovered inclusions is underestimated (~0.75x) at all depths corresponding to a 23% error. Since the high absorbance region is confined to a smaller area than the true size, the resulting optical absorption recovered from the reconstruction algorithm provides a higher absorption to compensate as seen by the blue PMI profile. However, when the mean optical absorption value is considered, PMI is in very good agreement with the true absorption value with less than 7% error for all three depths. In addition, the profiles show that the position of the inclusions recovered from the temperature map alone and PMI are aligned with the true position.

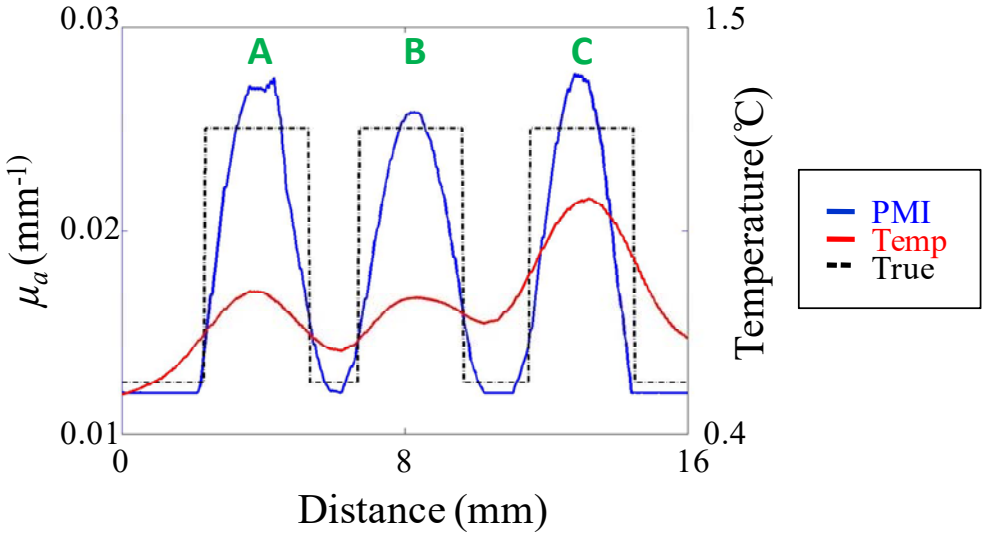

Figure 6.17 Profiles of the temperature and reconstructed absorption across the inclusions along the red arrow in Figure 6.15. [95]

Table 5 Summary of contrast agent enhancement phantom study.

	Inclusion A		Inclusion B		Inclusion C	
	True	**PMI**	**True**	**PMI**	**True**	**PMI**
Diameter(mm)	3.0	2.3	3.0	2.4	3.0	2.3
% error Diameter		23%		20%		23%

Mean μ_a (mm^{-1})	0.04	0.0254	0.04	0.0244	0.04	0.0263
***% error* μ_a**		2.31%		6.10%		1.15%

These results show that the optical absorption enhanced by gold nanorods in a highly scattering medium is well recovered. Hence, the distribution of the gold nanoparticles can be accurately monitored by PMI.

6.3 In vivo studies

These studies will be similar to the phantom studies but will provide a more realistic background tissue distribution and background absorbance. These studies are following the approach developed by Graves et al [96]. A translucent plastic tube will be filled with various concentrations of NIR dyes. This tube will be called the "inclusion". Tube with inner diameters 5 mm will be employed. The tube will be positioned in different location inside the small animal body to verify high resolution property of PMI in all positions. Imaging studies will be conducted immediately after surgery while the animals are still under anesthesia.

6.3.1 Optimization of PMI sequence parameters for *in vivo* imaging

In this first optimization preliminary study, there are many complications that arise from moving from a simple agarose phantom to live animal. Animal imaging is very challenging and for the *in vivo* study, there is a balance between increasing the SNR while simultaneously increasing the MR sequence echo time to maximize the phase change per degree temperature change from the gradient echo sequence. In the phantom experiments a short T_R and long T_E

gradient echo sequence was used to increase the SNR and achieve the best results. The phase change is linearly proportional to the echo time. [MR Thermometry]

$$\Delta\phi = \Delta T * \gamma\alpha B_0 * T_E$$

However, when using live animals there is a scan time limit due to the anesthesia. The signal loss resulting from a long echo time is amplified by the shorter T2* of the animal tissue. This decay in the MR signal intensity is exponential:

$$I_{MRI} \propto \exp(-\frac{T_E}{T_2^*}) \tag{31}$$

This means the MR thermometry signal intensity will be:

$$SNR_{phase} \propto T_E \exp(-\frac{T_E}{T_2^*}) \tag{32}$$

In short, optimizing SNR means using a short TE but optimizing the phase change requires a long TE. As these are mutually exclusive, choosing specific echo time for the *in vivo* study is critical in photo-magnetic imaging. From the figure below, it can be seen that if T_E is equal to T2*, MRT will has highest signal.

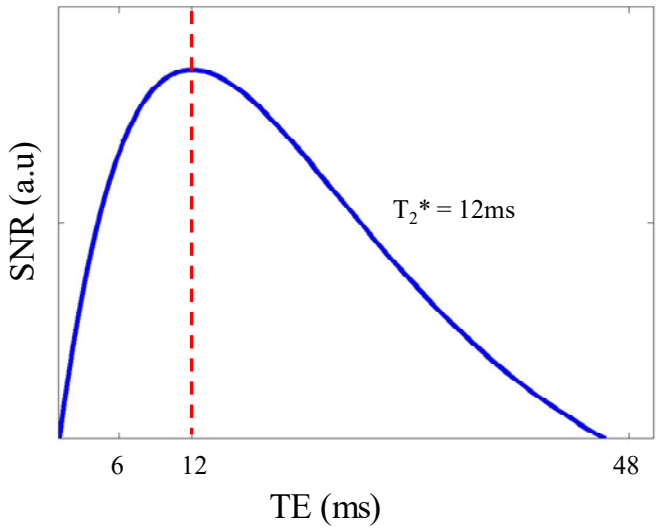

Figure 6.18 simulated SNR of the MRT vs. T_E at T_2*=12 milli-seconds.

Another challenge that arises from live animal imaging is the motion artifact. In the following experiment, we focus the region of interest at the lower body of the mice to reduce the respiratory movement from the upper body. In addition, the respiratory triggering system can further reduce the motion artifact.

6.3.2 Optimization of mesh for animal geometry

Previously a cylindrical agar phantom was used replicate a rat body. However, in reality, a rat body is much more complicated and not perfectly circular and symmetric, as seen in Figure 6.19. Therefore in order to perform PMI *in vivo*, we need to model the irregular shape boundary of the subject. This will allow us to better estimate the photon distribution and temperature of the subject. The process to generate the finite element mesh from the high resolution MR image is defined:

[1]. Definition of the origin coordinates. The origin coordinate is defined by two agarose gel marker which is placed on the laser probe at $\theta = 0^{\circ}$ and 90° to define the x and y position of the center origin point.

[2]. Definition of boundary. A binary mask is used to define the exterior boundary. The binary mask threshold is set by the user on a case by case basis according to the image sequence and magnitude. The program will automatically generate the FEM mesh according to the boundary and inner mesh fineness set by the user.

[3]. Definition of laser center. The center of the laser illumination pattern is defined according to the marker position. The laser pattern is defined by the collimator spot size. The

fineness of the boundary and the laser pattern will pick up the corresponding FEM nodes on the boundary as the laser source points in the photon diffusion equation.

[4]. Generation of the differential map for the mesh in advance for adjoint Jacobian reconstruction.

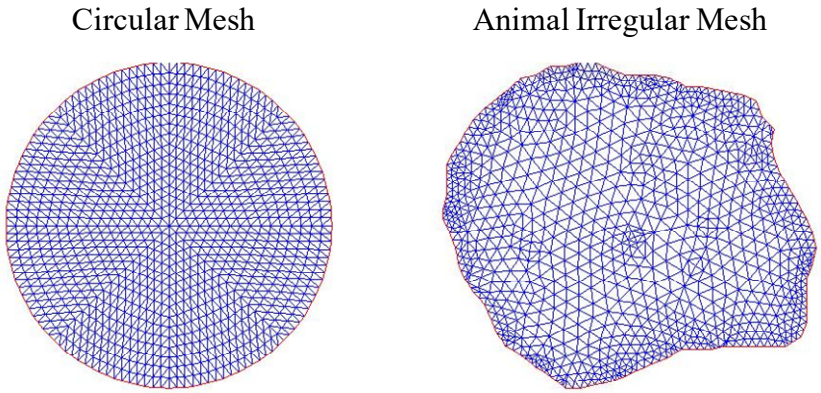

Figure 6.19 Comparison of symmetric mesh for (a) agar phantom versus (b) irregular animal mesh.

6.3.3 Animal preparation

All animal procedures were approved by the Institutional Animal Care and Use Committee at University of California, Irvine. Five to six weeks old Fisher rats with 180g average weight were used in this study. Prior to imaging, the animal is shaven to remove hair around the imaging area. Ketamine (87 mg per kg) was use to anesthetize the rats for a 50 minute period.

For each imaging session, prior to any animal imaging, an agarose phantom is used to calibrate the laser power and check the laser power for animal safety. During the imaging, the laser power is kept under ANSI limit based on maximum skin exposure limit suggested by ANSI

to prevent any skin tissue damage or uncomfortable. After the experiment, the animal is placed on the electronic heating pad to conserve its body temperature and prevent hyperthermia complication during recovery.

6.3.4 Experiment procedure

Prior to the animal imaging, a 25 mm diameter homogenous agarose gel cylindrical phantom is first used to calibrate the laser power. Then the anesthetize animal is positioned at the center of the animal integrated PMI coil. Two agarose markers are placed on two perpendicular optical probes for alignment of the PMI laser illumination plane with MR slice. After the routine survey localizer imaging, a high resolution T1 weighted image is taken. Next, PMI is performed using a photo-magnetic imaging sequence with TR 100 ms, TE 12 ms, and bandwidth 1.2 pixels. The laser is turn on for 64 seconds in this experiment. A gradient echo image sequence was taken at 64 seconds to obtain the MR thermometry data. The total imaging time is 20 minutes. The subject is under anesthesia for a maximum of 50 minutes. The timeline of the animal experimental procedure is described in Figure 6.20.

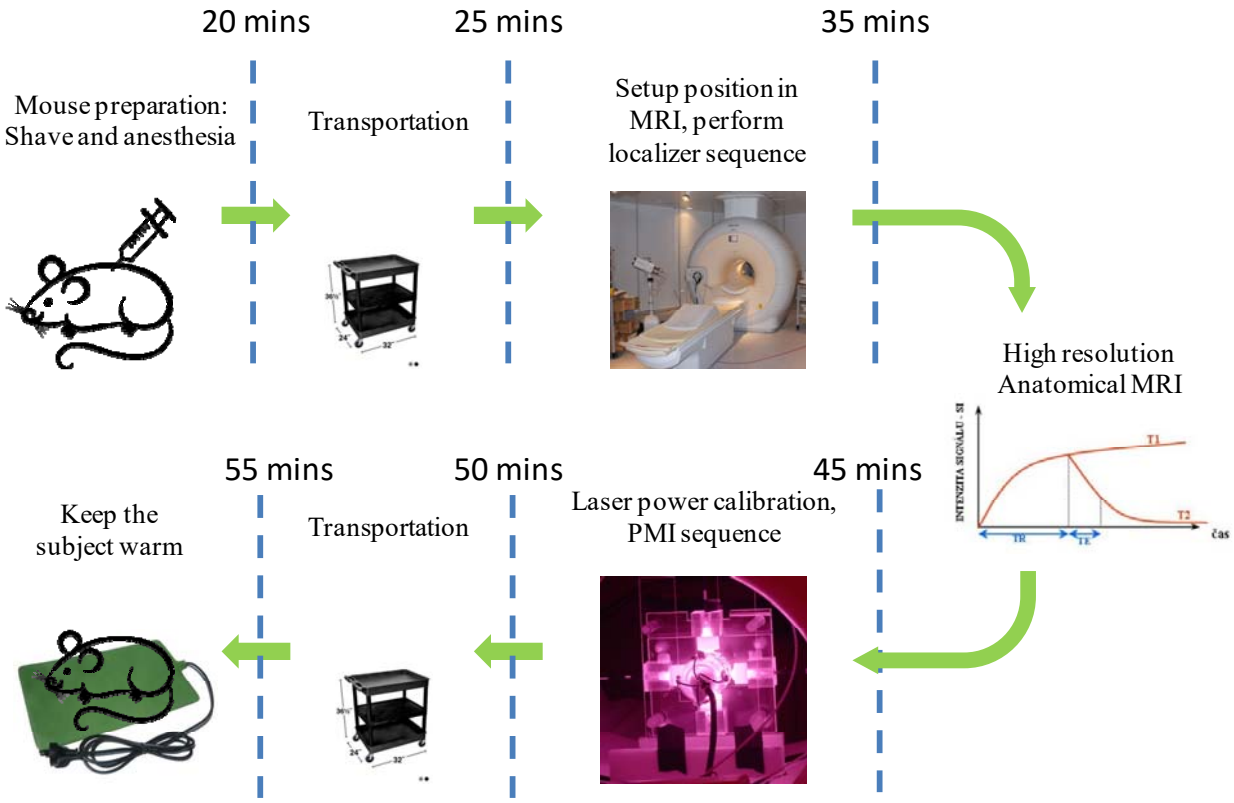

Figure 6.20 Timeline of animal experiment. The maximum animal anesthesia time is less than 60 minutes.

6.3.5 Feasibility studies

In this *in vivo* animal study, we determined whether PMI can is feasible in a live rat. A major consideration with *in vivo* imaging is the safety of the animals. As reported in the Chapter 6.2.1, the accuracy of PMI depends on the SNR. In this study, we evaluated whether the maximum laser power set by ANSI limits is capable of generating a temperature increase above the MRT noise level. Two different cases were studied: subcutaneous inclusion, and a deep seated inclusion in the center of the rat. This *in vivo* study proved that laser power set by ANSI is sufficient of generating a large enough temperature increase in the rat for PMI.

6.3.5.1 Case 1: subcutaneous inclusion

First we wanted to see whether PMI has the sensitivity to detect small regions of high absorption such as the aorta or a tumor which have a high blood volume and correspondingly high absorption. Again we started with the simpler case of a subcutaneous inclusion as the MRT signal is strongest closest to the laser source.

In this section, a thin walled transparent 3 mm diameter and 100 mm long tube was surgically inserted just beneath the skin of the rat 3.7 mm deep. This subcutaneous inclusion was filled with a high absorption contrast solution (μa=0.04 mm-1). The inclusion also contained the MR contrast agent gadolinium (Gd-DTPA, 0.02%) in order to enhance the contrast in the T1 anatomical MR image in order to locate the inclusion with high precision. This procedure was done under anesthesia by the animal technician.

A single 808 nm, 500 mW laser was used to illuminate the rat from the top as seen in Figure 6.21. This source position was chosen due to the proximity to the inclusion. The results show that the inclusion can be located from the MRT temperature map without any reconstruction, Figure 6.21.b. As expected the temperature decrease the further from the laser source but shows a high signal (~0.5°C) at the location of the inclusion due to its high optical absorption. However, there is a significant artifact next to the inclusion. This is mostly likely a attributed to air that gets trapped in the animal when the inclusion is surgically embedded. From part a, the inclusion can be clear seen in the T1 anatomical MR image due to the Gd-DTPA MR contrast agent. However, while inserting the inclusion into the animal, inevitably, air will get trapped in the space around the inclusion. The magnetic susceptibility difference between the small air gap, biological tissue, and the inclusion will result in signal artifacts and geometry distortion. For the T1 weighted anatomical image this is not severe as the MR spin echo

sequence and gradient echo sequence uses a short TE. However, PMI is strongly affected due to the long TE gradient echo sequence (15 ms) used to maximize the phase change for MR thermometry. However, as this is a result of the inclusion surgery, this will not affect animals that have naturally growing tumors or high absorption areas.

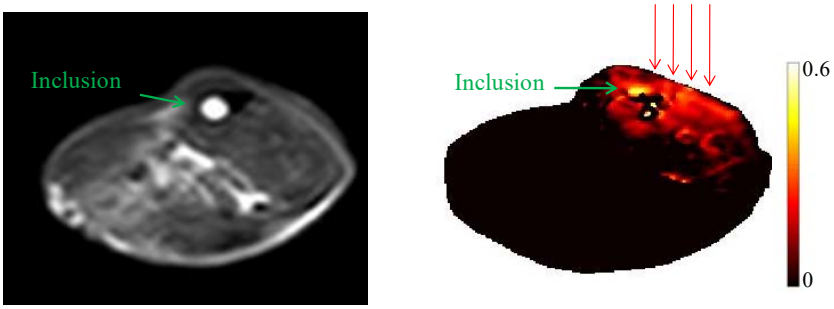

(a) (b)

Figure 6.21 (a) shows the high absorption inclusion positioned at the top of animal. The depth of the inclusion to the boundary is 3.7mm. (b) shows the temperature map acquired with MRT with PMI sequence.

6.3.5.2 Case2: deep inclusion

Finally we looked at the most challenging case, a deep seated inclusion located at the center of the rat farthest for the laser sources. The inclusion was surgically embedded 12 mm deep at the center of the rat. This deep seated inclusion is identical to the one used in the previous subcutaneous case. Due to the location of the inclusion, two lasers were used to heat the tissue as seen in Figure 6.22.b. As expected, the temperature map shows an increase in temperature at two sides of the rat where the laser sources are located, as seen in Figure 6.22.b. However, the high signal in the center of the phantom clearly identifies the high absorption 3 mm inclusion even in deep tissue. Similar to the previous case, due to the surgical insertion of the inclusion, there is an air gap surrounding the inclusion in the MR image, Figure 6.22.a. While

PMI is affected, as seen by the artifacts near the inclusion, the results show that PMI can accurately locate the inclusion even when placed 12 mm deep.

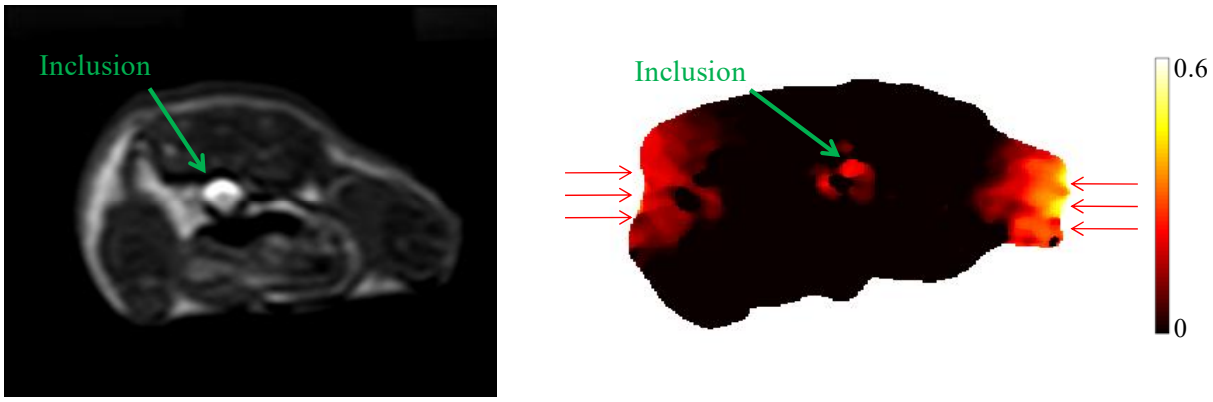

(a) (b)

Figure 6.22 (a) is the T1 weighted MRI to show the position of the inclusion. (b) shows the temperature map acquired with MRT using PMI sequence.

Chapter 7: Clinical human breast PMI interface

PMI has great potential for a number of clinical applications. Since we validated that PMI works *in vivo* for small animals, our next step is to translate this technology and method to clinical applications. In particular, PMI could have a big impact on breast cancer. In this chapter, we report on the development of a human breast PMI system. Although the human body shares many similarities to small animals, translating the small animal system to humans is a major step and requires thorough testing to optimize the system for humans to ensure accuracy and safety. In this chapter we will report on the development of this human breast PMI system from phantom experiments to *ex vivo* biological tissue.

7.1 Phantom studies

The human breast has a different size, shape, and optical properties than rats. Therefore a dedicated phantom study was complete to test the performance of the PMI breast coil and optimize the system. As the human breast is much larger than a rat, one of the key issues in developing this human breast system was to first determine whether the photons from the laser would be able to penetrate deep enough to make PMI feasible. These results were reported in the first phantom study. After this feasibility study was complete, we developed a human breast PMI prototype and tested the performance to see whether our PMI system can distinguish multiple inclusions located deep in the medium.

7.1.1 Validation of PMI modeling for breast interface

A small preliminary study was first performed to determine whether PMI was feasible in a human breast sized phantom and evaluate the human breast PMI system. To verify the breast PMI system, the accuracy of the FEM forward algorithm to model the temperature change induced by the laser in homogeneous and heterogeneous optical absorbing mediums was studied.

7.1.1.1 Sample Preparation

For this feasibility study, a large cylindrical agarose gel phantom, 60 mm in diameter and 70 mm in length, was prepared. A 5 mm diameter inclusion was embedded just under the surface of the phantom, 5 mm deep. The inclusions absorption coefficients are $0.01mm^{-1}$ (homogeneous), $0.02mm^{-1}$ and $0.06mm^{-1}$.

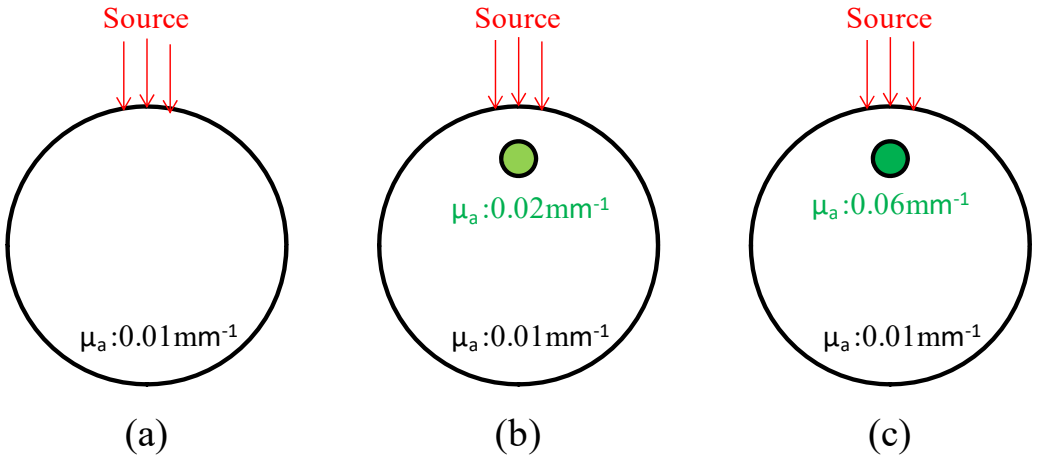

Figure 7.1 (a), (b) and (c) are the cross-sections of three cylindrical agarose phantoms with three different absorption coefficient inclusions. (a) has the inclusion with same absorptions as the background and the second one has 2 times and the third one has 6 times absorption. The laser illumination position is pointed out by the red arrows.

7.1.1.2 Results

Figure 7.2 compares the experimental results from PMI to FEM. The results are highly promising as the PMI temperature maps show that MRT can capture laser induced temperature

change for all three different phantoms. As expected, the results show that the temperature increase is dependent on the optical absorption of the medium. This can be observed in the absorption maps and profiles in Figure 7.2. The homogeneous phantom which has the lowest optical absorption exhibits the smallest temperature change while increasing the absorbance results in a larger temperature gain. The PMI experimental results are in very good agreement with FEM as seen in the profiles from part c. This experiment demonstrates the accuracy of the FEM forward algorithm to model the temperature change induced by the laser in homogeneous and heterogeneous optical absorbing mediums.

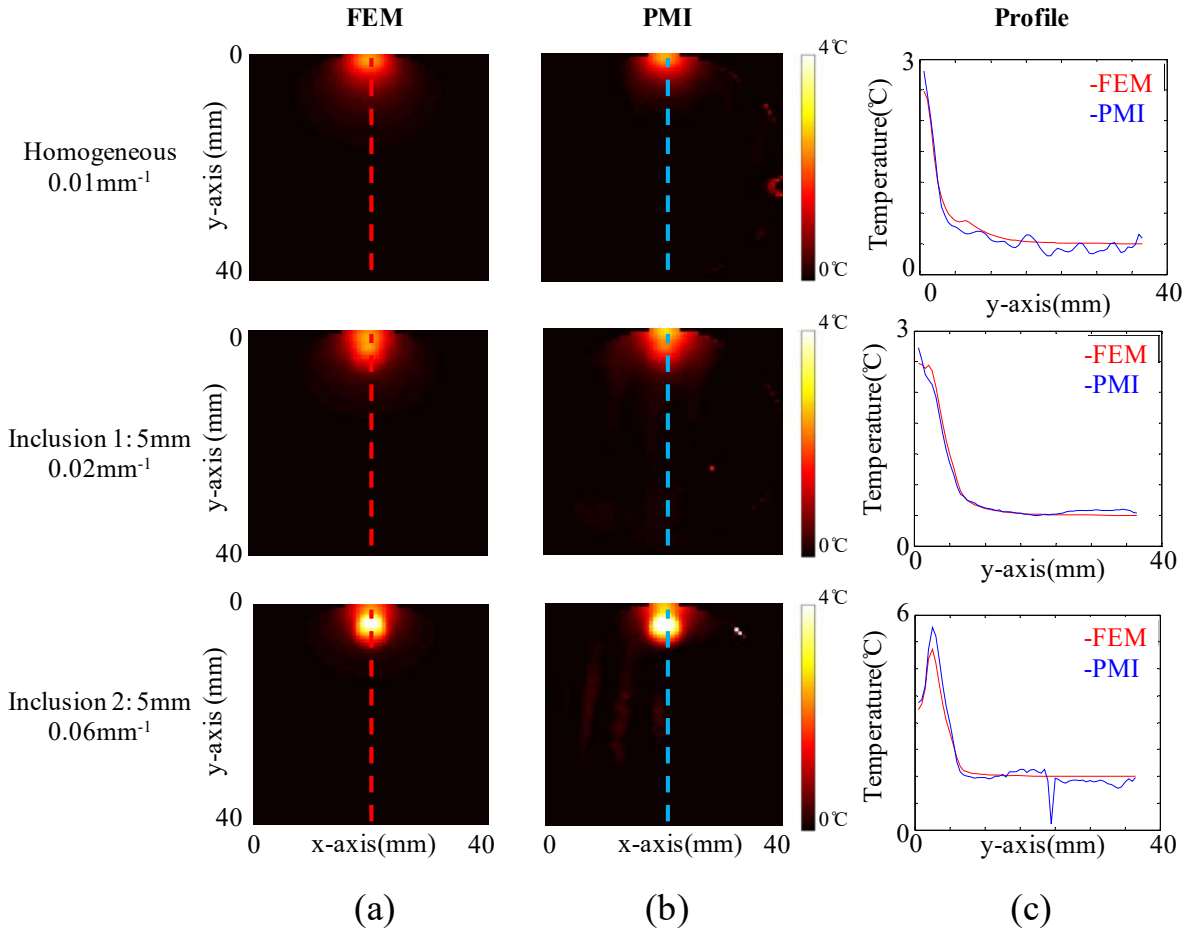

Figure 7.23 (a) shows the temperature map estimated by FEM based PMI forward solver to compared with the real temperature map obtained by MRT in (b). (c) presents the profiles of these three phantoms at the lines drew in (a)&(b).

7.1.2 Experimental results

Although the previous study showed the feasibility of PMI in normal uncompressed breast sized phantoms, breast compression was chosen to maximize the photon density throughout the medium to maximize the SNR and improve the accuracy of PMI. Breast compression is common in many imaging methods such as mammography. Due to the poor photon depth and high scattering in biological tissue, diffuse optical imaging is most challenging when the inclusions are located far from the laser source and close together. In this study, in order to test the limits of PMI, we tested the most challenging case: whether PMI could recover two 5 mm diameter inclusions located at the center of the phantom farthest from the source with our PMI breast coil described in chapter 5.

7.1.2.1 Phantom preparation

A rectangular phantom (4cm x 4cm x 6cm) was prepared to simulate the size and optical properties of a breast compressed to 4 cm. Two 5 mm diameter inclusions located 5 mm apart (edge to edge) were positioned in the middle of the phantom, farthest from the edges as seen in Figure 7.3. The absorption and reduced scattering coefficients of the phantom were set to 0.005 mm−1 and 1 mm−1, respectively to mimic the optical properties of breast tissue. The absorption contrasts in the two inclusions were identical at 0.02 mm-1, four times the absorption contrast of the background.

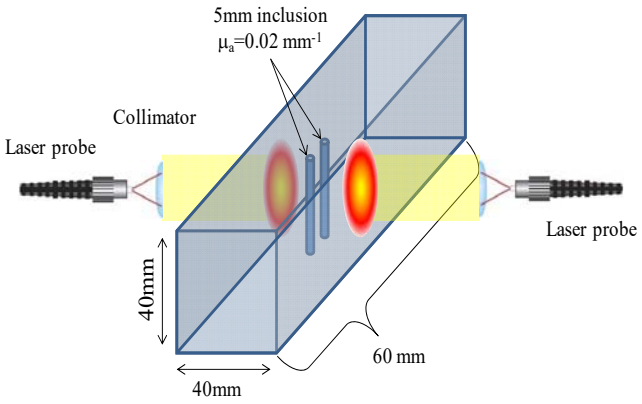

Figure 7.3 shows the phantom dimensions and inclusions and experiment setting in this experiment. Large lens collimating system is used here to provide homogenous illumination to the compressed breast phantom. The spot size of the laser illumination is 15mm diameter.

7.1.2.2 Experimental parameters

The power density used was the limit set by ANSI, namely 0.31W/cm2 for duration of more than 10 seconds. The phantom was illuminated from both sides with the spot size of 1.5 cm diameter for duration of 32 seconds. Four frames of temperature map were acquired with an 8-second temporal resolution during the heating cycle. During the reconstruction, images from all four time points were used, i.e. reconstruction algorithm used the time-evolution of the temperature distribution. A gradient echo sequence of 55 ms repetition time (T_R) and 36 ms echo time (T_E). This large TE sequence results in a larger phase change per temperature increase. The slice thickness of this MRI sequence is 3mm and the flip angle is 90 degree.

7.1.2.3 Results

As seen from the Figure 7.4, the two 5 mm inclusions were successfully recovered although they are located at the center of the phantom, 2 cm deep from both surfaces, which represents the worst case. There were some artifacts existed at the boundaries, though. The artifacts on the left and right side were due to lack of illumination on that side. Illuminating the

object from all sides should solve this problem. The artifacts under the illumination points, on the other hand, are due to mismatch between the modeling and experimental data, presumably due to our current 2D modeling capability. By optimizing the algorithms and expanding into 3D, these artifacts should be eliminated as well. The FWHM of the recover inclusion is 5.2mm and 5.1mm which are 4% and 2% error similar to the animal phantom results in chapter 6.

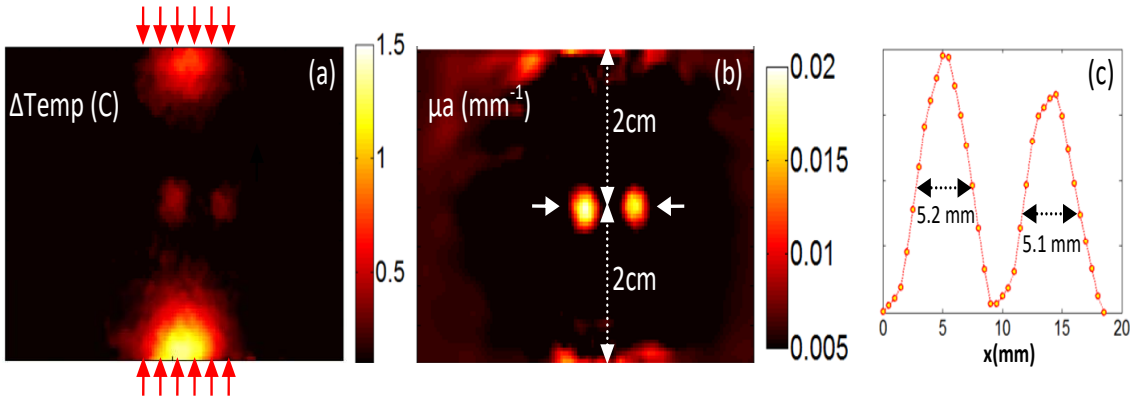

Figure 7.4 (a) The temperature difference map for the third frame (16-24 seconds). The red arrows indicate the illumination points. The bottom probe delivers 30% more light than the top one and still under ANSI limit. (b) The reconstructed absorption map using four temperature frames acquired in 32 seconds (8 seconds each). The two 5 mm objects positioned 2 cm below both surface are successfully recovered with 5% and 15% error based on the peak value, respectively. (c) The profile shows that FWHM of the recovered objects are very close to their real size ~5 mm.

7.2 Evaluation of breast PMI [94]

PMI is a multimodality imaging technique that relies on both the optical and thermal properties of the medium. Although the agar phantoms that were used tried to simulate their properties, unfortunately, they are not a perfect substitution for biological tissue. Thus, the potential of PMI for future human breast studies is dependent on whether PMI is feasible in biological tissue. Chicken breast was chosen as it is a common substitute for human breast tissue for its similar optical and thermal properties [97]. As mentioned in the phantom section, unlike

small animal imaging whose small size allows for easy delivery of the photons throughout the tissue, a key issue is whether photons can penetrate through the larger chicken breast size sample. In this section, we address this question and evaluate the PMI breast system with biological tissue. The *ex vivo* PMI results presented in this section represent the first step in translation this novel technology to the clinical area.

7.2.1 ANSI Limit

An important consideration for this human breast PMI system is safety. Due to the high absorption and scattering of photons in biological tissue, PMI is more challenging on larger phantoms due to the poor penetration depth. Under other circumstances, increasing the power of the laser would address this issue. However, as this system is designed for human imaging, it must fall under the ANSI limits. Therefore it is the key to understand whether PMI is feasible under these power density limitations.

7.2.1.1 Chicken breast preparation

In this study chicken breast is used to replicate human breast tissue. The chicken breast was cut into a 4 cm x 6 cm x 5 cm slab, Figure 7.5. This slab was immersed in room temperature deionized (DI) water to provide a similar magnetic susceptibility environment and reduce the MRI gradient echo artifact at the boundary of the tissue without affecting the PMI measurements. DI water is not highly absorbent at the laser wavelength (808 nm) and thus has little effecting on the PMI measurements.

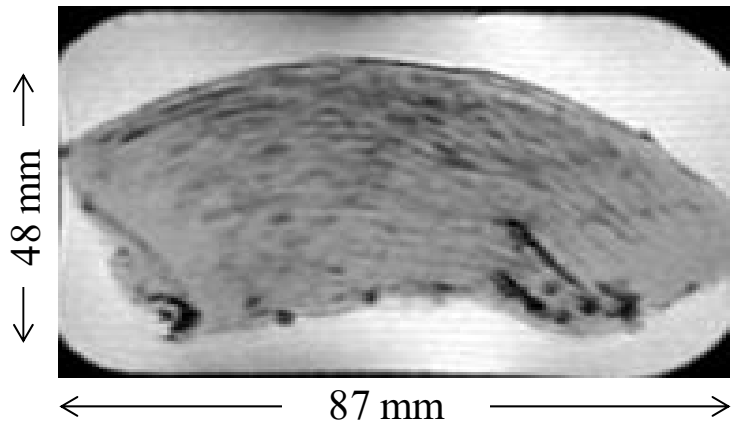

Figure 7.5 shows the dimension of the chicken breast cross section with MRI T1 gradient echo sequence.

7.2.1.2 Experimental procedure

In this experiment, the chicken breast sample is illuminated from two sides of the chicken breast, as seen in Figure 7.7.b. The power of the two laser source is under ANSI limits and set at 300 mW/cm2. The experimental procedure for this study starts with a high resolution anatomical MRI T1weighted image. The laser position in the axial direction is precisely located by the T1 weighted image using a fiducial marker. Next, the PMI measurements are taken. Figure 7.6 shows the dynamic MR temperature acquisition timeline consisting of multiple frames with a temporal resolution of 8 seconds. First, the baseline MR phase map is acquired before the laser is turned on. In this step, the dynamic MR temperature sequence acquisition is initiated using a gradient echo sequence with repetition time TR at 55 ms and echo time TE at 24 ms, FOV = 120 mm*120 mm, MR image pixel size is 0.468 mm*0.468 mm, and a 3 mm slice-thickness to acquire the first MR phase map. Secondly, the laser is turned on at the beginning of the second frame to warm up the medium under investigation and dynamic MR temperature measurements are acquired for the following frames. The dynamic MRT temperature map is acquired for a total of 64 seconds (8 frames). The laser induced temperature variation based on the phase shift between any frame and the baseline is calculated during the post processing step.

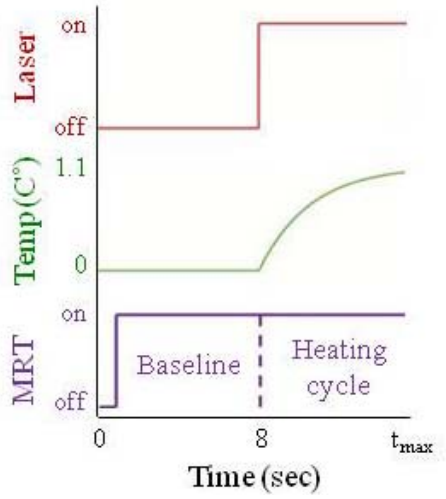

Figure 7.6 PMI data acquisition timeline: the temporal resolution of the dynamic MRT sequence is 8 seconds. The laser is turned on after the acquisition of the first MRT baseline image, and several images are acquired during this heating-phase as the temperature of the medium rises.

7.2.1.3 Feasibility results

Figure 7.7.a and b shows the temperature map before and after laser illumination. The MRT temperature map shows that the lasers have enough power to heat the chicken breast using only two laser positions to generate a temperature increase above noise level (0.1°C). A temperature gradient can be seen with the highest increase near the boundaries closest to the laser sources and decreases with distance. These results show that breast PMI is feasible in biological tissue and can be safely performed using a laser power under the limit set by ANSI.

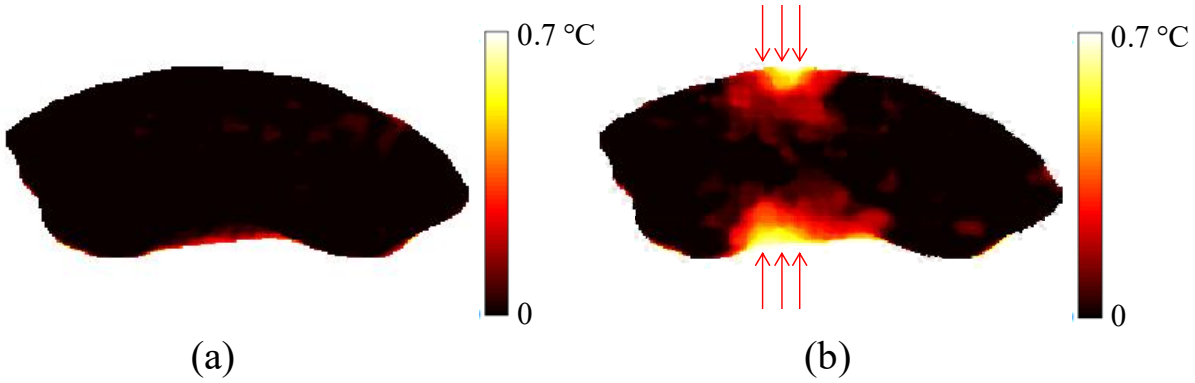

Figure 7.7 (a) 4 cm x 6 cm x 5 cm chicken breast slab immersed in DI water bath. (b)High resolution MR image. (c) Temperature map of the chicken breast without laser illumination used as a baseline temperature map. (d) Temperature map of the chicken breast after 40 seconds laser illumination from top and bottom shows absorption of laser photons and temperature increase.

7.2.2 *Ex vivo* experimental results

PMI has much potential to impact breast cancer in clinical medicine as a low-cost add on to any MRI system by providing high spatial resolution functional information about breast tissue and tumors. For example, it is well established in optical imaging that the endogenous contrast of diseased tissue can be up to three times higher than normal tissue, however the poor spatial resolution of diffuse optical imaging techniques makes clinical application impractical [98, 99]. PMI has the potential to change the field of optical imaging and clinical medicine by providing functional information with the spatial resolution on the same order of magnitude as MRI. In this study, we evaluated the performance of the breast PMI system to recover the size, position, and optical absorption of a small inclusion in biological tissue with high spatial resolution and quantitative accuracy. Chicken breast was used to mimic the breast tissue as it resembles the optical and mechanical properties of human breast tissue. A 3.5 mm agarose inclusion whose optical contrast was four times higher than the chicken breast slab was used to mimic a breast tumor. The results of the chicken breast study reported in this section verify the performance of PMI and the hybrid breast PMI system in *ex vivo* biological tissue.

7.2.2.1 Sample preparation

The chicken breast phantom consists in an 82 mm (x) x 30 mm (y) x 45 mm (z). A 3.5 mm hole is drilled along the z axis 13 mm deep as seen in Figure 7.8.a. This hole was filled with an agarose mixture almost four times higher contrast than the chicken breast slab. The absorption and scattering of this mixture are respectively set to 0.041 mm-1 and 0.8 mm-1. This inclusion also contains 0.04% gadolinium, a MRI contrast agent, to enhance the contrast of the inclusion in the T1-weighted MR image, Figure 7.8.a. Although the drilled hole is in a circular shape, an elliptical cross-section is observed in the MR image. Most likely, the distortion of the shape of the hole can be attributed to the elasticity of the chicken breast tissue when moved to the breast PMI system sample holder. The chicken breast is illuminated from 2 sides as seen by the red arrows in Figure 7.8.a.

7.2.2.2 Experimental procedure

The experimental procedure and parameters for this chicken breast study are the detailed in the previous section 7.2.1.3. However, in this study, the baseline phase map was subtracted from the fourth frame which occurs 32 seconds after the start of the heating for the dynamic PMI temperature acquisition to generate the temperature difference map seen in Figure 7.8.b. This resulting temperature map is utilized during the PMI image reconstruction as measurements to obtain a high resolution optical absorption map. In fact, each pixel of this image is utilized as temperature detector in the reconstruction algorithm.

The FEM mesh is constructed using the boundary of the sample delineated using the MR image and consisted in 4908 triangular elements connected at 2564 nodes. Prior to performing PMI reconstruction, the bulk background absorption coefficient for the chicken breast tissue sample is calculated from the MRT temperature measurements. For this purpose, the temperature

distribution is utilized down to one centimeter depth on both illumination sites to eliminate the effect of the inclusion presence. Both optical absorption and scattering parameters are considered constant throughout this limited volume in this initiation step. Scattering parameter is set to the 0.2 mm-1 based on the values reported in the literature [97]. After that a minimization algorithm is utilized to minimize the difference between estimated and measured temperature distribution, and find a bulk absorption value for the tissue sample. This value is then used as the initial estimate for the PMI reconstruction algorithm.

7.2.2.3 Results

Figure 7.8.b shows the temperature map from MRI thermometry overlaid on the MRI anatomical image. The profiles of the temperature map from the red dashed lined in part a can be seen in Figure 7.8.d and e. The temperature profile carried out across the inclusion between the two illumination points shows a high increase in temperature under the illumination sites. As expected the temperature decreases as the photons propagate deeper in the tissue, away from its surface. Nevertheless, substantial increase in temperature is observed at the inclusion even though it positioned nearly 13 mm under both surfaces. This is due to the high optical absorption of the inclusion. Thus, this temperature map alone can identify the inclusion without any further processing. However, in order to recover the absorption of the inclusion, this temperature map is then put into the reconstruction program to obtain the absorption properties of the inclusion and chicken breast.

Figure 7.8.c shows the reconstructed high resolution absorption map demonstrating the performance of PMI in resolving the inclusion buried 13 mm deep in a biological tissue. The profiles across the inclusion show the high quantification accuracy of our technique. The size of the inclusion measured from the MR anatomic image are 2.91 mm and 4.28 mm in x- and y-

directions, respectively. PMI recovered the size of the object with 9% error, 3.2 mm and with 2% error, 4.22 mm, in the orthogonal directions. Meanwhile, the peak and mean absorption values in the FWHM are 0.045 mm-1, respectively. The error in the recovered absorption value of the inclusion is around 8.9%, very similar to the phantom study, when the peak absorption value in the reconstructed object is considered.

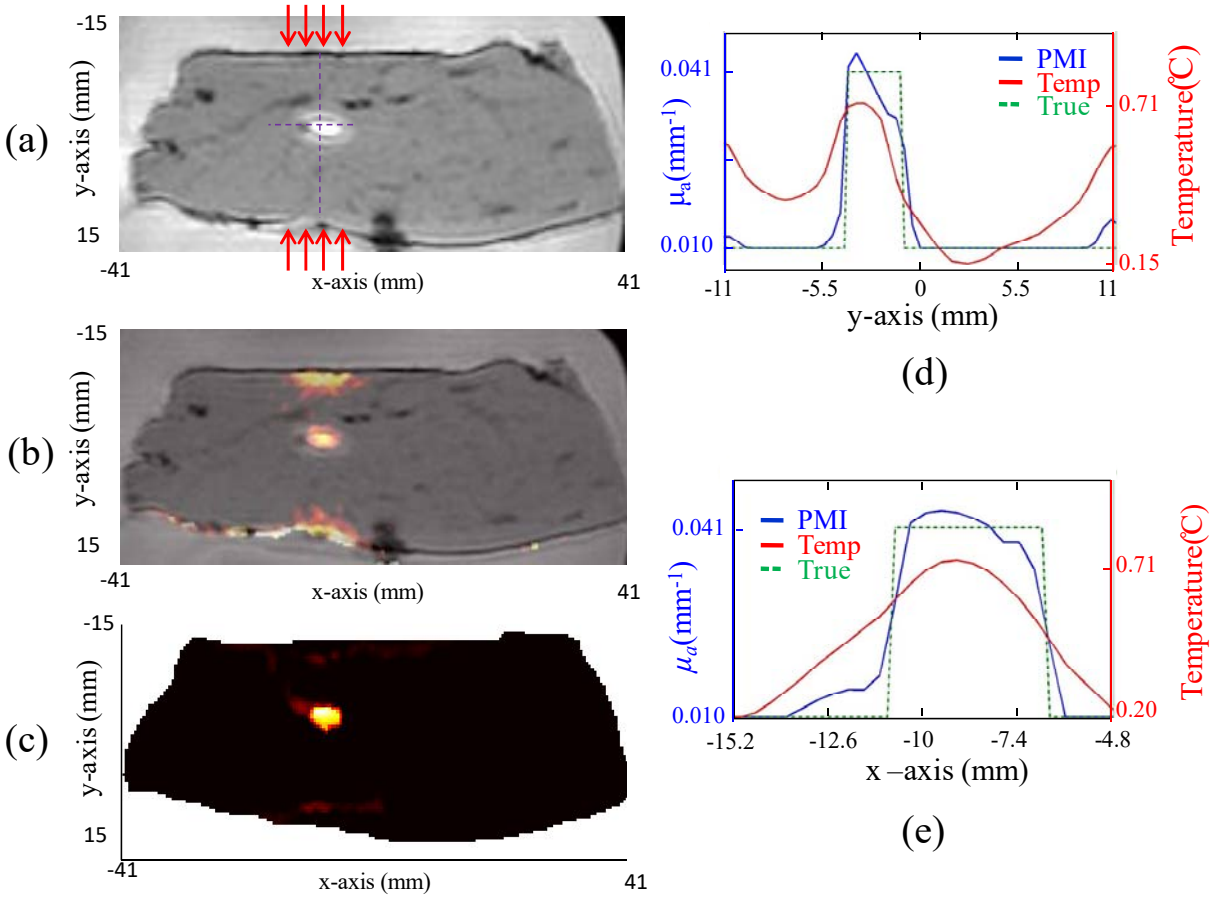

Figure 7.8 (a) shows the laser illumination position of the chicken breast phantom with a 4 times absorptions contrast inclusion at the center. The chicken breast is 3cm thick. (b) shows the temperature obtained with MRI using PMI sequence on top of the MRI acquired with gradient echo sequence. (c) shows the PMI reconstruction absorption map of this chicken breast tissue. The x and y profiles across the inclusion have been plotted in (d)&(e) comparing with the temperature profiles as in other phantom studies. The reconstructed optical value shows good agreement with the true value.

Chapter 8: Conclusion and future plans

The work presented in this thesis demonstrates the performance of our PMI technique, mainly its superior spatial resolution and high quantitative accuracy. The simulation and phantom studies show that PMI can recover objects as small as 2 mm located at different depths. It would be impossible to resolve these closely seated small objects in a turbid medium with any of the diffused optical imaging techniques, since utilizing only surface measurements provide images with poor spatial resolution due to the highly scattering nature of the tissue. On the other hand, the recently emerged new photo acoustic imaging technique provides higher spatial resolution but its major disadvantage is the requirement of sensor-tissue contact due to utilization of ultrasound. Since PMI acquires internal measurements from the whole volume, it provides unprecedented spatial resolution compared to conventional optical imaging modalities, which is independent of depth as long as the variation of temperature is above the sensitivity of the MRI. In addition to that using only continuous wave lasers, it can be a low-cost add on to any MRI system and perform as a non-contact imaging technique.

The experimental phantom studies shows that the MRT signal is directly proportional to the temperature change and is linear. The *ex vivo* PMI results presented in this thesis is the first step in translating this novel technology to the preclinical and clinical arena. The thickness of the chicken breast tissue used in the experiments is 2.6 cm so these preliminary results show that PMI can probe several centimeters deep in tissue. In addition to that, tissue sample is more heterogeneous than the agarose phantoms prepared in the lab. Unlike these phantoms, we have no control on setting the optical properties of the chicken breast tissue sample, which are unknown. Hence *ex vivo* experiments allows us to test several important steps that will be critical

for *in vivo* imaging such as estimating bulk tissue optical properties from the measurements as the first step.

Preliminary *in vivo* studies are also performed proving that PMI has a great potential for *in vivo* imaging. Hence, in the last phase of this work a PMI interface for breast imaging has been built and tested. Meanwhile, the efforts spent on the reconstruction algorithm accelerated its performance and shortened the image reconstruction time. These developments are also beneficial for the clinical translation of the PMI since real-time image reconstruction would help technicians and physicians.

At the end, simulation and experimental studies using phantom, *ex vivo* tissue samples and *in vivo* small animals demonstrated that PMI not only provides high resolution but also high quantitative accuracy in recovered tissue absorption coefficient. Actually, inclusions are localized in the raw MR temperature maps before any reconstruction process. However, a dedicated reconstruction algorithm is required to recover the quantitatively accurate high resolution absorption images.

Using multiple wavelengths, in the future PMI can provide the same functional information provided by conventional optical imaging techniques namely water, fat, oxy- and deoxy- hemoglobin maps as well as distribution of exogenous contrast agents. These quantitatively accurate high resolution tissue chromophore and contrast agent concentration maps will be useful for many applications such as cancer imaging and characterization. Hence our near future goal is to upgrade both pre-clinical and clinical PMI systems by including multiple additional lasers providing different wavelengths. In parallel, the PMI reconstruction algorithm will be extended for multi-wavelength data and direct reconstruction of tissue chromophores as well as contrast agent distribution. Our long-term goal will be translating PMI

to clinical settings for first breast cancer but later oral cancer, head & neck cancer, and lymph node imaging.

Reference

[1] E.M.C. Hillman, Experimental and theoretical investigations of near infrared tomographic imaging methods and clinical applications, University of London, 2002.

[2] A.P. Gibson, J.C. Hebden, S.R. Arridge, Recent advances in diffuse optical imaging, Phys Med Biol 50(4) (2005) R1-43.

[3] S.R. Arridge, Optical tomography in medical imaging, Inv. Prob. 15 (1999) R41.

[4] H. Dehghani, D.T. Delpy, S.R. Arridge, Photon migration in non-scattering tissue and the effects on image reconstruction, Phys Med Biol 44(12) (1999) 2897-906.

[5] H. Erkol, F. Nouizi, A. Luk, M.B. Unlu, G. Gulsen, Comprehensive analytical model for CW laser induced heat in turbid media, Opt Express 23(24) (2015) 31069-84.

[6] Horecker, The absorption spectra of hemoglobin and its derivatives in the visible and near infra-red regions, *J. Biol. Chem* (1*48* : 1*73*) (1943).

[7] U.I. Beckman Laser Institute & Medical Clinic, http://dosi.bli.uci.edu/research/

[8] V.V. Tuchin, Laser light scattering in biomedical diagnostics and therapy, J Laser Appl 5(2-3) (1993) 43-60.

[9] Y. Lin, B. W., I. J., R. W., O. Nalcioglu, G. Gulsen, Quantitative fluorescence tomography using a combined tri-modality FT/DOT/XCT system, Optics Express under review (2009).

[10] F.P. Bolin, L.E. Preuss, R.C. Taylor, R.J. Ference, Refractive index of some mammalian tissues using a fiber optic cladding method, Appl Opt 28(12) (1989) 2297-303.

[11] S.L. Jacques, Optical properties of biological tissues: a review, Phys Med Biol 58(11) (2013) R37-61.

[12] S.T. Flock, M.S. Patterson, B.C. Wilson, D.R. Wyman, Monte Carlo modeling of light propagation in highly scattering tissue--I: Model predictions and comparison with diffusion theory, IEEE Trans Biomed Eng 36(12) (1989) 1162-8.

[13] C. Darne, Y. Lu, E.M. Sevick-Muraca, Small animal fluorescence and bioluminescence tomography: a review of approaches, algorithms and technology update, Physics in medicine and biology 59(1) (2014) R1.

[14] A. Kienle, T. Glanzmann, *In vivo* determination of the optical properties of muscle with time-resolved reflectance using a layered model, Phys Med Biol 44(11) (1999) 2689-702.

[15] S.R. Arridge, M. Cope, D.T. Delpy, The theoretical basis for the determination of optical pathlengths in tissue: temporal and frequency analysis, Phys Med Biol 37(7) (1992) 1531-60.

[16] B.J. Tromberg, Optical scanning and breast cancer, Acad Radiol 12(8) (2005) 923-4.

[17] B.J. Tromberg, B.W. Pogue, K.D. Paulsen, A.G. Yodh, D.A. Boas, A.E. Cerussi, Assessing the future of diffuse optical imaging technologies for breast cancer management, Med Phys 35(6) (2008) 2443-51.

[18] H. Erkol, M.B. Unlu, Virtual source method for diffuse optical imaging, Appl Opt 52(20) (2013) 4933-40.

[19] S. Arridge, M. Schweiger, M. Hiraoka, D. Delpy, A finite element approach for modeling photon transport in tissue, Medical physics 20(2) (1993) 299-309.

[20] Y. Lin, H. Gao, D. Thayer, A.L. Luk, G. Gulsen, Photo-magnetic imaging: resolving optical contrast at MRI resolution, Phys Med Biol 58(11) (2013) 3551-62.

[21] E.J. Woo, J.K. Seo, Magnetic resonance electrical impedance tomography (MREIT) for high-resolution conductivity imaging, Physiol Meas 29(10) (2008) R1-26.

[22] D.O.K.J.P.K.V.S.M.T.T.V.M. Arridge S R, A. Zacharopoulos, Reconstruction of subdomain boundaries of piecewise constant coefficients of the radiative transport equation from optical tomography data, Inverse Problems 22(6) (2006) 2175.

[23] S.R. Arridge, M. Hiraoka, M. Schweiger, Statistical basis for the determination of optical pathlength in tissue, Phys Med Biol 40(9) (1995) 1539-58.

[24] S.R. Arridge, J.C. Hebden, Optical imaging in medicine: II. Modelling and reconstruction, Phys Med Biol 42(5) (1997) 841-53.

[25] F. Nouizi, fluorescence and diffuse optical tomography: non-contact instrumentation, modeling and time-resolved 3D reconstruction, France, 2011.

[26] Tuchin, Tissue optics: light scattering methods and instruments for medical diagnosis, 2007.

[27] I. A., Wave propagation and scattering in Random media, Academic Press, New York, NY (1978).

[28] W.G., T.W.H. Egan, O*ptical Properties of Inhomogeneous Materials*, New York, 1979.

[29] R., J.T.B. Groenhuis, H.A. Ferwerda, Scattering and absorption of turbid materials determined from reflection measurements. 2:Measuring method and calibration, Applied Optics 22(16) (1983).

[30] F. Gao, P. Poulet, Y. Yamada, Simultaneous mapping of absorption and scattering coefficients from a three-dimensional model of time-resolved optical tomography, Appl Opt 39(31) (2000) 5898-910.

[31] F. Nouizi, M. Torregrossa, R. Chabrier, P. Poulet, Improvement of absorption and scattering discrimination by selection of sensitive points on temporal profile in diffuse optical tomography, Opt Express 19(13) (2011) 12843-54.

[32] J. Chen, V. Venugopal, F. Lesage, X. Intes, Time-resolved diffuse optical tomography with patterned-light illumination and detection, Opt Lett 35(13) (2010) 2121-3.

[33] A. Puszka, L. Hervé, A. Planat-Chrétien, A. Koenig, J. Derouard, J.M. Dinten, Time-domain reflectance diffuse optical tomography with Mellin-Laplace transform for experimental detection and depth localization of a single absorbing inclusion, Biomed Opt Express 4(4) (2013) 569-83.

[34] R.J. Cooper, E. Magee, N. Everdell, S. Magazov, M. Varela, D. Airantzis, A.P. Gibson, J.C. Hebden, MONSTIR II: a 32-channel, multispectral, time-resolved optical tomography system for neonatal brain imaging, Rev Sci Instrum 85(5) (2014) 053105.

[35] A. Planat-Chrétien, Design of an optimized time-resolved diffuse optical tomography probe to achieve deep absorption contrast reconstruction in a cylindrical geometry SPIE Optical Tomography and Spectroscopy of Tissue, 2013.

[36] R.W. Holt, K.M. Tichauer, H. Dehghani, B.W. Pogue, F. Leblond, Multiple-gate time domain diffuse fluorescence tomography allows more sparse tissue sampling without compromising image quality, Opt Lett 37(13) (2012) 2559-61.

[37] F. Nouizi, 3D modeling of noncontact fiber-based approach for time-resolved diffuse optical tomography SPIE Optical Tomography and Spectroscopy of Tissue, 2011.

[38] B.O. Unlu B.M, Shafihaa R., Gulsen G., Nalcioglu O., Diffuse Optical Tomographic Reconstruction Using Multi-frequency Data, J Biomed Opt 11(5) (2006) 054008.

[39] D.T. Y Lin, O Nalcioglu and G Gulsen,, Tumor Characterization in Small Animals Using MR-guided Dynamic Contrast Enhanced Diffuse Optical Tomography (DCE-DOT), Journal of Biomedical Optics In press (2011).

[40] H.Y. Ban, M. Schweiger, V.C. Kavuri, J.M. Cochran, L. Xie, D.R. Busch, J. Katrašnik, S. Pathak, S.H. Chung, K. Lee, R. Choe, B.J. Czerniecki, S.R. Arridge, A.G. Yodh, Heterodyne frequency-domain multispectral diffuse optical tomography of breast cancer in the parallel-plane transmission geometry, Med Phys 43(7) (2016) 4383.

[41] A.M. Laughney, V. Krishnaswamy, T.B. Rice, D.J. Cuccia, R.J. Barth, B.J. Tromberg, K.D. Paulsen, B.W. Pogue, W.A. Wells, System analysis of spatial frequency domain imaging for quantitative mapping of surgically resected breast tissues, J Biomed Opt 18(3) (2013) 036012.

[42] H.K. Kim, A.H. Hielscher, A PDE-constrained SQP algorithm for optical tomography based on the frequency-domain equation of radiative transfer, Inverse Problems 25(1) (2009) 015010.

[43] S.R. Arridge, Methods in diffuse optical imaging, Philos Transact A Math Phys Eng Sci 369(1955) (2011) 4558-76.

[44] R.A. Simon, C.S. John, Optical tomography: forward and inverse problems, Inverse Problems 25(12) (2009) 123010.

[45] V.M. Tarvainen T, S.R. Arridge, Image reconstruction in optical tomography using the finite element solution of the frequency domain radiative transfer equation, J. Qaunt. Spect. Rad. Transfer 109(17-18) (2008) 2767.

[46] S. Arridge, Photon-measurement density functions. Part I: Analytical forms, Appl. Opt. 34 (1999) 7395-7409.

[47] M. Schweiger, S.R. Arridge, M. Hiraoka, D.T. Delpy, The finite element method for the propagation of light in scattering media: boundary and source conditions, Med Phys 22(11 Pt 1) (1995) 1779-92.

[48] D.W. Marquardt, J. Soc. Industr. Appl. Math. 11(2) (1963) 431.

[49] K., Levenberg, A method for the solution of certain non–linear problems in least squares, 1944.

[50] A.S., R., Forward and inverse problems in time resolved infrared imaging, Med. Opt (1993).

[51] H., D.B. Dehghani, I. Basarab-Horwath, Incorporating a priori anatomical information into image reconstruction in electrical impedance tomography, Physiological measurement 20(1) (1999).

[52] Tikhonov, Regularization of mathematically incorrectly posed problems, 1963.

[53] K.D. Paulsen, H. Jiang, Spatially varying optical property reconstruction using a finite element diffusion equation approximation, Med Phys 22(6) (1995) 691-701.

[54] S. Srinivasan, B.W. Pogue, H. Dehghani, S. Jiang, X. Song, K.D. Paulsen, Improved quantification of small objects in near-infrared diffuse optical tomography, J Biomed Opt 9(6) (2004) 1161-71.

[55] P.K. Yalavarthy, B.W. Pogue, H. Dehghani, K.D. Paulsen, Weight-matrix structured regularization provides optimal generalized least-squares estimate in diffuse optical tomography, Med Phys 34(6) (2007) 2085-98.

[56] P.K. Yalavarthy, B.W. Pogue, H. Dehghani, C.M. Carpenter, S. Jiang, K.D. Paulsen, Structural information within regularization matrices improves near infrared diffuse optical tomography, Opt. Express 15(13) (2007) 8043-8058.

[57] F. Nouizi, A. Luk, D. Thayer, Y. Lin, S. Ha, G. Gulsen, Experimental validation of a high-resolution diffuse optical imaging modality: photomagnetic imaging, J Biomed Opt 21(1) (2016) 16009.

[58] A.T., D.T. Luk, Y. Lin, F. Nouizi, H. Gao, G. Gulsen, A novel high-resolution optical imaging modality: photo-magnetic imaging, SPIE BiOS International Society for Optics and Photonics, San Francisco, 2013.

[59] D.A. Thayer, Y. Lin, A. Luk, G. Gulsen, Laser-induced photo-thermal magnetic imaging, Appl Phys Lett 101(8) (2012) 83703.

[60] J.C. Hebden, S.R. Arridge, D.T. Delpy, Optical imaging in medicine: I. Experimental techniques, Phys Med Biol 42(5) (1997) 825-40.

[61] H. Erkol, F. Nouizi, M.B. Unlu, G. Gulsen, An extended analytical approach for diffuse optical imaging, Phys Med Biol 60(13) (2015) 5103-21.

[62] Kwong, Simulation of optical breast density measurements using structured light illumination; SPIE, 2014.

[63] Schweiger, Application of the finite-element method for the forward and inverse models in optical tomography, Math Imaging 3: 263. (1993).

[64] E.H., Wissler, Pennes' 1948 paper revisited, J Appl Physiol 85(1) (1985).

[65] F. Nouizi, H. Erkol, A. Luk, M. Marks, M.B. Unlu, G. Gulsen, An accelerated photo-magnetic imaging reconstruction algorithm based on an analytical forward solution and a fast Jacobian assembly method, Phys Med Biol 61(20) (2016) 7448-7465.

[66] Diaz, Modeling the thermal response of porcine cartilage to laser irradiation; 2001.

[67] C.J.P.S.J.J. Boas D A, A.K. Dunn, Three dimensional Monte Carlo code for photon migration through complex heterogenous media including the adult human head, Opt. Express 10 (2002) 159.

[68] K.M.J.S.L.W.A.J. Prahl S A, A Monte Carlo model of light propagation in tissue, Dosimetry of Laser Radiation in Medicine and Biology 5 (1989) 102.

[69] Patterson, Diffusion equation representation of photon migration in tissue, 1991.

[70] J.M. Schmitt, G.X. Zhou, E.C. Walker, R.T. Wall, Multilayer model of photon diffusion in skin, J Opt Soc Am A 7(11) (1990) 2141-53.

[71] D.A. Boas, M.A. O'Leary, B. Chance, A.G. Yodh, Scattering of diffuse photon density waves by spherical inhomogeneities within turbid media: analytic solution and applications, Proc Natl Acad Sci U S A 91(11) (1994) 4887-91.

[72] S.A. Walker, D.A. Boas, E. Gratton, Photon density waves scattered from cylindrical inhomogeneities: theory and experiments, Appl Opt 37(10) (1998) 1935-44.

[73] B.W. Pogue, M.S. Patterson, Frequency-domain optical absorption spectroscopy of finite tissue volumes using diffusion theory, Phys Med Biol 39(7) (1994) 1157-80.

[74] D. Contini, F. Martelli, G. Zaccanti, Photon migration through a turbid slab described by a model based on diffusion approximation. I. Theory, Appl Opt 36(19) (1997) 4587-99.

[75] F. Martelli, A. Sassaroli, Y. Yamada, G. Zaccanti, Analytical approximate solutions of the time-domain diffusion equation in layered slabs, J Opt Soc Am A Opt Image Sci Vis 19(1) (2002) 71-80.

[76] A. Kienle, Light diffusion through a turbid parallelepiped, J Opt Soc Am A Opt Image Sci Vis 22(9) (2005) 1883-8.

[77] A. Liemert, A. Kienle, Light diffusion in a turbid cylinder. I. Homogeneous case, Opt Express 18(9) (2010) 9456-73.

[78] A., D.P. Zhang, C.F. Bunting, B.W. Pogue, Photon diffusion in a homogeneous medium bounded externally or internally by an infinitely long circular cylindrical applicator. I. Steady-state theory, JOSA A 27(3) (2010).

[79] J. Sikora, A. Zacharopoulos, A. Douiri, M. Schweiger, L. Horesh, S.R. Arridge, J. Ripoll, Diffuse photon propagation in multilayered geometries, Phys Med Biol 51(3) (2006) 497-516.

[80] A. Liemert, A. Kienle, Light diffusion in N-layered turbid media: frequency and time domains, J Biomed Opt 15(2) (2010) 025002.

[81] G., M.S. Brix, G. Hellwig, J. Griebel, Estimation of heat transfer and temperature rise in partial-body regions during MR procedures: an analytical approach with respect to safety considerations, Magnetic resonance imaging 20(1) (2002).

[82] Z.S. Deng, J. Liu, Mathematical modeling of temperature mapping over skin surface and its implementation in thermal disease diagnostics, Comput Biol Med 34(6) (2004) 495-521.

[83] Nouizi, Real-time photo-magnetic imaging, Bio. Opt. express 7(10) (2016).

[84] Y. Lin, D. Thayer, O. Nalcioglu, G. Gulsen, Tumor characterization in small animals using magnetic resonance-guided dynamic contrast enhanced diffuse optical tomography, J Biomed Opt 16(10) (2011) 106015.

[85] N.S. Abadeer, Recent progress in cancer thermal therapy using gold nanoparticles, in: C.J. Murphy (Ed.) 2016.

[86] W. Cai, T. Gao, H. Hong, J. Sun, Applications of gold nanoparticles in cancer nanotechnology, Nanotechnol Sci Appl 1 (2008) 17-32.

[87] D.M. Ikeda, D.R. Baker, B.L. Daniel, Magnetic resonance imaging of breast cancer: clinical indications and breast MRI reporting system, J Magn Reson Imaging 12(6) (2000) 975-83.

[88] M.Y. Su, H.J. Yu, P.M. Carpenter, C.E. McLaren, O. Nalcioglu, Pharmacokinetic parameters analyzed from mr contrast enhancement kinetics of multiple malignant and benign breast lesions detected in the same patients, Technol Cancer Res Treat 4(3) (2005) 255-63.

[89] M.Y. Su, Y.C. Cheung, J.P. Fruehauf, H. Yu, O. Nalcioglu, E. Mechetner, A. Kyshtoobayeva, S.C. Chen, S. Hsueh, C.E. McLaren, Y.L. Wan, Correlation of dynamic contrast enhancement MRI parameters with microvessel density and VEGF for assessment of angiogenesis in breast cancer, J Magn Reson Imaging 18(4) (2003) 467-77.

[90] K. Blyschak, M. Simick, R. Jong, L. Lilge, Classification of breast tissue density by optical transillumination spectroscopy: optical and physiological effects governing predictive value, Med Phys 31(6) (2004) 1398-414.

[91] S. Srinivasan, B.W. Pogue, S. Jiang, H. Dehghani, C. Kogel, S. Soho, J.J. Gibson, T.D. Tosteson, S.P. Poplack, K.D. Paulsen, Interpreting hemoglobin and water concentration, oxygen saturation, and scattering measured *in vivo* by near-infrared breast tomography, Proc Natl Acad Sci U S A 100(21) (2003) 12349-54.

[92] A.M. Chen, F. Meric-Bernstam, K.K. Hunt, H.D. Thames, M.J. Oswald, E.D. Outlaw, E.A. Strom, M.D. McNeese, H.M. Kuerer, M.I. Ross, S.E. Singletary, F.C. Ames, B.W. Feig, A.A. Sahin, G.H. Perkins, N.R. Schechter, G.N. Hortobagyi, T.A. Buchholz, Breast conservation after neoadjuvant chemotherapy: the MD Anderson cancer center experience, J Clin Oncol 22(12) (2004) 2303-12.

[93] J.H. Chen, B. Feig, G. Agrawal, H. Yu, P.M. Carpenter, R.S. Mehta, O. Nalcioglu, M.Y. Su, MRI evaluation of pathologically complete response and residual tumors in breast cancer after neoadjuvant chemotherapy, Cancer 112(1) (2008) 17-26.

[94] A. Luk, ex-vivo Validation of Photo-Magnetic Imaging, submitted.

[95] A. Luk, Monitoring gold nanoparticle distribution with high resolution using photo-magnetic imaging, SPIE, San Francisco, 2016.

[96] E.E. Graves, J. Ripoll, R. Weissleder, V. Ntziachristos, A submillimeter resolution fluorescence molecular imaging system for small animal imaging, Med Phys 30(5) (2003) 901-11.

[97] G. Marquez, Anisotropy in the absorption and scattering spectra of chicken breast tissue, Appl. Opt 37(4) (1998).

[98] Tromberg B J et al, Non-invasive *in vivo* characterization of breast tumors using photon migration spectroscopy Neoplasia 2 26-40 (2000)

[99] Mehmet Burcin Unlu, Yuting Lin and Gultekin Gulsen. Dynamic contrast-enhanced diffuse optical tomography (DCE-DOT): experimental validation with a dynamic phantom , Physics in medicine and biology